The Dissertation Committee for Junse Lee
certifies that this is the approved version of the following dissertation:

Modeling and Analyzing Wireless Networks using Stochastic Geometry

Committee:

François Baccelli, Supervisor

Gustavo de Veciana

Jeffrey G. Andrews

Robert W. Heath Jr.

Thibaud Taillefumier

Modeling and Analyzing Wireless Networks using Stochastic Geometry

by

Junse Lee

DISSERTATION

Presented to the Faculty of the Graduate School of

The University of Texas at Austin

in Partial Fulfillment

of the Requirements

for the Degree of

DOCTOR OF PHILOSOPHY

THE UNIVERSITY OF TEXAS AT AUSTIN

May 2018

Dedicated to my family.

Acknowledgments

The four years of the Ph.D. program at UT Austin was an incredible journey in my life, and I would like to express my gratitude to many people for their helps and supports during this time.

First, I would like to extend my sincere gratitude to my supervisor Prof. François Baccelli. Over the past four years, I have learned his solid engineering knowledge, great senses for research directions, his deep mathematical knowledge, high standards for rigorous works, strong work ethic and dedications to research. His guidance and helps have really shaped me into an independent researcher and professional engineer. I also want to thank my dissertation committee members Prof. Gustavo de Veciana, Prof. Robert Heath, Prof. Jeff Andrews, and Prof. Thibaud Taillefumier for providing useful comments to my research and dissertation. Furthermore, I want to thank Prof. de Veciana. In his course, I have learned a lot about fundamentals of queuing theory. I also want to thank Prof. Heath for the wireless communications lab course, which is very useful for my research and job interviews.

My life at UT has been really wonderful and memorable, thanks to my brilliant colleagues and friends. I thank Jongwon Lee, Xinchen Zhang, Namyoon Lee, Jaeoh Woo and Yingzhe Li for their academic guidance during my early Ph.D. years, and Junil Choi, Gilwon Lee, Jeonghun Park, Abishek

Sankararaman, and Ahmad Alammouri for various valuable technical discussions. I would also like to thank my friends for spending a lot of memorable moments with me: Daewon Seo, Hyoyoung Jeong, Heechai Kang, Junho Choi, Yeonhak Jung, Sungwoo Park, Muryong Kim, Taewan Kim, Jinseok Choi, Jaeseong Lee, Saungeun Park, Kiyeon Jeon, Junmo Sung, Dohyun Kim, Mandar Kulkarni, Pranav Madadi and many others. I also want to express my appreciation to Melanie Gulick and Karen Little for their helps.

Finally, I woud like to thank my wife, Jungmin Park, for sharing this unbelievable Ph.D. journey with me; my lovely son, Jongyoon Lee.

Modeling and Analyzing Wireless Networks using Stochastic Geometry

Publication No. _____

Junse Lee, Ph.D.
The University of Texas at Austin, 2018

Supervisor: François Baccelli

Over the past decade, stochastic geometric models, and most notably the planar Poisson point process (PPP) model, have become popular for the analysis of spectral efficiency in wireless networks, in both the D2D and the cellular contexts [1]. By modeling base station (BS) and user locations as spatial point processes, stochastic geometry has recently been recognized as a tractable and efficient analytical tool to quantify key performance metrics. This tool provides a natural way of defining and computing macroscopic properties of multiuser information theory. These properties are obtained by averaging over all node patterns found in a large random network of the Euclidean plane. For example, some key performance metrics such as signal to interference and noise ratio and data rate depend on the network geometric configurations. This tool has thus been widely adopted for analyzing the network performance and broadening network design.

This thesis proposes new models to represent several new scenarios. Three main scenarios are considered: 3-D inbuilding networks, MIMO ad-hoc networks, and multihop communication under mmWave networks. To do so, mathematical tools such as Poisson point processes, Poisson line processes, Boolean models and Poisson bipolar models are used. Each model is 1) *generative* in that it has a clear physical interpretation, 2) leads to explicit analytical representations of important wireless performance metrics, and 3) highly *parametric*, with parameters expressing the geometric characteristic of the elements of networks. Physical interpretations from these models are quite different from previous results.

The core of this thesis is focused on the effects of correlated shadowing. Shadowing is the effect that the received signal power fluctuates due to objects obstructing the propagation path. By introducing an independent shadowing term over links, it is possible to model the effect of shadow fading. Most previous papers analyzing urban networks assume that shadowing fields are independent over links. With this assumption, it is possible to derive simple closed-form expressions of important network performance metrics. However, this assumption cannot capture that shadowing fields are spatially correlated. This thesis goes beyond the independent shadowing approximation and analyzes the effects of correlated shadowing on various performance metrics.

Table of Contents

List of Tables

List of Figures

Chapter 1

Introduction

In order to evaluate the performance of wireless networks, system level simulation is crucial. By implementing a vast set of network topologies, wireless channel models, network protocols and traffic models, system level simulation can accurately evaluate key performance metrics. However, a major limitation of simulations is that each wireless scenario should be simulated separately when different system parameters are used. As networks become complicated, system level simulation consumes much time and becomes expensive.

Thus, it is necessary to capture essential characteristics of wireless networks with high accuracy and low complexity. As an alternative to system level simulation, stochastic geometry is now recognized as a tractable analytical tool for deriving key performance metrics of networks by utilizing spatial point process to model the location of users and base stations. In this approach, the locations of the network elements are seen as the realizations of some point processes. Stochastic geometry, in particular point process theory, can provide an analytically approach for characterizing important key metrics of wireless networks and for performing optimizations more efficiently

than simulation. Over the last few decades, several studies in this field have contributed to a better understanding of network behaviors.

The main goal of this thesis is to provide new insights on some physical phenomena (e.g. correlated shadowing) and wireless network scenarios (e.g. 3-D in-building networks) which have not been discussed sufficiently in the stochastic geometric framework.

This introductory chapter consists of four parts. Section 1.1 discusses some effects of the shadowing in modern wireless networks whereas 1.2 discusses MIMO ad-hoc networks, respectively. Section 1.3 summarizes the key contributions of this dissertation. Finally, Section 1.4 presents how the rest of this dissertation is organized.

1.1 Analysis of Blockage Effects

The main focus below is on the penetration loss of radio signals due to obstruction by obstacles. Such blockage effects make it hard to predict network performances and become more severe in higher frequencies such as millimeter-wave (mmWave) networks. Therefore, the modeling and analysis of blockage are crucial in modern wireless networks.

Typically, blockage effects are incorporated into the shadowing field, and shadowing of each link is often modeled by using a log-normal random variable with some measured variance. However, this approach cannot capture the effect of network topologies. To understand the effect of network topolo-

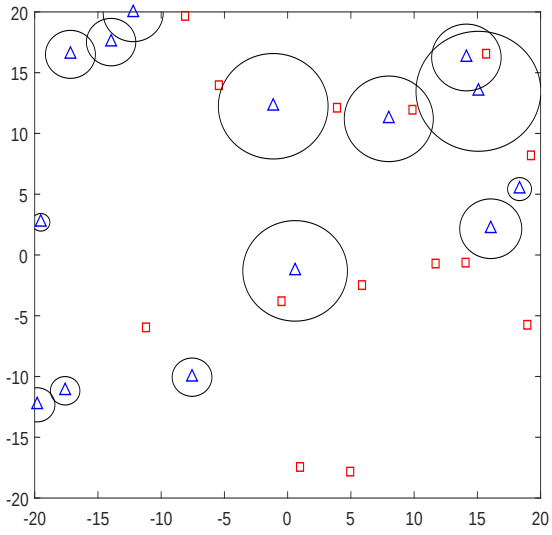

Figure 1.1: An example of Boolean model. Triangles are centers of blockages and squares are base stations.

gies, many previous papers took a stochastic geometry approach as in [2–4].

Especially, [4] proposed a new mathematical framework to model random blockages and analyzed the impact on network performance. In this paper, the authors modelled the obstacles by a Boolean model [5]. More precisely, obstacles have a random shapes and centers which form a homogenous Poisson point process as in Figure 1.1. In this figure, the shape of obstacles is a disc with a random radius and centers of disc (triangles) and users (squares) form independent homogeneous Poisson point processes (PPP). By leveraging the random shape theory, the authors obtained that the distribution of the number of obstacles obstructing a link is a Poisson random variable with

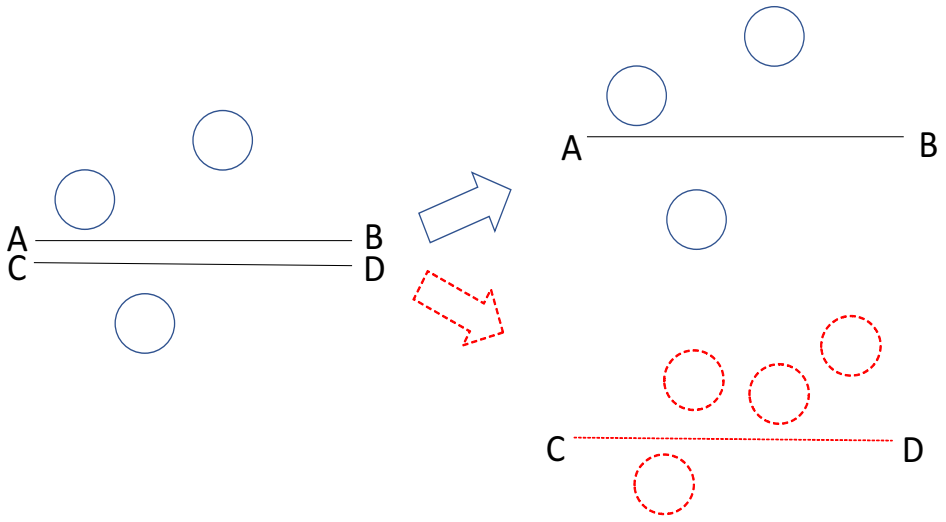

Figure 1.2: Comparison of the correlated shadowing model and the independent shadowing model. A boolean model is generated per each link under the independent model, while is generated per each user process under the correlated model.

mean which depends on its length of the link. By incorporating this result into a path loss model, the authors analyzed the performance of cellular networks such as coverage probability, and the average rate. This approach provides significant intuitions to interpret network behaviors and the impact of shadowing effects. Also, important metrics are obtained by simple closed form expressions.

Shadowing is spatially correlated. For example, let us consider two nearby links with the same length as in Figure 1.2. If the probability that one of these two line segments, AB, is not blocked by any obstacles is p, the probability that both two links, AB and CD, are not blocked is almost p under

the correlated shadowing model (or in real environment), while that probability is p^2 in the independent shadowing model. So, the previous stochastic models cannot capture this spatial shadowing correlation since they assign independent shadowing coefficients over links. Motivated by this, the first three contributions of this dissertation investigate the effect of correlated shadowing by proposing new models.

In Chapters 2, 3, and 4, I propose new mathematical models which aim capturing the shadowing correlations. In Chapter 2, I propose a new model for 3-D in-building network, called the *Poisson building*. By leveraging Poisson line processes, walls (obstacles) parallel to xy, yz, and zx planes are randomly constructed. This model leads to explicit analytical representations of the interference field and of its correlation induced by common obstacles. This chapter shows that the distributions of interference of the correlated and the independent shadowing are quite different. Chapter 3 focuses on the effect of shadowing correlation on wireless network performance. I propose a concept of *Shadowing cell* where base stations in the same *Shadowing cell* have the same shadowing random variable. Interestingly, previous independent shadowing approximation leads to pessimistic evaluation for a wide variety of metrics such as coverage probability and Shannon throughput. Chapter 4 analyzes connectivity of multihop communications in mmWave bands. This chapter provides some connectivity results in the correlated and independent blockage models.

1.2 MIMO Communications in Ad-Hoc Networks

The capacity of MIMO mobile ad-hoc networks (MANET) has been thoroughly analyzed. MANETs are self-organizing wireless networks in which mobile devices do not need any infrastructure such as base stations and MIMO is a method for multiplying the capacity of a wireless link. It has been studied where a finite number of transmitter and receiver pairs communicate in a deterministic network topology. To increase the capacity, optimal power allocation strategies were proposed in [6–8]. However, the common assumption in these studies is that the distances between any two nodes in the network are deterministic or identical. Thus, this approach cannot be used in large random MANETs to evaluate the gain of MIMO transmission.

To model such large random MANETS, a Poisson network has been considered, in which the locations of interferers form a realization of a homogenous PPP. Under this network model, the transmission capacity [9], which quantifies the maximum allowable spatial density of successful transmissions per unit area given an outage constraint, was characterized. With the transmission capacity, [10] showed that interference cancellation techniques at a receiver employing multiple antennas can provide a linear increase of the transmission capacity with respect to the network density. In [11], it was shown that a single stream transmission is optimal under the MIMO setting.

Transmission capacity is a natural and intuitive metrics for analyzing wireless networks under such a Poisson configuration. However, it cannot capture the effects of rate adaptation techniques. Motivated by this, Chapter

5 defines *Ergodic spectral efficiency* under Poisson configuration with MIMO transmission techniques and analyze network behaviors. Especially, *Ergodic spectral efficiency* quantifies the achievable Shannon transmission rate while transmission capacity computes a maximum successful transmission density under a reliability constraint. Chapter 5 will show that a new insight such as gains from spatial multiplexing transmission can be obtained with this new performance metric.

1.3 Contributions

This dissertation mainly aims at utilizing stochastic geometry to model and analyze wireless networks. The main technical contributions of this dissertation are covered from Chapter 2 to 5, and can be summarized as follows.

Modeling a New 3-D In-building Wireless Networks with Correlated Shadowing

This topic is addressed in Chapter 2. In this work, I present a new stochastic geometric model, namely *Poisson building*, for representing 3-D in-building wireless networks.

The main technical challenge for obtaining a tractable 3-D spatial model for in-building wireless networks lies in the proper handling of the shadowing correlation created by the static physical objects compared to the classical planar models such as [12]. As most of the planar models are designed to study outdoor networks, the shadowing correlation is typically ignored and

path loss is simply modeled through independent log-normal shadowing coefficients [2,3] or distance-dependent function combined with independent shadowing random variables [4, 13].

The *Poisson building* model explicitly handles the shadowing correlation. This model is compatible with the empirical lognormal shadowing model in that the marginal shadowing component converges to lognormal distribution as the link distance grows. Under this model, I demonstrate the tractability by deriving the interference distribution and its spatial correlation. This leads to analytical characterizations of the SINR distributions of D2D underlay networks and the coverage probability of in-building networks. I also consider a couple of important variants, namely the finite Poisson building and the semi-infinite Poisson building. The latter allows one to analyze the interference in a window office, which is a boundary office in a large semi-infinite building. The analysis of these variants further reveals fundamental differences between 3-D and 2-D correlated shadowing analysis.

On the Effect of Shadowing Correlation on Wireless Network Performance

As I said above, many previous studies use independent shadowing approximation to analyze shadowing effects in model wireless networks since it is possible to obtain simple exact expressions of network performances with this approximation. Motivated by this, in Chapter 3, I investigate the effect of shadowing correlation on important wireless network performances to complement the independent shadowing approximation.

To do so, I propose a new shadowing field model to capture spatial correlations. In order to represent the spatial correlation property, I provide two intuitive network examples where shadowing variables are assigned based on the network topology. With these network examples, I compute and compare the interference distributions under the correlated and independent shadowing models in the stochastic ordering sense. To provide a fair comparison, the same marginal shadowing laws are used in both cases. I first compute the Laplace transforms of the interference observed by the typical user under both the correlated and the independent shadowing models. Then, I provide stochastic ordering relation of three widely used metrics (coverage probability, Shannon throughput, and local delay) which will be shown completely monotone functions of interference between two shadowing models by using well known results on the relation between the Laplace transform ordering and completely monotone functions.

From these ordering relations, I conclude that when ignoring the spatial correlations of shadowing, widely used metrics such as coverage probability, Shannon throughput, local delay are systematically evaluated in a possibly quite pessimistic way.

Multihop Connectivity of Millimeter-Wave Networks

Chapter 4 presents some connectivity results of mmWave multihop communications. Even though multihop communication is a promising technique to improve coverage and network connectivity, it has not been sufficiently analyzed under mmWave networks.

In Chapter 4, the main analysis is focused on network connectivity, and it concerns both ad-hoc and cellular multihop networks. To model and analyze the blockage effect, a Poisson-Boolean model is used. In order to get simple analytical expressions, I first assume blockage process is independent over links, and then consider effects of blockage correlation, which is closer to real environments. I refer to these as independent blockage model and correlated blockage model, respectively. Under the independent blockage model, I obtain exact expressions for the distributions of the users connected to the typical user or to the typical base station. Especially, I provide exact expressions of the mean numbers of k-hop paths starting from (or ending to) the typical user and the distribution of users connected to the typical base station in 2 hops. Then, the condition of the user density for having a cluster of infinitely many connected users is obtained by using percolation properties of the random connection model. Finally, the correlated blockage model is also considered. It is shown that the mean numbers of users connected to the typical user, the typical base station or any base stations in one hop are the same under the independent and correlated blockage models. Unlike the independent blockage model, even though the user density is high enough, there exists no cluster of infinitely many connected users under certain blockage conditions.

Scaling Laws for Ergodic Spectral Efficiency in MIMO Ad-hoc Poisson Networks

The benefits of multiple antenna communication in random wireless networks are considered in Chapter 5. In many previous papers, MIMO ad-

hoc networks have been analyzed in stochastic geometric model. Most of them focused on *transmission capacity* as in [11] which is constrained by a reliability condition, and not many papers analyzed Shannon throughput of MIMO ad-hoc networks. Motivated by this, I analyze *ergodic spectral efficiency* of MIMO ad-hoc networks under several network scenarios.

The setting is that of the Poisson bipolar model introduced in [14], which is a natural model for ad-hoc and device-to-device (D2D) networks. With knowledge of channel state information at receiver, I derive *ergodic spectral efficiencies* with a function of the number of antennas, the node density, and the path loss exponent, when a zero forcing receiver or a zero forcing successive interference cancellation receiver are used.

The primary finding is that, with knowledge of channel state information between a receiver and its associated transmitter, by zero-forcing successive interference cancellation, and for appropriate antenna configurations, the ergodic spectral efficiency can be made to scale linearly with both 1) the minimum of the number of transmit and receive antennas, 2) the density of nodes, and 3) the pathloss exponent. This linear gain is achieved by using the transmit antennas to send multiple data streams (e.g. through an open-loop transmission method) and by exploiting the receive antennas to cancel interference. Further, when a receiver can learn channel state information from a certain number of near interferers, higher scaling gains can be achieved when using a successive interference cancellation method. A major implication of the derived scaling laws is that spatial multiplexing transmission methods are

essential for obtaining better and eventually optimal scaling laws in multiple antenna random wireless networks. This is a new insight which is not obtained with transmission capacity view. Since transmission capacity is a performance metric with a reliability constraint, transmitting one data stream is optimal for enhancing reliability.

1.4 Organization

The rest of dissertation is organized as follows. Chapter 2 introduces the *Poisson building* model, a 3-D tractable comprehensive 3-D spatial model for in-building networks. Chapter 3 analyzes the effect of correlated shadowing and provides the ordering of some important performance metrics under spatially correlated and independent assumptions. Chapter 4 presents connectivity results on multihop relaying in mmWave networks. Chapter 5 provides new insights on MIMO ad-hoc networks using *Ergodic spectral efficiency*. The dissertation is concluded in Chapter 6 by summarizing the key contributions and discussing potential research directions.

Chapter 2

A 3-D Spatial Model for In-building Wireless Networks with Correlated Shadowing

In this chapter[1], I propose *Poisson building* model which captures the complex in-building shadowing correlations.

2.1 Introduction

Analyists predict in-building wireless networking to be one of the fastest growing markets of the wireless industry. Since traffic increase is expected to come from indoor networks, mobile operators are investigating in-building network deployment in recent and upcoming years [18]. The potential of the in-building wireless market largely comes from the complement it offers to conventional outdoor network deployments, and from the exponential growth of mobile traffic demand. On the contrary, the spatial modeling of in-building wireless networks largely remains an uncharted area despite the great progress in the planar (2-D) modeling of wireless networks over the past decade. This contribution presents a first attempt toward getting a tractable comprehensive

[1]This chapter has been published in [15, 16]. I am the primary author of these works. Coauthor Dr. Xinchen Zhang has provided many discussions and insightful feedbacks to this work, and Dr. Françcois Baccelli is my supervisor.

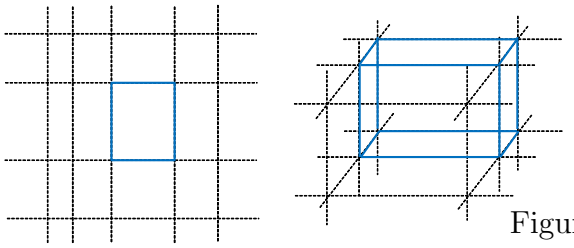

Figure 2.1: One realization of Poisson grids for 2-D and 3-D. Typical room is highlighted with a solid box.

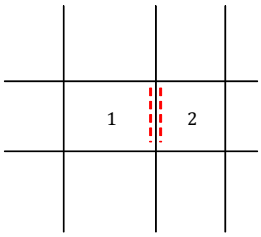

Figure 2.2: Transmitter deployments in 2-D. Room 1 and 2 share one line segment but physically 2 transmitter processes along that line are built and assigned one to room 1 and the other to room 2.

3-D spatial model in this context.

2.1.1 Related Works

2.1.1.1 3-D Network Models

The 3-D Poisson building model is not the only 3-D model for wireless networks; nor the simplest one. One obvious alternative is to generalize the usual 2-D model directly by distributing nodes as a Poisson point process in the 3-D space and applying a distance-based path loss function [17, 18]. This will be referred to as the *free-space 3-D model*. While such a model is analytically convenient, it may appear to be inadequate in some contexts. Distance-based path loss models are usually derived using free space propagation assumptions (Friis' equation) and a simplified ground reflection model (e.g., the 2-ray model or the Hata model [19, 20]). Therefore, applying this model to the 3-D in-building context amounts to ignoring the major path loss contributor, namely (spatially correlated) blockage. In contrast, the Poisson building model is built

in order to represent blockage effects and to provide a compact mathematical model for in-building networks with variable size rooms.

The free-space 3-D and the Poisson building are compared in Sect. 2.5.3, where important metrics pertaining to the distribution of interference created by the very same collection of wireless nodes are shown to lead to arbitrarily large discrepancies.

2.1.1.2 Ray-tracing

Accurate in-building network analysis can be achieved by 3-D ray-tracing [21, 22]. As a site-specific approach, 3-D ray-tracing requires sophisticated software packages and an exact building geometry. In contrast, the stochastic geometric modeling approach of this chapter is based on analyzing a random structure of obstacles with a small number of key parameters. It thus works without a complete description of the propagation environment and is more flexible in obtaining general design guidelines for 3-D in-building networks. In fact, in the long term, this approach might provide a theoretically justified and rather simple alternative to 3-D ray-tracing software platforms which are often difficult to build and use.

2.1.2 Contributions

Compared to classical planar models, the main technical challenge for obtaining a tractable 3-D spatial model for in-building wireless networks lies in the proper handling of the shadowing correlation created by the static physical

objects that shape the way wireless signal propagates and attenuates over the Euclidean space. As most of the planar models are designed to study outdoor networks on the scale of a city, the shadowing correlation is typically ignored and path loss is simply modeled through independent log-normal shadowing coefficients [2,3] or a distance dependent function combined with independent fading/shadowing random variables [4, 13]. In contrast, in-building networks are typically much denser and heavily-shadowed by physical objects (floors and walls). The scale of these objects is comparable and often much larger than inter-node distances, resulting in highly-correlated shadowing in space.

This work presents the Poisson grid model, which explicitly handles the shadowing correlation, and is one of the main challenges of in-building network modeling. The Poisson grid is dimension-scalable in that it can be constructed and analyzed for 2-D, 3-D and even higher dimensional networks in a consistent fashion (Sect. 2.3.1, 2.3.2). The prominent application of the Poisson grid is its 3-D version, also referred as the Poisson building, which is particularly useful to study the performance of 3-D wireless networks in large buildings. This model is compatible with the empirically supported lognormal shadowing model in that the marginal shadowing component converges to lognormal distribution as the link distance grows (Sect. 2.3.3).

In this chapter, the tractability of the Poisson building model is provided by explicitly deriving the interference distribution and its spatial correlation (Sect. 2.4, 2.5). This in turn leads to analytical characterizations of the success probability (SINR distributions) of D2D underlay networks and

the coverage probability of in-building cellular networks (Sect. 2.6). Finally, a couple of important variants, namely the finite Poisson building and the semi-infinite Poisson building (Sect. 2.7) are considered. The latter allows one to analyze the interference in a window office, which is a boundary office in a large semi-infinite building. The analysis of these variants further reveals fundamental differences between 3-D and 2-D correlated shadowing analysis.

2.2 System Model

2.2.1 The Poisson Grid

The Poisson grid is constructed on the n-dimensional[2] Euclidean space $\mathbb{R}^n,\ n \in \mathbb{N} \cap [2, \infty)$. It consists of a collection of (hyper-)planes perpendicular to the axes of the Euclidean space. This is a generalization of the (2-D) Manhattan Poisson Line Process (MPLP) [23]. n Cartesian axes are considered and named them $v_1, v_2, \ldots, v_n$. Independent homogeneous Poisson Point Processes (PPP) are built along the $v_1, v_2, \ldots, v_n$-axis, with intensities $\mu_1, \mu_2, \ldots, \mu_n$, respectively. At each point of these processes, an infinite hyperplane grows perpendicular to the axis on which the point is located. This random structure is denoted by $\Psi = \bigcup_{i=1}^{n} \Psi_i$, where Ψ_i is the collection of hyperplanes grown from the points on v_i. This divides the space into infinitely many rectangular boxes or rooms. Fig. 5.1 gives an example of the 2-D (MPLP) and the 3-D (Poisson building) cases.

[2]Below, n will be 2 or 3, but since there is no cost handling the general case, this chapter keeps n general in the model and most of the derivation.

2.2.2 Transmitters on Room Corners and Ceiling Lines

To reflect realistic network deployments, it is assumed that all transmitters (infrastructure nodes, also referred as BSs) are located on some of the one dimensional facets of Ψ, as in [15, 24]. This is inspired by the fact that most real-life wireless infrastructure nodes (small cell BSs or WiFi access points) are often mounted along ceiling lines of rooms or placed at the corners of rooms. Since each intersection line segment meets 2^{n-1} rooms, 2^{n-1} independent transmitter processes are built along each line segment and assign each of them to one adjacent room as in Fig. 2.2. For example, in 2-D as in Fig 2.2, two transmitter processes are built on the wall between room 1 and room 2, with the left one representing the one in room 1 and the right one in room 2.

On the lines parallel to v_i ($i \in [n]$)[3], the transmitters are distributed as a homogeneous PPP with intensity λ_i.[4] The resulting point process (transmitters) is denoted by Φ, which is a stationary Cox point process in $\mathbb{R}^n$. The

[3] [n] is used to denote the set $[1, n] \cap \mathbb{N}$.

[4] Assuming each of the adjacent 2^{n-1} processes having the same density λ_i is only for convenience and can be easily generalized. In fact, as will become obvious later in the chapter, all of the results will stay the same if different densities $\lambda_{i,1}, \lambda_{i,2}, \ldots, \lambda_{i,2^{n-1}}$ to these processes are applied but keep $2^{n-1}\lambda_i = \sum_{j=1}^{2^{n-1}} \lambda_{i,j}$.

mean number of BSs per unit volume[5] is

$$\begin{aligned}\lambda_{avg} &= \frac{\text{(mean number of BSs in a room)}}{\text{(mean volume of a room)}} \\ &= \left(\sum_{i=1}^{n} \frac{2^{n-1}\lambda_i}{\mu_i}\right)\left(\prod_{j=1}^{n} \mu_j\right). \end{aligned} \tag{2.1}$$

2.2.3 Path Loss Model

2.2.3.1 Blockage-Based Path Loss Model

A *blockage-based* path loss model is considered, where the received signal power at y from the transmitter at x ($x, y \in \mathbb{R}^n$) is

$$P_{x\to y} = P_{tx} h \prod_{i=1}^{n} K_i^{N_i}, \tag{2.2}$$

where P_{tx} is the transmit power, h is the channel fading coefficient between x and y, $K_i \in [0,1), i \in [n]$ is the penetration loss of the hyperplanes perpendicular to the v_i axis, and $N_i, i \in [n]$ is the number of hyperplanes grown from the point process on the v_i axis between x and y. To be precise, $N_i = |\overline{xy} \cap \Psi_i|$, where $\overline{xy}$ is the open line segment connecting x and y and $|\cdot|$ denotes the cardinality of a set. Without loss of generality, $P_{tx} = 1$ is assumed, which does not affect the SINR distribution after proper rescaling of the thermal noise power.

One possible concern on this model is the absence of distance-based path loss term. This is justified by the fact that blockage dominates distance-

[5]This will be used in Sect.2.5.3 to compare SIR distribution of our Cox point process model in the Poisson grid and the previous PPP models in *free-space*. (2.1) is the ratio of the mean number of BSs in one room to the mean size of a room.

based loss in indoor environments, which aligns with intuition and is corroborated by ray-tracing studies [25]. However, this path-loss model does not neglect the distance at all. In fact, the exponents N_x, N_y, N_z are functions of the distance between TX and RX. Especially, N_x is a Poisson random variable with mean $\mu_x d\cos(\theta_x)$ where d is $\|TX - RX\|$ and θ_x is angle between the link and x-axis.

2.2.3.2 Compatibility with Log-normal Shadowing

For an arbitrary link $x \to y$ with given Euclidean length $\|x - y\| = d$, and angle (w.r.t. $v_i, i \in [n]$) ϑ_i, N_i is Poisson distributed with mean $\mu_i d\cos(\vartheta_i)$. Thus, the path loss can be rewritten as $\exp\left(-\sum_{i=1}^{n} N_i \log(\frac{1}{K_i})\right)$ where $\log(\frac{1}{K_i}) > 0$. As $\mu_i \to \infty$ or as $d \to \infty$, N_i can be well approximated by a normal random variable. In other words, combining a blockage-based path loss model and the Poisson grid indoor geometry creates a marginal shadowing distribution which is lognormal, and thus connects the model with the data supported lognormal shadowing.

2.2.4 Coverage and Success Probability

This chapter considers two communication scenarios. The first is a *cellular downlink* scenario, and deriving the *coverage probability* $\mathbb{P}[\mathsf{SINR}_c > \theta]$ is considered, where

$$\mathsf{SINR}_c \triangleq \frac{P_{d\to r}}{\sum_{t\in\Phi\setminus\{d\}} P_{t\to r} + \sigma^2}.$$

Here, d is the serving BS, r the receiver, and σ^2 the thermal noise power. This is the probability that a chosen user observes an SINR higher than a threshold θ. As a function of θ, $\mathbb{P}[\mathsf{SINR}_c > \theta]$ can be interpreted as the complementary cumulative distribution function (CCDF) of SINR.

A *D2D underlay* scenario is also considered, where a mobile user attempts to connect to another user using the cellular spectrum. the *success probability*, $\mathbb{P}[\mathsf{SINR}_s > \theta]$, is analyzed where

$$\mathsf{SINR}_s \triangleq \frac{P_{link}}{\sum_{t\in\Phi} P_{t\to r} + \sigma^2},$$

with P_{link} being the received power of the target D2D link.

2.3 Interference in the Typical Room

Define the total interference as the sum of the received power from all transmitters. When the channel coefficients are $h = 1$ (i.e., without fading), the interference is the same at any point of a given room according to our model. Under Rayleigh fading, (i.e., $h \sim \exp(1)$), the interference measured at two points in the typical room is almost surely different due to small-scale fading, but the first moment of interference is the same. This section focuses on the interference in the typical room (formally defined below), and give the moments and the distribution of the total interference.

Precisely, the intersection points of n-orthogonal planes are considered. This stationary point process is denoted by ξ and considered the Palm version of ξ. Under its Palm version, ξ has a point at the origin of $\mathbb{R}^n$. This part

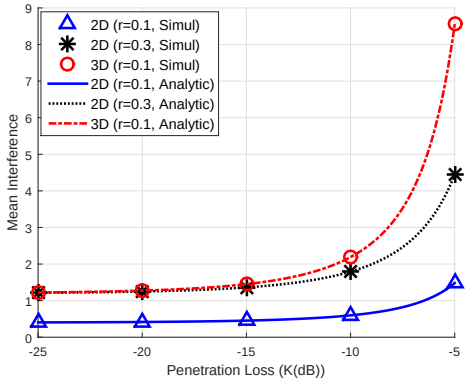

Figure 2.3: Mean interference in the typical room where $r_i = \frac{\lambda_i}{\mu_i} = r$, and $K_i = K$ for $i = 1, 2$ in the 2-D case and $i = 1, 2, 3$ in the 3-D case

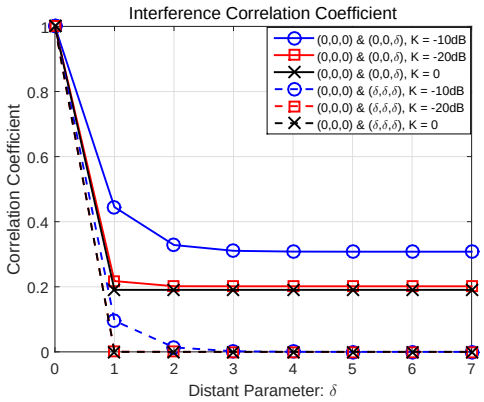

Figure 2.4: Interference Correlation Coefficient between the typical room and room $(0, 0, \delta)$ $(= \rho_{(0,0,\delta)})$ and the typical room and room (δ, δ, δ) $(= \rho_{(\delta,\delta,\delta)})$ in the 3-D case where $r_i = \frac{\lambda_i}{\mu_i} = 0.1$ and $K_i = K$ for $i = 1, 2, 3$

labels rooms by integers of the form $(i_1, i_2, \ldots, i_n) \in \mathbb{Z}^n$. $(0, 0, \ldots, 0)$ is the one containing the origin and located in the positive orthant. This chapter refers to this room as *the typical room*, and label the other rooms by their relative position with respect to the typical room. Intuitively, the typical room is a uniformly randomly chosen room in the Poisson grid.

In the case without fading, the interference observed in room $(i_1, i_2, \ldots, i_n)$ is denoted by $I_{(i_1,i_2,\ldots,i_n)} \triangleq \sum_{x\in\Phi} P_{x\to r}$, where r is any point in room $(i_1, i_2, \ldots, i_n)$.

2.3.1 Interference Moments

Proposition 1 (Mean Interference)**.** In the absence of fading ($h = 1$), the mean interference observed in the typical room is

$$\mathbb{E}[I_{(0,0,\ldots,0)}] = 2^{n-1} \left(\sum_{j=1}^{n} \frac{\lambda_j}{\mu_j}\right) \left(\prod_{i=1}^{n} \frac{1+K_i}{1-K_i}\right).$$

Proof. Let $N_{(i_1,i_2,\ldots,i_n)}$ be the number of the BSs in room $(i_1, i_2, \ldots, i_n)$. Denote the side lengths of this room by $d_{1_{i_1}}, d_{2_{i_2}}, \ldots, d_{n_{i_n}}$ where $d_{j_{i_j}}, (j \in [n])$ are independent exponential random variables with mean $\frac{1}{\mu_j}$, denoting the length of the side parallel to the v_j-axis. For a given structure Ψ,

$$\begin{aligned}\mathbb{E}[N_{(i_1,i_2,\ldots,i_n)}] &= \mathbb{E}[\mathbb{E}[N_{(i_1,i_2,\ldots,i_n)}|\Psi]] \\ &= \mathbb{E}[2^{n-1} \textstyle\sum_{j=1}^{n} \lambda_j d_{j_{i_j}}] = 2^{n-1} \textstyle\sum_{j=1}^{n} \frac{\lambda_j}{\mu_j}.\end{aligned}$$

Since the attenuation from room $(i_1, i_2, \ldots, i_n)$ to the typical room is $\prod_{j=1}^{n} K_j^{|i_j|}$,

$$\begin{aligned}\mathbb{E}[I_{(0,0,\ldots,0)}] &= \textstyle\sum_{(i_t)_{t=1}^{n} \in \mathbb{Z}^n} \mathbb{E}[N_{(i_1,i_2,\ldots,i_n)}] \prod_{j=1}^{n} K_j^{|i_j|} \\ &= 2^{n-1} \left(\textstyle\sum_{j=1}^{n} \frac{\lambda_j}{\mu_j}\right) \left(\prod_{i=1}^{n} \frac{1+K_i}{1-K_i}\right).\end{aligned}$$

The last step comes from the fact that $\sum_{i \in \mathbb{Z}} K^{|i|} = \frac{1+K}{1-K}$. □

Example 1. The mean interference observed in the typical room is $2\left(\prod_{i=1}^{2} \frac{1+K_i}{1-K_i}\right)\left(\sum_{i=1}^{2} \frac{\lambda_i}{\mu_i}\right)$ for $n = 2$, and $4\left(\prod_{i=1}^{3} \frac{1+K_i}{1-K_i}\right)\left(\sum_{i=1}^{3} \frac{\lambda_i}{\mu_i}\right)$ for $n = 3$. In the 3-D case, when there are no BS along the v_3 axis, (i.e. $\lambda_3 = 0$), the ratio of the interference in the 3-D typical room to that of the 2-D typical room is $2\left(\frac{1+K_3}{1-K_3}\right)$. The factor 2 comes from the fact that there are twice more BSs in

any of the v_1, v_2 directions in the 3-D model (*e.g.,* those on the ceiling lines, and those on the floor lines); $\frac{1+K_3}{1-K_3}$ reflects the interference leaked from other floors.

Fig. 2.3 illustrates the mean interference observed by the typical room in the 2-D and the 3-D cases. This part assumes all penetration losses are the same (i.e., $K_i = K,\ \forall i$) and the ratios of the transmitter density to the wall density are identical (i.e. $r_i = \frac{\lambda_i}{\mu_i} = r,\ \forall i$). Since there are more edges in a higher dimensional room, the mean interference of 3-D is larger than that of 2-D, under the same K and r. Also, as K decreases, the mean interference in 3-D decreases faster compared to that of 2-D. As K goes to 0, the hyperplanes shield the interference from other rooms perfectly. So, when $K \to 0$, the mean interference converges to the mean number of the transmitters in the typical room of the Poisson grid.

Proposition 2 (Interference Joint Moment)**.** In the absence of fading (i.e., $h = 1$), the joint moment of the interference between the typical room and room $(i_1, i_2, \ldots, i_n)$ is

$$\begin{aligned}\mathbb{E}[I_{(0,0,\ldots,0)} I_{(i_1,i_2,\ldots,i_n)}] &= 2^{n-1} \left(\sum_{j=1}^{n} \frac{\lambda_j}{\mu_j}\right) \left(\prod_{l=1}^{n} b_l(i_l)\right) \\ &+ 2^{2n-2} \left(\prod_{l=1}^{n} a_l\right) \left(\left(\sum_{j=1}^{n} \frac{\lambda_j}{\mu_j}\right)^2 + \left(\sum_{j=1}^{n} \frac{\lambda_j^2 b_j(i_j)}{\mu_j^2 a_j}\right)\right),\end{aligned}$$

where

$$a_i = \left(\frac{1+K_i}{1-K_i}\right)^2, b_i(x) = K_i^{|x|} \left(|x| + \frac{1+K_i^2}{1-K_i^2}\right),$$

for $i \in [n]$.

Proof. See Appendix 2.8.1. □

Corollary 1 (Interference Variance)**.** By Propositions 1 and 2 with $(i_1, i_2, \ldots, i_n) = (0, 0, \ldots, 0)$, the variance of the interference observed in the typical room is

$$\begin{aligned}\mathrm{Var}[I_{(0,0,\ldots,0)}] &= 2^{n-1}\left(\sum_{j=1}^{n}\frac{\lambda_j}{\mu_j}\right)\left(\prod_{l=1}^{n} b_l(0)\right) \\ &+ 2^{2n-2}\left(\sum_{j=1}^{n}\frac{\lambda_j^2 b_j(0)}{\mu_j^2 a_j}\right)\left(\prod_{l=1}^{n} a_l\right).\end{aligned}$$

***Remark* 1.** Due to the stationarity of the Poisson grid, the correlation coefficient between the typical room and room $(i_1, i_2, \ldots, i_n)$ is $\rho_{(i_1,i_2,\ldots,i_n)} = \mathrm{Cov}[I_{(0,0,\ldots,0)}, I_{(i_1,i_2,\ldots,i_n)}]/\mathrm{Var}[I_{(0,0,\ldots,0)}]$.

Fig. 2.4 shows the interference correlation coefficient in the 3-D case ($\rho_{(0,0,\delta)}$ and $\rho_{(\delta,\delta,\delta)}$) where $\delta \in \mathbb{N} \cup \{0\}$. As expected, when the penetration loss K goes from -10dB to 0 (-∞dB), $\rho_{(0,0,\delta)}$ and $\rho_{(\delta,\delta,\delta)}$ decrease. Furthermore, 1) $\rho_{(0,0,\delta)}$ does not go to zero when $K = 0$ (*i.e.,* no interference leakage between rooms), and 2) $\rho_{(0,0,\delta)}$ does not go to zero even if δ goes to infinity. Both observations can be explained by the correlation of the room sizes along the corresponding axis directions. Intuitively, a large room is more likely next to a large room due to the shared building frame. On the other hand, $\rho_{(\delta,\delta,\delta)}$ goes to zero if K goes to zero and δ goes to infinity as the typical room and room (δ, δ, δ) do not share side(s). This intricate behavior of interference correlations highlights the impact of room size correlation in a typical in-building environment. This impact is well manifested in Fig. 2.4, but is impossible to capture using conventional (free-space) models.

***Remark* 2** (Scale-invariance)**.** By Propositions 1, 2 and Corollary 1, the interference moments of two Poisson grids are the same if the ratios of the transmitter density to the wall density $r_i = \frac{\lambda_i}{\mu_i}, i \in [n]$ as well as the penetration losses $K_i, i \in [n]$ are identical.

2.3.2 Interference Distribution

Proposition 3 (Interference Distribution without Fading)**.** Without fading (i.e., $h = 1$), the Laplace transform of the interference observed in the typical room is

$$\mathcal{L}_{I_{(0,0,\ldots,0)}}(s) = \prod_{k=1}^{n} f\left(s, \frac{\lambda_k}{\mu_k}, \left(K_{(i+k)\equiv n}\right)_{i=0}^{n-1}\right),$$

where $m \equiv n$ denotes m modulo[6] n, and

$$f\left(s, x, (K_i)_{i=1}^{n}\right) = f(s, x, K_1, K_2, \ldots, K_n) = \\ \prod_{i_1 \in \mathbb{Z}} \left(1 + 2^{n-1} x \sum_{(i_p)_{p=2}^{n} \in \mathbb{Z}^{n-1}} (1 - e^{-s \prod_{q=1}^{n} K_q^{|i_q|}})\right)^{-1}.$$

Proof. The Laplace transform of the interference given Ψ is

$$\mathcal{L}_{I_{(0,0,\ldots,0)}|\Psi}(s) = \prod_{k=1}^{n} f_c\left(s, \lambda_k, \left(K_{(i+k)\equiv n}\right)_{i=0}^{n-1}\right),$$

where

$$f_c\left(s, x, (K_i)_{i=0}^{n-1}\right) = \\ \prod_{i_1 \in \mathbb{Z}} \left(2^{n-1} x \sum_{(i_p)_{p=2}^{n} \in \mathbb{Z}^{n-1}} (1 - \exp(-s \prod_{q=1}^{n} K_q^{|i_q|}))\right).$$

[6] In this chapter, the range of modular operation by an integer N is 1 to N.

Since the random variable d_{ij} are i.i.d. exponential, the Laplace transform by deconditioning is obtained with respect to the Poisson grid. $\square$

Let $\tilde{I}_{(i_1,i_2,\ldots,i_n)}$ be the interference in room $(i_1, i_2, \ldots, i_n)$ when the channel is subject to Rayleigh fading.

Proposition 4 (Fading)**.** Under Rayleigh fading ($h \sim \exp(1)$), the Laplace transform of the interference observed in the typical room is

$$\mathcal{L}_{\tilde{I}_{(0,0,\ldots,0)}} = \prod_{k=1}^{n} \tilde{f}\left(s, \tfrac{\lambda_k}{\mu_k}, \left(K_{(i+k)\equiv n}\right)_{i=0}^{n-1}\right),$$

where

$$\begin{aligned}\tilde{f}\left(s, x, (K_i)_{i=1}^{n}\right) &= \tilde{f}(s, x, K_1, K_2, \ldots, K_n) \\ &= \prod_{i_1\in\mathbb{Z}}(1 + 2^{n-1}x \sum_{(i_p)_{p=2}^{n}\in\mathbb{Z}^{n-1}}(1 - \tfrac{1}{1+s\prod_{q=1}^{n} K_q^{|i_q|}}))^{-1}.\end{aligned}$$

Proof. The proof is analogous to that of Proposition 3, except that the interference from room $(i_1, i_2, \ldots, i_n)$ is the sum of i.i.d. exponential random variables with mean $\prod_{m=1}^{n} K_m^{|i_m|}$. $\square$

This part also provides the joint interference distribution at two rooms. Characterizing the joint distribution is important for analyzing the Quality of Service (QoS) of users when they travel across rooms and is non-trivial under the previous stochastic geometric models.

Proposition 5 (Joint Laplace Transform)**.** Under Rayleigh fading (i.e., $h \sim$ Exp(1)), the joint Laplace transform of the interference in the typical room

and in room $(l_1, l_2, \ldots, l_n)$ is

$$\begin{aligned}
&\mathcal{L}_{\tilde{I}_{(0,0,\ldots,0)}\tilde{I}_{(l_1,l_2,\ldots,l_n)}}(s_1, s_2) \\
&= \prod_{k=1}^{n} \tilde{f}_{\mathsf{j}}\left(s_1, s_2, \tfrac{\lambda_k}{\mu_k}, \left(K_{(i+k)\equiv n}\right)_{i=0}^{n-1}, (l_i)_{i=0}^{n-1}\right),
\end{aligned}$$

where

$$\begin{aligned}
&\tilde{f}_{\mathsf{j}}\left(s_1, s_2, x, (K_i)_{i=1}^{n}, (l_i)_{i=1}^{n}\right) \\
=&\tilde{f}_{\mathsf{j}}(s_1, s_2, x, K_1, K_2, \ldots, K_n, l_1, l_2, \ldots, l_n) \\
=&\prod_{i_1 \in \mathbb{Z}} \Big(1 + 2^{n-1} x \sum_{(i_p)_{p=2}^{n} \in \mathbb{Z}^{n-1}} \\
&\left(1 - \frac{1}{1+s_1 \prod_{q=1}^{n} K_q^{|i_q|}} \frac{1}{1+s_2 \prod_{q=1}^{n} K_q^{|i_q - l_q|}}\right)\Big)^{-1},
\end{aligned}$$

and the subscript j stresses the *joint* distribution.

The proof follows the line of thought in [26] and is omitted.

2.4 Interference at a Typical User

At the beginning of Section 2.3, the point process ξ is defined and discussed its Palm distribution. This section is focused on the stationary distribution case or equivalently takes the perspective of the *typical user*. The typical user is located at the origin of the n-dimensional Euclidean space, and the room containing origin has biased size, which is the 3-D analogue of the 1-D bus paradox [27]. Without fading (i.e., $h = 1$), the interference at the typical user is denoted by $I_o \triangleq \sum_{x \in \Phi} P_{x \to o}$, where o is the origin. It is denoted by $\tilde{I}_o$ under Rayleigh fading.

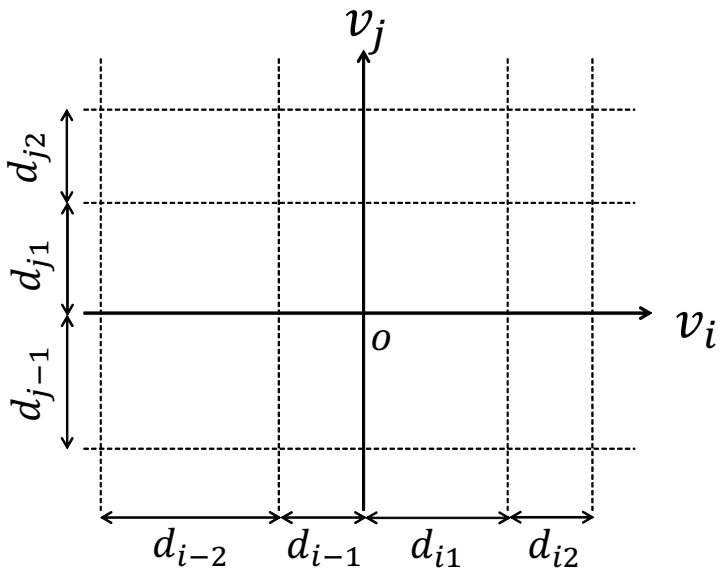

Figure 2.5: Labeling system for Section 2.4

As indicated in Fig. 2.5, a different labeling system is used for the stationary distribution of ξ. The main difference between this labeling system and the one in Section 2.3 is that the size of edges of the room containing o is the sum of two exponential random variables and this room is divided into 2^n *pseudo rooms*. By construction, each of the pseudo rooms has identically, exponentially distributed sides.

2.4.1 Interference Distribution

Proposition 6 (No fading)**.** Without fading, i.e., $h = 1$, the Laplace transform of the interference I_o observed by a typical user is

$$\mathcal{L}_{I_o}(s) = \prod_{k=1}^{n} g\left(s, \tfrac{\lambda_k}{\mu_k}, \left(K_{(i+k)\equiv n}\right)_{i=0}^{n-1}\right),$$

where

$$g\left(s,x,(K_i)_{i=1}^n\right) = g(s,x,K_1,K_2,\ldots,K_n)$$
$$= \prod_{i_1\in\mathbb{N}} \left(1 + 2^{n-1}x \sum_{(i_p)_{p=2}^n \in \mathbb{Z}^{n-1}} \right.$$
$$\left.\left(1-\exp(-s\frac{\prod_{q=1}^n K_q^{|i_q|}}{K_1})\right)\right)^{-2}.$$

Proof. The proof is analogous to that of Proposition 3. The main difference is that the edges of the typical room have lengths distributed like the sum of two exponential random variables. □

By differentiating the formula of Proposition 6, the following result is obtained.

Proposition 7. In the absence of fading, the mean interference observed at the typical user is

$$\mathbb{E}[I_o] = 2^{n-1}\left(\prod_{i=1}^n \frac{1+K_i}{1-K_i}\right)\left(\sum_{j=1}^n \frac{\lambda_j}{\mu_j}\frac{2}{1+K_j}\right).$$

***Remark* 3** (n-D Feller's Paradox [27])**.** By comparing Propositions 1 and 7, the amount of interference observed by the typical user is larger than the interference in the typical room. This result comes from the fact that the size of the typical room is smaller than the room containing the typical user, which makes the user "see" a larger number of strong (near) interferers. More formally, the zero-cell (cell which contains the origin) is chosen with a size bias with respect to the typical cell under Palm distribution, and this favors larger cells, which have in turn more chance to cover a fixed point.

Proposition 8 (Interference Distribution with Fading)**.** Under Rayleigh fading, the Laplace transform of the interference $\tilde{I}_o$ at the typical user is

$$\mathcal{L}_{\tilde{I}_o}(s) = \prod_{k=1}^{n} \tilde{g}\left(s, \frac{\lambda_k}{\mu_k}, \left(K_{(i+k)\equiv n}\right)_{i=0}^{n-1}\right),$$

where

$$\begin{aligned}&\tilde{g}\left(s, x, (K_i)_{i=1}^{n}\right) = \tilde{g}(s, x, K_1, K_2, \ldots, K_n)\\ &= \prod_{i_1 \in \mathbb{N}} (1 + 2^{n-1} x \sum_{(i_p)_{p=2}^{n} \in \mathbb{Z}^{n-1}} (1 - \frac{K_1}{K_1 + s\prod_{q=1}^{n} K_q^{|i_q|}}))^{-2}.\end{aligned}$$

Proof. The proof is analogous to that of Proposition 4 and is omitted. □

2.4.2 Comparison of Correlated and Uncorrelated Shadowing

In classical stochastic geometric models, the shadowing coefficients of different links are modeled using i.i.d. log-normal random variables [2, 3] or depend only on the lengths of each link [4]. In these models, the shadowing correlation is typically ignored. In this subsection, the statistical differences between our correlated model and the distance-based uncorrelated shadowing model are compared. 3-D case will be mainly considered [7], and denoted the interference observed by the typical user under correlated and uncorrelated shadowing by $I_{o,cor}$ and $I_{o,unc}$, respectively.

2.4.2.1 Poisson Grid with *Correlated* and *Uncorrelated* Shadowing

For a fair comparison, the uncorrelated case with the same Cox node distribution as in the Poisson grid model is considered. That is the transmitters

[7] It is possible to generalize this to the n-dimensional case.

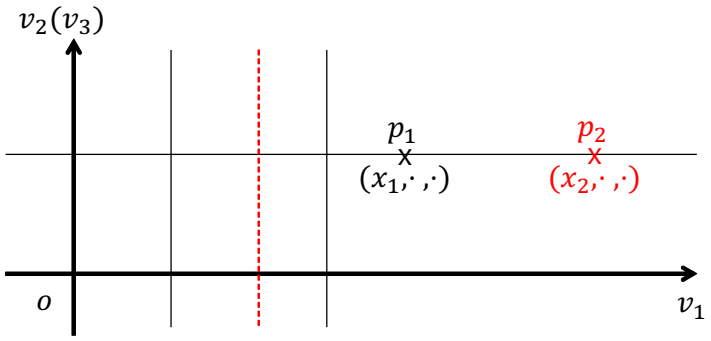

Figure 2.6: Uncorrelated Shadowing model. The number of v_1-orthogonal walls from the origin to p_1 is $Poiss(\mu_1 x_1)$, and to p_2 is $Poiss(\mu_1 x_2)$. With a positive probability, $Poiss(\mu_1 x_1)$ can be larger than $Poiss(\mu_1 x_2)$.

are also distributed on the lines of a Poisson grid made of planes parallel to the axes. In the uncorrelated model, the penetration losses of the transmitters are independently sampled from the marginal distribution of the number of walls that block their link.

Let us first focus on the nodes on the lines parallel to v_1 and denote these nodes by Φ_{v_1}. For each transmitter $x \in \Phi_{v_1}$ with v_1-coordinate x_{v_1}, the number of planes orthogonal to v_1 between this transmitter and the typical user is a Poisson random variable with mean $\mu_1|x_{v_1}|$. To analyze the difference between the correlated and the uncorrelated models, this section considers two transmitters p_1 and p_2 with v_1-coordinates x_1 and x_2 respectively and such that $0 < x_1 < x_2$. In the correlated model, there are always fewer v_1-orthogonal walls between x_1 and the typical user than between x_2 and the typical user, a

property which is not guaranteed under the uncorrelated model (See Fig. 2.6.) The difference can result in non-trivial discrepancies in interference statistics.

2.4.2.2 Mean Interference

From Proposition 7,

Corollary 2. Without fading, in the 3-D case, the mean interference at the typical user under correlated shadowing is

$$\mathbb{E}[I_{o,cor}] = 4\left(\prod_{i=1}^{3}\frac{1+K_i}{1-K_i}\right)\left(\sum_{j=1}^{3}\frac{\lambda_j}{\mu_j}\frac{2}{1+K_j}\right).$$

Proposition 9. Under the 3-D uncorrelated shadowing model without fading, the mean interference observed by the typical user is

$$\mathbb{E}[I_{o,unc}] = \mathbb{E}[I_{o,cor}]. \tag{2.3}$$

Proof. For $x \in \Phi_{v_1}$ with v_1 coordinate x_{v_1}, the expectation of the power attenuation by v_1-orthogonal walls is

$$\sum_{n=0}^{\infty} K_1^n \frac{(\mu_1|x_{v_1}|)^n}{n!} e^{-\mu_1|x_{v_1}|} = e^{-\mu_1|x_{v_1}|(1-K_1)}.$$

Since Φ is the union of independent PPPs, this chapter computes the interference moments from one PPP and aggregate the contributions of all PPPs. By Campbell's formula [5], in the uncorrelated case, the mean interference from the transmitters on one v_1-parallel line such that that there is no v_2 and v_3 orthogonal wall between this line and the origin is

$$\mathbb{E}[I_{\Phi_{v_{11}}}] = \lambda_1 \int_{\mathbb{R}} e^{-\mu_1|x|(1-K_1)}dx = \lambda_1 \frac{2}{\mu_1(1-K_1)},$$

when this chapter denotes these transmitters by $\Phi_{v_{11}}$ and the interference from $\Phi_{v_{11}}$ by $I_{\Phi_{v_{11}}}$. If all transmitters are aggregated on the v_1-parallel lines, the mean interference is

$$\begin{aligned}\mathbb{E}[I_{\Phi_{v_1}}] &= \mathbb{E}[I_{\Phi_{v_{11}}}] \times 4\left(\sum_{i\in\mathbb{Z}} K_2^{|i|}\right)\left(\sum_{j\in\mathbb{Z}} K_3^{|j|}\right) \\ &= \lambda_1 \tfrac{2}{\mu_1(1-K_1)} 4 \prod_{i=2}^{3}\left(\tfrac{1+K_i}{1-K_i}\right) \\ &= 4\left(\prod_{i=1}^{3}\tfrac{1+K_i}{1-K_i}\right)\left(\tfrac{\lambda_1}{\mu_1}\tfrac{2}{1+K_1}\right).\end{aligned}$$

(2.3) is obtained by using the same line of thought, for all transmitters (including transmitters on the lines parallel to the v_2-axis and the v_3-axis). □

2.4.2.3 Variance

From the formula of Proposition 6,

Corollary 3. For the correlated shadowing case, in the absence of fading, the variance of the interference observed by the typical user in the 3-D case is

$$\begin{aligned}\mathrm{Var}[I_{o,cor}] = &\left(\prod_{i=1}^{3}\tfrac{1+K_i}{1-K_i}\right)^2\left(\sum_{j=1}^{3}\tfrac{32(1-K_j)}{(1+K_j)^3}\tfrac{\lambda_j^2}{\mu_j^2}\right) \\ &+\left(\prod_{i=1}^{3}\tfrac{1+K_i^2}{1-K_i^2}\right)\left(\sum_{j=1}^{3}\tfrac{8}{1+K_j^2}\tfrac{\lambda_j}{\mu_j}\right).\end{aligned}$$

Proposition 10. For the 3-D uncorrelated shadowing case, the variance of interference is

$$\mathrm{Var}[I_{o,unc}] = 4\left(\prod_{i=1}^{3}\tfrac{1+K_i^2}{1-K_i^2}\right)\left(\sum_{j=1}^{3}\tfrac{\lambda_j}{\mu_j}\tfrac{1+K_j}{1+K_j^2}\right).$$

Proof. The expectation of the square of the interference from $\Phi_{v_{11}}$ is

$$\begin{aligned}
&\mathbb{E}[I^2_{\Phi_{v_{11}}}] = \mathbb{E}\left[\left(\textstyle\sum_{X\in\Phi_{v_{11}}} e^{-|X|\mu_1(1-K_1)}\right)^2\right]\\
=&\mathbb{E}\left[\left(\textstyle\sum_{X\in\Phi_{v_{11}}} e^{-|X|\mu_1(1-K_1)}\right)\left(\textstyle\sum_{Z\in\Phi_{v_{11}}} e^{-|Z|\mu_1(1-K_1)}\right)\right]\\
=&\mathbb{E}\left[\left(\textstyle\sum_{X\in\Phi_{v_{11}}} e^{-2|X|\mu_1(1-K_1)}\right)\right]\\
+&\mathbb{E}\left[\textstyle\sum_{X,Z\in\Phi_{v_{11}}}^{X\neq Z} e^{-(|X|+|Z|)\mu_1(1-K_1)}\right]\\
=&\lambda_1\textstyle\int_{\mathbb{R}} e^{-2|x|\mu_1(1-K_1)}dx + \lambda_1^2\int_{\mathbb{R}}\int_{\mathbb{R}} e^{-(|x|+|z|)\mu_1(1-K_1)}dxdz\\
=&\lambda_1\textstyle\int_{\mathbb{R}} e^{-2|x|\mu_1(1-K_1)}dx + \left(\lambda_1\int_{\mathbb{R}} e^{-|x|\mu_1(1-K_1)}\right)^2.
\end{aligned}$$

So, the variance of interference from $\Phi_{v_{11}}$ is

$$\mathrm{Var}[I_{\Phi_{v_{11}}}] = \lambda_1\textstyle\int_{\mathbb{R}} e^{-2|x|\mu_1(1-K_1)}dx = \frac{\lambda_1}{\mu_1(1-K_1)}.$$

Since the PPPs on different lines are independent, the variance of the interference from transmitters on the v_1-parallel lines is

$$\begin{aligned}
&\mathrm{Var}[I_{\Phi_{v_1}}] = \mathrm{Var}[I_{\Phi_{v_{11}}}]\times 4\left(\textstyle\sum_{i\in\mathbb{Z}} K_2^{2|i|}\right)\left(\textstyle\sum_{j\in\mathbb{Z}} K_3^{2|j|}\right)\\
&= \frac{\lambda_1}{\mu_1(1-K_1)}4\left(\frac{1+K_2^2}{1-K_2^2}\right)\left(\frac{1+K_3^2}{1-K_3^2}\right).
\end{aligned}$$

□

***Remark* 4.** In general, the variances of the correlated and uncorrelated shadowing cases are different. If $\lambda_2, \lambda_3 = 0$, the variance ratio between the correlated and uncorrelated cases can be simplified into

$$\frac{\mathrm{Var}[I_{o,cor}]}{\mathrm{Var}[I_{o,unc}]} = \frac{2}{1+K_1}\left(1+\frac{4\lambda_1}{\mu_1}\frac{(1+K_2)^3}{(1-K_2)(1+K_2^2)}\frac{(1+K_3)^3}{(1-K_3)(1+K_3^2)}\right). \tag{2.4}$$

Equation (2.4) shows that the tail of $I_{o,cor}$ is heavier than that of $I_{o,unc}$, which aligns with the observation in [28, Corollary 3]. As $\frac{\lambda_1}{\mu_1}$ decreases and K_1 approaches 1,[8] the variance ratio goes to 1. Intuitively this is explained by the fact that in Fig. 2.6, if there is no penetration loss through v_1-orthogonal walls, and the probability that the path loss between the origin and p_1 is larger than that between the origin and p_2 becomes 0. For a special case, when $K_2, K_3 = 0$, (i.e., all v_2, v_3-orthogonal walls totally shield the signal stemming from the next rooms), the ratio becomes $\frac{2}{1+K_1}(1+4\frac{\lambda_1}{\mu_1})$. The factor $\frac{2}{1+K_1}$ shows the effect of the penetration loss of v_1-orthogonal walls and $\frac{\lambda_1}{\mu_1}$ represents the effect of correlated shadowing by common obstacles. As both λ_1 and μ_1 can be arbitrarily configured, (2.4) shows that the two models can yield arbitrarily different variances, highlighting the importance of including correlation.

2.5 Success and Coverage Probabilities

This section derives the coverage probability under the cellular network scenario and the success probability under the D2D underlay scenario, both in Poisson grid networks. The main assumption is that all BSs (and also all D2D links, in the D2D underlay scenario) share the same spectrum. In the cellular network setting, the typical user associates with one of the BSs and the other BSs act as interferers. In the D2D underlay setting, all signals from

[8] K_1 can be arbitrarily close to but not equal to 1, as the derivation used the fact that $\sum_{j\in\mathbb{Z}} K_1^{|j|} = \frac{1+K_1}{1-K_1}$.

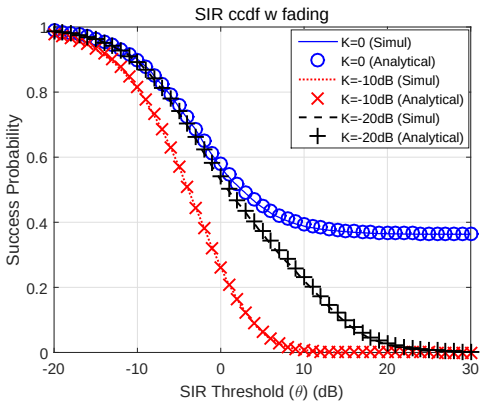

Figure 2.7: In-room link success probability (D2D transmission within room $(0,0,0)$) under the 3-D case, with Poisson building parameters $r_i = \frac{\lambda_i}{\mu_i} = 0.1$, $K_i = K$ for $i = 1,2,3$, and network parameter $\nu = 1$ and $\sigma^2 = 0$.

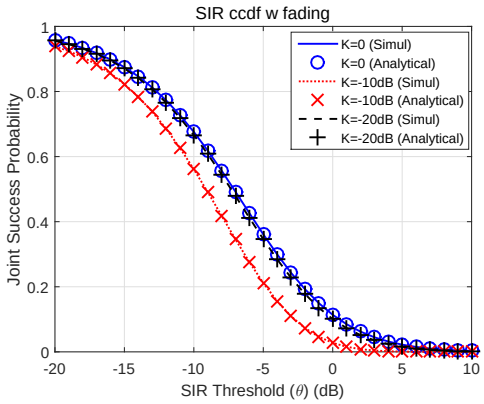

Figure 2.8: In-room link joint success probability (Two D2D links attempt from $(0,0,0)$ to itself) under the 3-D case where Poisson building parameters $r_i = \frac{\lambda_i}{\mu_i} = 0.1$, $K_i = K$ for $i = 1,2,3$, and network parameter $\nu = 1$, $\theta = \theta'$ and $\sigma_1^2, \sigma_2^2 = 0$.

BSs are considered interference.

For the D2D underlay scenario, the results on interference statistics obtained in the previous sections can be directly applied. For the case of cellular networks, the signal from the serving BS should be excluded from interference. First, the D2D underlay case and then the cellular network case under several association scenarios are considered. It is assumed that all D2D transmit powers are equal to P_{tx}/ν (i.e., $P_{link} = 1/\nu$).

2.5.1 Success Probability

2.5.1.1 Success Probability for a Single D2D Link

The labeling system of Section 2.3 is used.

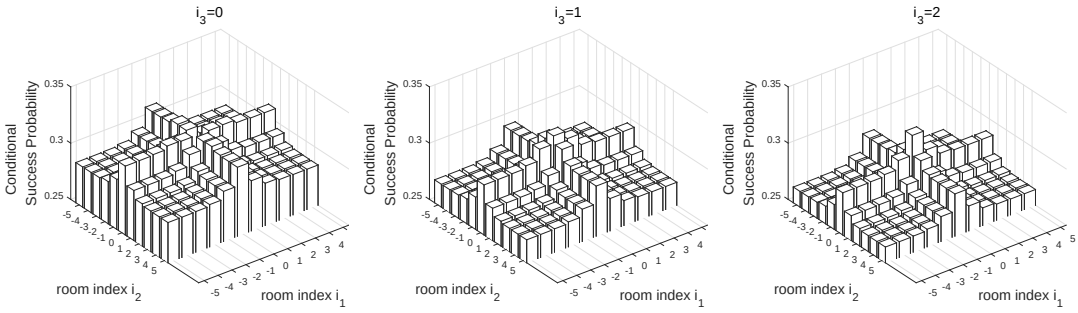

Figure 2.9: Conditional probability that the SINR of a in-room D2D link in room (i_1, i_2, i_3) is larger than $0dB$ given the SINR of a in-room D2D link in the typical room is larger than $0dB$ (i.e. $\mathbb{P}[\mathsf{SINR}_2 > 1 | \mathsf{SINR}_1 > 1]$) when $K_i = -10dB$, $r_i = 0.1$ for $i = 1, 2, 3$, and $\sigma_1^2, \sigma_2^2 = 0$.

Proposition 11. Under Rayleigh fading, the success probability of a D2D transmission from room $(i_1, i_2, \ldots, i_n)$ to room $(0, 0, \ldots, 0)$ is

$$\mathbb{P}[\mathsf{SINR}_s > \theta] = \mathcal{L}_{\tilde{I}_{(0,0,,\ldots,0)}} \left(\frac{\nu\theta}{\prod_{j=1}^n K_j^{|i_j|}} \right) \exp\left(-\frac{\nu\theta\sigma^2}{\prod_{j=1}^n K_j^{|i_j|}} \right),$$

where $\mathcal{L}_{\tilde{I}_{(0,0,\ldots,0)}}(\cdot)$ is given in Proposition 4, θ is the SINR threshold and σ^2 is the thermal noise power.

Proof. Since the path loss model is (2.2), the interference power from room $(i_1, i_2, \ldots, i_n)$ to the typical room is $h \prod_{j=1}^n K_j^{|i_j|}$, where h is an exponential random variable with mean 1, the success probability is

$$\begin{aligned} &\mathbb{P}\left[\frac{h \prod_{j=1}^n K_j^{|i_j|}/\nu}{\tilde{I}_{(0,0,\ldots,0)} + \sigma^2} > \theta \right] = \mathbb{E} \exp\left(\frac{-\nu\theta(\tilde{I}_{(0,0,\ldots,0)} + \sigma^2)}{\prod_{j=1}^n K_j^{|i_j|}} \right) \\ &= \mathcal{L}_{\tilde{I}_{(0,0,,\ldots,0)}} \left(\frac{\nu\theta}{\prod_{j=1}^n K_j^{|i_j|}} \right) \exp\left(-\frac{\nu\theta\sigma^2}{\prod_{j=1}^n K_j^{|i_j|}} \right). \end{aligned}$$

□

Fig. 2.7 illustrates the in-room link success probability when the both transceivers are in $(0,0,0)$ in the 3-D case. $\nu = 1$, $K_i = K$, $r_i = 0.1$ for $i = 1,2,3$ and $\sigma^2 = 0$ are assumed. As K decreases from -10dB to 0 ($-\infty$ dB), the interference power from other rooms is more attenuated and the success probability increases. When $K = 0$, the success probability does not converge to 0 as θ tends to ∞ but converges to the probability that there exists no BS in room $(0,0,0)$.

2.5.1.2 Success Probability for Multiple D2D Links

Multiple D2D communications with normalized transmit powers are considered. For a simple case, there are two D2D links and these links are in-room links (i.e., a pair of TX and RX are in same room).

Proposition 12. Consider two in-room D2D links, one in $(0,0,\ldots,0)$ and the other in $(i_1,i_2,\ldots,i_n) \neq (0,0,\ldots,0)$. Under Rayleigh fading, the probability that the SINRs of two D2D links are larger than θ and θ', respectively, is

$$\mathbb{P}[\mathsf{SINR}_1 > \theta, \mathsf{SINR}_2 > \theta'] = \mathcal{L}_{\tilde{I}_{(0,0,\ldots,0)}\tilde{I}_{(i_1,i_2,\ldots,i_n)}}(\nu\theta, \nu\theta')$$
$$\times \frac{1}{1+\nu\theta\prod_{m=1}^{n} K_m^{|im|}} \frac{1}{1+\nu\theta'\prod_{m=1}^{n} K_m^{|im|}} \exp\big(-\nu(\theta\sigma_1^2 + \theta'\sigma_2^2)\big),$$

where $\mathcal{L}_{\tilde{I}_{(0,0,\ldots,0)}\tilde{I}_{(i_1,i_2,\ldots,i_n)}}(\cdot,\cdot)$ is given in Proposition 5, σ_1^2 and σ_2^2 are the thermal noise powers of the first and the second link respectively. Here, SINR_1 and SINR_2 are the SINRs of the two D2D links. The first term represents the interference from the BSs, the second and third terms the interference between the two D2D links, and the last one the thermal noise, respectively.

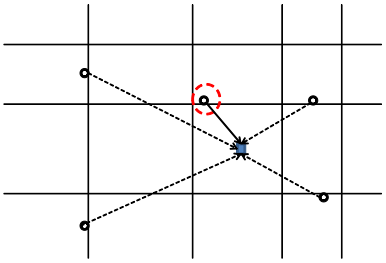

Figure 2.10: Nearest association. The typical user associates with the BS in a red dotted circle which is the (graph-distance) nearest one.

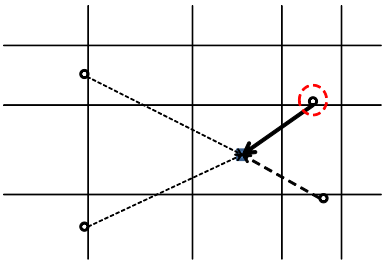

Figure 2.11: Strongest association. The thickness of arrows from BSs to the typical user implies power from each BS. The typical user associates with the BS in the red dotted circle which provides the strongest power.

In Fig. 2.8, the joint in-room success probability of two D2D links is plotted in the 3-D case. As in Fig. 2.7, the joint in-room success probability also increases as K goes from $-10dB$ to 0.

Fig. 2.9 illustrates the conditional probability that the second in-room D2D link (in room (i_1, i_2, i_3)) is successful ($\text{SINR}_2 > 0dB$) given the first D2D in-room link (in the typical room) is successful ($\text{SINR}_1 > 0dB$). The conditional success probability decreases as the room distance increase but in a non-isotropic manner, and the same room distance does not necessarily imply the same conditional success probability due to the intricate spatial interference correlation.[9]

[9]If two D2D links are in the same room (0,0,0), this leads to severe interference between these two links. Due to the randomness of channel fading coefficient, $\mathbb{P}[\text{SINR}_1 > 0dB]$ does not guarantee the highest $\mathbb{P}[\text{SINR}_2 > 0dB]$ when the second link is in the room $(0, 0, 0)$.

2.5.2 Coverage Probability

In this part, the labeling system of Section 2.4 is used. Two scenarios are considered: One is the strongest BS association and the other is the nearest (graph-distance) BS association. If all K_i are the same and there is no fading ($h = 1$), these two scenarios are the same. With fading, the nearest BS is not always the strongest one. These scenarios are illustrated in Fig. 2.10 and 2.11.

2.5.2.1 Strongest BS Association

First, this part consider the case where the typical user associates to the BS which provides the best (strongest) instantaneous signal.

Proposition 13. Under Rayleigh and strongest BS association, the coverage probability is

$$\sum_{k=1}^{n} p(\theta, \lambda_i, \left(K_{(i+k)\equiv n}\right)_{i=0}^{n-1}, 2^{n-1}\left(r_{(i+k)\equiv n}\right)_{i=0}^{n-1}), \tag{2.5}$$

where $\theta > 1$ and

$$\begin{aligned}
&p(\theta, \lambda, \left(K_{(i)\equiv n}\right)_{i=0}^{n-1}, \left(r_{(i)\equiv n}\right)_{i=0}^{n-1}) \\
=&p(\theta, \lambda, K_1, K_2, \ldots, K_n, r_1, r_2, \ldots, r_n) \\
=&2^n \lambda \sum_{j_1 \in \mathbb{N}} \sum_{(j_t)_{t=2}^{n} \in \mathbb{Z}^{n-1}} \exp(-\frac{K_1 \theta \sigma^2}{\prod_{m=1}^{n} K_m^{|jm|}}) \\
&\times \left(1 + r_i \sum_{(l_t)_{t=2}^{n} \in \mathbb{Z}^{n-1}} \frac{1}{1+\prod_{m=2}^{n} K_m^{|jm|-|lm|}/\theta}\right)^{-1} \\
&\times \prod_{m=1}^{n} \big(\prod_{l_m \in \mathbb{N}} (1 + r_m \sum_{(l_t)_{t=1,\ldots,m}^{\neq m} \in \mathbb{Z}^{n-1}} \\
&\frac{1/K_m}{1/K_m + K_1^{|j_1|-|l_1|-1} \prod_{m=2}^{n} K_m^{|jm|-|lm|}/\theta}) ^{-2}\big).
\end{aligned}$$

Here σ^2 is the thermal noise power. If $\theta \leq 1$, the equality in (2.5) should be replaced by $\leq$.

Proof (sketch). For any BS $t \in \Phi$, let $N_1(t), N_2(t), \ldots, N_n(t)$ be the number of hyperplanes between t and the typical user. Let $d \in \Phi$ be the serving transmitter. The aggregated received power from all transmitters except d is

$$I^{!d} = \sum_{t \in \Phi \setminus \{d\}} h_t \prod_{m=1}^{n} K_m^{N_m(t)},$$

where h_t is the channel fading coefficient between transmitter t and the typical user. Then, the coverage probability is

$$\begin{aligned}
&\mathbb{P}[\mathsf{SINR}_c > \theta] = \mathbb{P}(\max \tfrac{h_d \prod_{m=1}^{n} K_m^{N_m}}{I^{!d}+\sigma^2} > \theta) \\
&= \mathbb{E}\mathbb{1}(\max \tfrac{h_d \prod_{m=1}^{n} K_m^{N_m}}{I^{!d}+\sigma^2} > \theta) \\
&\overset{(a)}{\leq} \mathbb{E} \sum_{d \in \Phi} \mathbb{1}(\tfrac{h_d \prod_{m=1}^{n} K_m^{N_m}}{I^{!d}+\sigma^2} > \theta) \\
&= \mathbb{E}[\sum_{d \in \Phi \cup \bar{v}_1} \mathbb{1}(\tfrac{h_d \prod_{m=1}^{n} K_m^{N_m}}{I^{!d}+\sigma^2} > \theta) \\
&+ \ldots + \sum_{d \in \Phi \cup \bar{v}_n} \mathbb{1}(\tfrac{h_d \prod_{m=1}^{n} K_m^{N_m}}{I^{!d}+\sigma^2} > \theta)],
\end{aligned}$$

where h_d is the channel coefficient between d and the typical user, and $\bar{v}_i, i \in [n]$ are the line segments parallel to the v_i axis. (a) comes from the fact that if $\theta > 1$, there is (almost surely) at most one BS serving $\mathsf{SINR} > \theta$ [29]. If the BSs on v_1 are considered in the given structure Ψ, the conditioned expression becomes

$$\begin{aligned}
&\mathbb{E}[\sum_{d \in \Phi \cup \bar{v}_1} \mathbb{1}(\tfrac{h_d \prod_{m=1}^{n} K_m^{N_m}}{I^{!d}+\sigma^2} > \theta) | \Psi] \\
&= 2^{n-1} \lambda_1 \sum_{(j_t)_{t=1}^{n} \in \mathbb{Z}^n}^{j_1 \neq 0} l_{1_i} \mathbb{P}(\tfrac{h_d \prod_{m=1}^{n} K_m^{N_m}}{K_1(I^{!d}+\sigma^2)} > \theta),
\end{aligned}$$

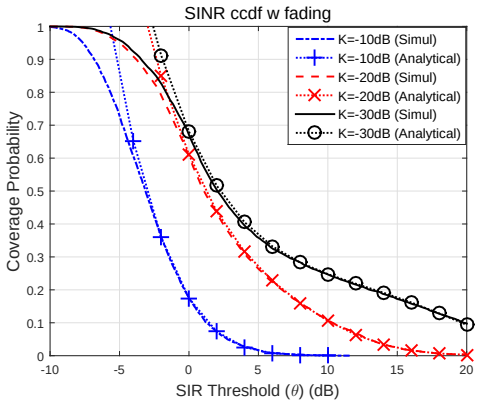

Figure 2.12: Coverage Probability under the 3-D case and the strongest association scenario. $K_i = K$, $r_i = \frac{\lambda_i}{\mu_i} = 0.1$ for $i = 1, 2, 3$ and $\sigma^2 = 0$.

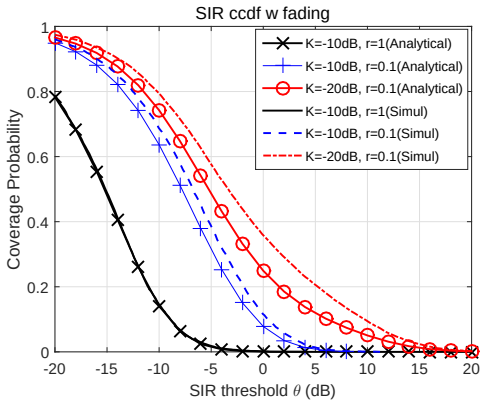

Figure 2.13: Coverage Probability under the 3-D case and the nearest association scenario. $K_i = K$, and $r_i = \frac{\lambda_i}{\mu_i} = r$ for $i = 1, 2, 3$ and $\sigma^2 = 0$.

by Slivnyak's theorem [5, 30] and the construction of the Poisson grid. It is obtained that the result by deconditioning with respect to the Poisson grid, the channel coefficients. □

2.5.2.2 Nearest (Room-Distance) BS Association

In the case where the user connects to the BS with strongest average signal, the BS selection process boils down to finding the nearest (w.r.t. room-distance) BS. More precisely, let $K_i = K, i \in [n]$, and define the graph distance between two rooms as the number of hyperplanes between these rooms. The typical user is associated to the minimal graph distance BS. Denote this distance by δ. If there are several BSs at distance δ, the user associates randomly with one of them.

***Remark* 5.** Given the Poisson grid Ψ and δ, one can compute the coverage

probability in closed form. In the 3-D case, assume $\delta = 0$ and define N to be the number of BSs in the tagged room (or $(0,0,0)$). Then,

$$\mathbb{P}[N = 1|\delta = 0, \Psi] = \textstyle\sum_{i=1}^{12} \lambda_i \times \exp(-\sum_{i=1}^{12} \lambda_i)/P_{tot},$$

where $\lambda_i, i \in [1, 12]$ is the mean number of BSs on the edges of the tagged room and $P_{tot} = \mathbb{P}[\delta = 0|\Psi]$. For the cases $N = 2, 3, \ldots$, it is possible to compute these quantities. So, conditional on the given Poisson grid Ψ, the Laplace transform $\mathbb{E}[e^{-sI}|\Psi, \delta = 0]$ can be computed using Proposition 8 and $\mathbb{P}[N = n|\Psi, \delta = 0]$. The conditional interference Laplace transform under these conditions is given in Appendix 2.8.2.

Proposition 14. Under Rayleigh fading, the coverage probability of a typical user, $\mathbb{P}[\mathsf{SINR}_c > \theta]$ is asymptotically equal to

$$\begin{aligned}
&\textstyle\sum_{m\geq 0} \exp(-\frac{\theta\sigma^2}{K^m}) \\
&\times \left(\textstyle\prod_{i=1}^{m} h_1(m, 2^{n-1}r_i, \frac{\theta}{K^m})^2 - \prod_{i=1}^{m} h_2(m, 2^{n-1}r_i, \frac{\theta}{K^m})^2\right), \qquad (2.6)
\end{aligned}$$

as r_i goes to infinity, where σ^2 is the thermal noise power and

$$\begin{aligned}
&h_1(m, r, s) \\
&= (\textstyle\prod_{i_1\in\mathbb{N}} 1 + r((1 + 2^{m-1}(m + 1 - i_1)(m - i_1)) \\
&\times V_m(i_1) + \textstyle\sum_{(i_t)_{t=2}^n \in \mathbb{Z}^{n-1}}^{i_1+\sum_{t=2}^n |i_t| \geq n+1} (1 - \frac{K}{K+sK^{i_1+\sum_{t=2}^n |i_t|}}))\,)^{-1} \\
&h_2(m, r, s) \\
&= (\textstyle\prod_{i_1\in\mathbb{N}} 1 + r((1 + 2^{n-1}(m + 2 - i_1)(m + 1 - i_1)) \\
&\times V_{m+1}(i_1) + \textstyle\sum_{(i_t)_{t=2}^n \in \mathbb{Z}^{n-1}}^{i_1+\sum_{t=2}^n |i_t| \geq n+1} (1 - \frac{K}{K+sK^{i_1+\sum_{t=2}^n |i_t|}}))\,)^{-1},
\end{aligned}$$

and $V_m(x)$ is 1 if $x = 1, 2, \ldots, m$ and 0 otherwise.

Proof (sketch). Assume there exists at least one BS on a specific line segment. Denote the number of BSs on that line by N and the density by λ. Then, $\mathbb{P}(N = n+1|N > 0) = e^{-\lambda}\frac{\lambda^{n+1}}{(n+1)!(1-e^{-\lambda})}$. As λ increases, this distribution converges to $\mathbb{P}(N = n+1)$, and $\mathbb{P}(N = 0)$ goes to 0. With this result and Proposition 8, it is possible to obtain the asymptotic conditional coverage probability given the Poisson grid, and then obtain (2.6) by deconditioning. □

Fig. 2.13 describes the coverage probability under the nearest room-distance BS association scenario in the 3-D case. It is assumed that $K_i = K$, $r_i = r$ for $i = 1, 2, 3$ and $\sigma^2 = 0$. As r increases, the gap between (2.6) and the simulation result decreases. Fig. 2.13 shows that our expression (2.6) matches well with the simulation result when $r > 0.1$.

***Remark* 6.** For the case of $K = -10dB, r = 0.1$ in Figs. 2.12 and 2.13, the coverage probability under the strongest BS association case is higher than the nearest room distance BS association case, which is inline with intuition. The difference between these two cases provides quantitative guidelines for determining the worthiness of pursuing instantaneous cell reselection.

2.5.3 3-D Free-space and Poisson Building

This subsection provides a justification of our model for in-building networks, by comparing the SIR distribution of a classical stochastic geometric model without correlated shadowing and our new model. Fig. 2.14 compares

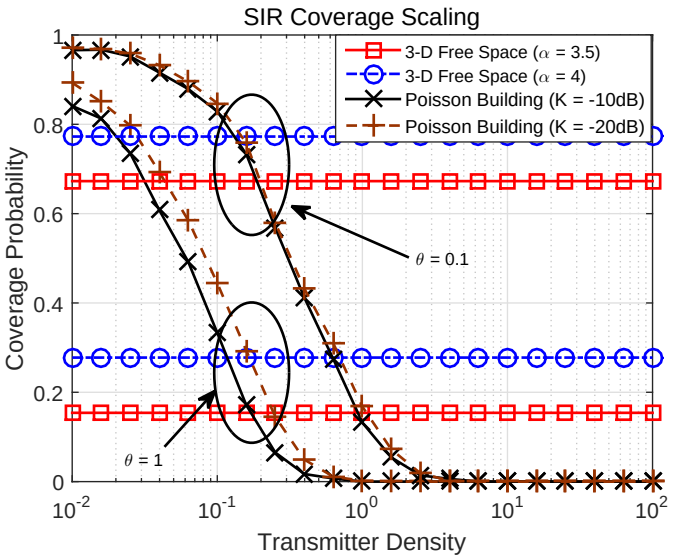

Figure 2.14: SIR coverage scaling over network density under the nearest BS association cases for 3-D free space (PPP) and Poisson building (Cox Point process). The x-axis represents λ_{avg} in (2.1) for Poisson building case and a density λ of a 3-D homogeneous PPP for the 3-D free space case.

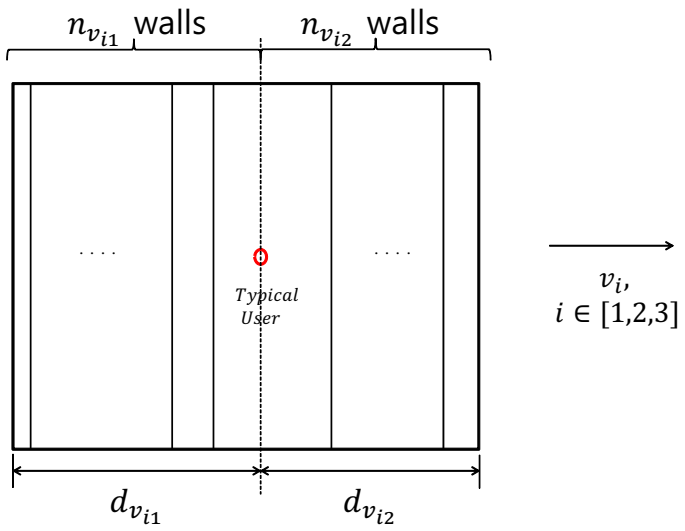

Figure 2.15: A Finite Size Poisson Building. The typical user is located at the origin. Along the v_i-axis ($i \in [1, 2, 3]$), the size of the finite size building is $[-d_{v_{i1}}, d_{v_{i2}}]$ and there are $n_{v_{i1}}$ and $n_{v_{i2}}$ walls in the positive and negative directions, respectively.

the 3-D free space model with distance-based path loss function and the Poisson building with blockage-based path loss function under the nearest BS (or nearest room-distance) association. The free space model is the 3-D extension of the network model in [12] with path loss exponents $\alpha = 3.5, 4$. The Poisson building is constructed with $\mu_i = 1$ and $K_i = -10, -20dB$ for $i = 1, 2, 3$. The average BS density (2.1), $\lambda_{avg} = \mu_1\mu_2\mu_3 \sum_{i=1}^{3} \frac{4\lambda_i}{\mu_i}$, the mean number of BSs per cubic meter in the Poisson building is used.

In the free-space model, the SIR scale invariance, *i.e.,* the fact that the SIR at the typical user does not depend on the infrastructure density, which was observed in 2-D in [12, 20], can be generalized in 3-D as shown in Fig. 2.14, whereas under the *Poisson building* model, the SIR coverage decreases rapidly with the average BS density. Clearly, 3-D in-building model cannot be reduced to a 3-D free-space model from the above observation.

2.6 Finite Poisson Structures

The analysis so far focuses on an infinite network, which circumvents the boundary effects and thus brings extra tractability. While such a modeling approach is justifiable for low dimensionality (2-D) networks, which represent large cities, the boundary effects kick in much sooner in higher dimension (3-D). Fortunately, the Poisson grid model can be tailored to analyze networks of finite sizes (with acceptable loss of tractability). This section analyzes the interference observed by the typical user and compare it with the results Section 2.4.

2.6.1 Finite Size 3-D Poisson Building

It is assumed that the dimension of the building is $[-d_{v_{11}}, d_{v_{12}}]\times[-d_{v_{21}}, d_{v_{22}}]\times[-d_{v_{31}}, d_{v_{32}}] \in \mathbb{R}^3$. As in Fig. 2.15 denote by $n_{v_{11}}$ ($n_{v_{12}}$, $n_{v_{21}}$, $n_{v_{22}}$, $n_{v_{31}}$, $n_{v_{32}}$, resp.), the number of walls between the typical user and building boundary toward $-v_1$ ($+v_1$, $-v_2$, $+v_2$, $-v_3$, $+v_3$, resp.)-axis direction.

Under the finite model as described above, first it is possible to characterize the distribution of the interference measured at the typical user.

Proposition 15. Under Rayleigh fading, the Laplace transform of the interference at the origin in a finite size Poisson building given $d_{v_{ij}} (i \in [1,2,3], j \in [1,2])$ is $\mathbb{E}\left[e^{-sI} | d_{v_{ij}}, I_{v_{ij}}, (i \in [1,2,3], j \in [1,2])\right] =$

$$\sum_{n_{v_{ij}}=1\ldots\infty}^{i=[1,2,3],j=[1,2]} \Big[\prod_{(i,j)} \frac{1}{1+sI_{v_{ij}}K_i^{n_{v_{ij}}}} l(\mu_i, d_{v_{ij}}, \lambda_i, n_{v_{ij}}, n_{v_{(i+1)\equiv 3,(j)\equiv 2}}, n_{v_{(i+1)\equiv 3,(j+1)\equiv 2}}, n_{v_{(i+2)\equiv 3,(j)\equiv 2}}, n_{v_{(i+2)\equiv 3,(j+1)\equiv 2}}, K_i, K_{(i+1)\equiv 3}, K_{(i+2)\equiv 3}, s)\Big],$$

where

$$l(\mu, d, \lambda, n_{v_{11}}, n_{v_{21}}, n_{v_{22}}, n_{v_{31}}, n_{v_{32}}, K_x, K_y, K_z, s) = \frac{\mu^{n_{v_{11}}-1}e^{-\mu d}}{2\pi j} \int_{c-j\infty}^{c+j\infty} \exp(zd) \prod_{i=1}^{n_{v_{11}}} \frac{1}{z+4\lambda \sum_{j=-n_{v_{21}}+1}^{n_{v_{22}}-1} \sum_{k=-n_{v_{31}}+1}^{n_{v_{32}}-1} (1-\frac{1}{1+sK_1^{|i|-1}K_2^{|j|}K_3^{|k|}})} \mathrm{dz}.$$

Proof (sketch). See Appendix 2.8.3. □

Example 2. The special case is considered where $d_{v_{12}}$, $d_{v_{21}}$, $d_{v_{22}}$, $d_{v_{31}}$, $d_{v_{32}}$ $= \infty$. By Proposition 8, Proposition 15 reduces to $\mathbb{E}\left[e^{-sI}|d_{x_1}\right] =$

$$\begin{aligned}
&\textstyle\sum_{n=1}^{\infty} \frac{\mu_1^{n-1} e^{-\mu d_{v_{11}}}}{2\pi j} \int_{c-j\infty}^{c+j\infty} \exp(z d_{v_{11}}) \\
&\times \textstyle\prod_{i=1}^{n} \left(z + 4\lambda_1 \sum_{j,k=-\infty}^{\infty} (1 - \frac{K_1}{K_1 + s K_1^i K_2^{|j|} K_3^{|k|}}) \right)^{-1} \mathrm{dz} \\
&\times \textstyle\prod_{i=1}^{\infty} \left(1 + \frac{4\lambda_1}{\mu_1} \sum_{j,k=-\infty}^{\infty} (1 - \frac{K_1}{K_1 + s K_1^i K_2^{|j|} K_3^{|k|}}) \right)^{-1} \\
&\times \textstyle\prod_{j=1}^{\infty} \left(1 + \frac{4\lambda_2}{\mu_2} \sum_{i,k=-\infty}^{\infty} (1 - \frac{K_2}{K_2 + s K_1^{|i|} K_2^j K_3^{|k|}}) \right)^{-2} \\
&\times \textstyle\prod_{k=1}^{\infty} \left(1 + \frac{4\lambda_3}{\mu_3} \sum_{i,j=-\infty}^{\infty} (1 - \frac{K_3}{K_3 + s K_1^{|i|} K_2^{|j|} K_3^k}) \right)^{-2}.
\end{aligned}$$

This is a simplified version of Proposition 15 with elements from Proposition 8. Fig. 2.16 illustrates the Laplace transform of the interference observed by the typical user when $d_{v_{11}} = 3$, $d_{v_{12}}, d_{v_{21}}, d_{v_{22}}, d_{v_{31}}, d_{v_{32}} = \infty$, $\lambda_1, \lambda_2, \lambda_3 = 0.1$, $\mu_1, \mu_2, \mu_3 = 1$, $K_1, K_2, K_3 = K$. Also it represents the success probability of a D2D link if 1) when D2D link is in the same room with the typical user and 2) the thermal noise power is ignored.

2.6.2 Window Office

In a real environment, even if interference does not penetrate the floors (i.e., $K_3 = 0$), the interference from other floors can enter a room through paths outside the building, *e.g.,* by reflecting on the neighboring buildings. To analyze this type of interference, this chapter proposes a semi-infinite Poisson building which is only deployed on the positive half plane of the v_1-axis. This building has a boundary wall at $v_1 = 0$ and the rooms with this boundary wall

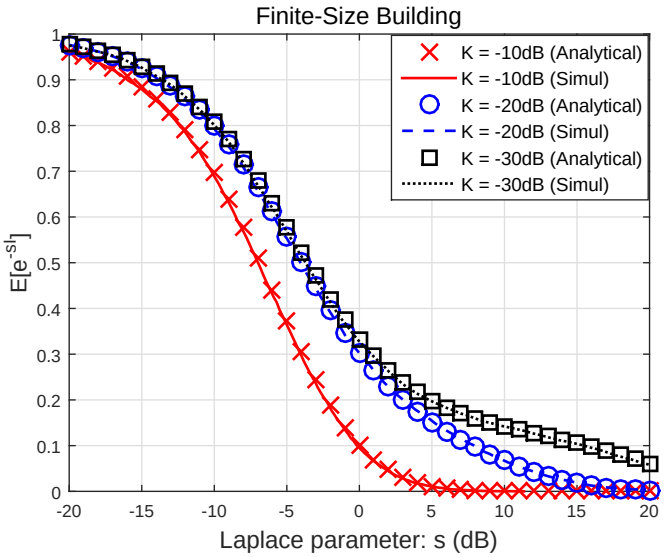

Figure 2.16: Laplace transform of the interference distribution at the typical user when $d_{v_{11}} = 3$, $d_{v_{12}} = d_{v_{21}} = d_{v_{22}} = d_{v_{31}} = d_{v_{32}} = \infty$, $\lambda_i = 0.1$, $\mu_i = 1$, and $K_i = K$ for $i = 1, 2, 3$.

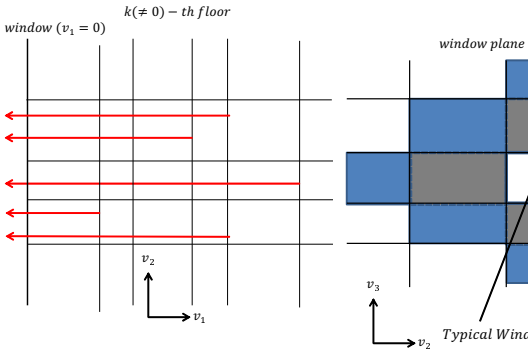

Figure 2.17: A Semi-infinite Poisson Building with the signal paths from a transmitter in room (i, j, k) to the typical window room $(0, 0, 0)$. The left figure describes that signal from a transmitter passes to the outside through the shortest path. The right one describes the graph-distance based path loss model used in the free-space region.

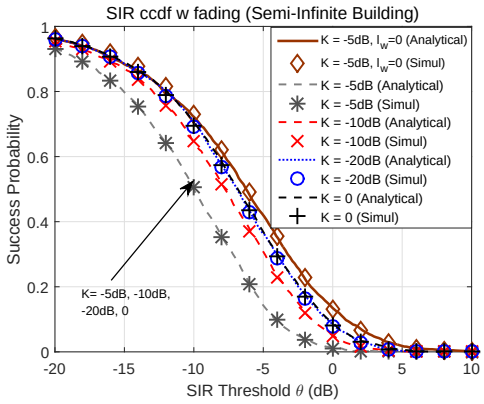

Figure 2.18: In-room link Success Probability (D2D transmission attempts from $(0, 0, 0)$ to itself) in the typical window room of semi-infinite Poisson building. $K_1 = K_2 = K$, $K_3 = 0$, $l_{|x|} = 0.5^x$, $l_w = -3dB$ (except the reference curve without interference from outside the building), $r_i = \frac{\lambda_i}{\mu_i} = 0.1$ for $i = 1, 2, 3$, and $\sigma^2 = 0$.

will be referred as window rooms.

This part chooses a window room which contains the origin of the 3-D Euclidean space and labels this room as $(0, 0, 0)$ (this is the typical room perspective as in Section 2.3), and labels the other rooms according to their relative position with respect to room $(0, 0, 0)$. This part only considers (shortest) graph-distance paths of signals to the outside[10]. For example, if a BS is in room (i, j, k), then a signal from this transmitter predominantly emits to outside through a window room $(0, j, k)$. See the left figure in Fig. 2.17. Since

[10]This is justified by the dominance of penetration loss over free-space loss in indoor.

room sizes in our Poisson building model are random, here a hypothetical path loss function is applied. This chapter defines the path loss from a window room $(0, j, k)$ to $(0, 0, 0)$ through out of building paths to be $l_{|j|+|k|} \in [0, 1]$[11]. Denoting the window loss by l_w, the signal from a BS in room $(i, j, k), k \neq 0$ to the typical window room $(0, 0, 0)$ is $hl_{|j|+|k|}l_w^2 K_1^{|i|}$, where h is the fading coefficient.

Now consider a signal path from a BS on the floor of the typical window room. It is considered that two paths from room $(i, j, 0)$ to $(0, 0, 0)$. The first one is the direct path which penetrates the walls between room $(i, j, 0)$ which contains a BS and the typical window room. The second one is the indirect path which radiates outside of the building through a window room $(0, j, 0)$ and then goes to $(0, 0, 0)$ through the outside. So, the path loss model from room $(i, j, 0)$ to $(0, 0, 0)$ becomes $h_d K_1^{|i|} K_2^{|j|} + h_i l_{|j|} l_w^2 K_1^{|i|}$ where h_d and h_i are channel fading coefficients. With this path loss model, the interference distribution and the success probability can be computed as in Section 2.3 and 2.5.

Denote the interference measured in the typical window room $(0, 0, 0)$

[11]Since the Poisson grid is a discrete random structure, it is hard to combine distance-based functions with it. Instead of this, a general path loss level-set function is taken using graph distance as indicated in the right of Fig. 2.17.

by $\tilde{I}_f$ under Rayleigh fading. The Laplace transform of $\tilde{I}_f$ is

$$\begin{aligned}
&\mathcal{L}_{\tilde{I}_f}(s) = \textstyle\prod_{i\in\mathbb{N}\cup\{0\}}(1+\frac{4\lambda_1}{\mu_1}\sum_{j\in\mathbb{Z}}\sum_{k\in\mathbb{Z}} \\
&(1-\tfrac{1}{1+sK_1^{|i|}K_2^{|j|}K_3^{|k|}}\tfrac{1}{1+sl_{|j|+|k|}l_w^2K_1^{|i|}}))^{-1} \\
&\times\textstyle\prod_{j\in\mathbb{Z}}(1+\frac{4\lambda_2}{\mu_2}\sum_{i\in\mathbb{N}\cup\{0\}}\sum_{k\in\mathbb{Z}} \\
&(1-\tfrac{1}{1+sK_1^{|i|}K_2^{|j|}K_3^{|k|}}\tfrac{1}{1+sl_{|j|+|k|}l_w^2K_1^{|i|}}))^{-1} \\
&\times\textstyle\prod_{k\in\mathbb{Z}}(1+\frac{4\lambda_3}{\mu_3}\sum_{i\in\mathbb{N}\cup\{0\}}\sum_{j\in\mathbb{Z}} \\
&(1-\tfrac{1}{1+sK_1^{|i|}K_2^{|j|}K_3^{|k|}}\tfrac{1}{1+sl_{|j|+|k|}l_w^2K_1^{|i|}}))^{-1}.
\end{aligned}$$

This is obtained by adjusting indices with the new path loss model in Proposition 4. Since $0^0 = 1$, the direct and indirect path losses can be combined as above.

The success probability from room (i, j, k) to room $(0, 0, 0)$ becomes

$$\mathbb{P}[\mathsf{SINR}_s > \theta] = \mathcal{L}_{\tilde{I}_f}\left(\frac{\theta}{K_1^{|i|}K_2^{|j|}K_3^{|k|}}\right)\exp\left(-\frac{\theta\sigma^2}{K_1^{|i|}K_2^{|j|}K_3^{|k|}}\right).$$

Fig. 2.18 plots the in-room link success probability when $K_1, K_2 = K$, $K_3 = 0$, $r_1, r_2, r_3 = 0.1$, $\sigma^2 = 0$, $l_x = 0.5^x$, and $l_w = -3dB$. As K decreases, the total interference from all transmitters decreases and the success probability increases. When $K = 0$, all walls and floors block signals perfectly and interference comes through the outside of building only from transmitters in window offices. For cases $K = 0$, $K = -10dB$, and $K = -20dB$, the success probabilities are almost the same, which suggests that interference coming through the outside dominates the interference coming through the walls in the same floor. By ignoring the interference leakage from through outside of

building paths (*i.e.*, $l_w = 0$), the success probability for $K = -5dB$ is higher than $K = -20dB$ with interference from outside. This shows interference leakage through outside of building paths is an important factor in the 3-D case.

2.7 Conclusions

This chapter propose a Poisson grid based framework for analyzing urban indoor networks. The Poisson grid allows one to model general n-dimensional structures with randomly (but dependently) sized rooms, capturing the fact that more users are located in larger rooms. While the indoor propagation is dominated by shadowing and blockage, the framework facilitates the study of the correlated shadowing field and node distribution, which are one of the distinctive aspects of urban indoor geometry. The interference field associated to this environment is no more a shot noise field, because of common randomness by the shared static obstacles in the Poisson grid.

This chapter obtains exact analytical expressions for the interference field and characterizes the spectral efficiency of two basic communication scenarios in this context. This chapter compares our correlated shadowing field and previous research (uncorrelated shadowing and free-space models) and observe very different moments and scaling laws. Thanks to its finite-size or semi-infinite size 3-D variants, the Poisson grid can be tailored for 1) computing the interference field given the building size and 2) analyzing interference leakage through the outside of the Poisson structure.

The nature of Poisson grid does not allow it to cover all possible building realizations. However, this model opens a new way of analyzing urban indoor networks. Several variants can be derived from it to study more realistic architectural scenarios and wireless technologies. One possible example is representing more complex building structure by removing some line segments in the Poisson grid. Another possible future direction might be considering Matérn-type grids [5,30] for preventing 1) lots of transmitters in a given room or 2) generating too small rooms.

2.8 Appendix

2.8.1 Proof of Proposition 2

Lemma 1. For all $K \in [0,1)$ and $k \in \mathbb{N} \cup \{0\}$,

$$\sum_{i\in\mathbb{Z}} K^{|i|+|i-k|} = K^{|k|}\left(|k| + \tfrac{1+K^2}{1-K^2}\right),$$
$$\sum_{(i,i')\in\mathbb{Z}^2}^{i\neq i'} K^{|i|+|i'-k|} = \left(\tfrac{1+K}{1-K}\right)^2 - K^{|k|}\left(|k| + \tfrac{1+K^2}{1-K^2}\right).$$

Leveraging this lemma, it is possible to obtain the joint moment of the interference between the typical room and room $(i_1, i_2, \ldots, i_n)$.

Let $N_{(i_1,i_2,\ldots,i_n)}$ be the number of the BSs in room $(i_1, i_2, \ldots, i_n)$. Since it is the sum of Poisson random variables, $\mathbb{E}[N_{(i_1,i_2,\ldots,i_n)}N_{(i'_1,i'_2,\ldots,i'_n)}] =$

$$2^{n-1}\left(\sum_{j=1}^n \tfrac{\lambda_j}{\mu_j}\right)\prod_{k=1}^n 1_{i_k=i'_k} + 2^{2n-2}\sum_{j=1}^n \tfrac{\lambda_j^2}{\mu_j^2}1_{i_j=i'_j}$$
$$+ 2^{2n-2}\left(\sum_{j=1}^n \tfrac{\lambda_j}{\mu_j}\right)^2.$$

By leveraging Lemma 1, $\mathbb{E}[I_{(0,0,\ldots,0)}I_{(i_1,i_2,\ldots,i_n)}] =$

$$\begin{aligned}
&\mathbb{E}[\textstyle\sum_{(j_t)_{t=1}^n\in\mathbb{Z}^n}(\prod_{m=1}^n K_m^{|j_m|}N_{(j_1,j_2,\ldots,j_n)})\\
&\textstyle\sum_{(j'_t)_{t'=1}^n\in\mathbb{Z}^n}(\prod_{m=1}^n K_m^{|j'_m-i_m|}N_{(j'_1,j'_2,\ldots,j'_n)})]\\
=&2^{n-1}\left(\textstyle\sum_{j=1}^n\frac{\lambda_j}{\mu_j}\right)(\prod_{l=1}^n b_l(i_l))\\
+&2^{2n-2}(\textstyle\prod_{l=1}^n a_l)\left(\left(\sum_{j=1}^n\frac{\lambda_j}{\mu_j}\right)^2+\left(\sum_{j=1}^n\frac{\lambda_j^2 b_j(i_j)}{\mu_j^2 a_j}\right)\right).
\end{aligned}$$

2.8.2 Interference Laplace Transform Conditioned on $\delta = 0$ and Ψ

In this section, the proof of the formula for coverage probability under the nearest room-distance BS association is provided, conditioned on $\delta = 0$ and the given Poisson grid Ψ.

$$\mathbb{P}[\delta = 0|\Psi] = \textstyle\sum_{n=1}^\infty \mathbb{P}[N = n|\delta = 0, \Psi] = 1 - e^{-\sum_{i=1}^{12}\lambda_i}$$

$$\mathbb{P}[N = 1|\delta = 0, \Psi] = (\textstyle\sum_{i=1}^{12}\lambda_i)\times\exp(-\sum_{i=1}^{12}\lambda_i)/P_{tot}\ldots$$

Combining these results, the interference Laplace transform becomes

$$\begin{aligned}
&\mathbb{E}[e^{-sI}|\delta = 0, \Psi]\\
&= \textstyle\sum_{n=1}^\infty \mathbb{E}[e^{-sI}|N = n, \delta = 0, \Psi]\mathbb{P}[N = n|\delta = 0, \Psi]\\
&= \textstyle\sum_{n=1}^\infty e^{-s\sum_{j=1}^{n-1}h_j}\mathbb{P}[N = n|\delta = 0, \Psi]\\
&\times \textstyle\prod_{i\in\mathbb{N},j,k\in\mathbb{Z},i+|j|+|k|\geq 2} e^{-4\lambda_1(x_i+x_{-i})(1-shK^{|i|+j+|k|-1})}\\
&\times \textstyle\prod_{j\in\mathbb{N},i,k\in\mathbb{Z},|i|+j+|k|\geq 2} e^{-4\lambda_2(y_j+y_{-j})(1-shK^{|i|+j+|k|-1})}\\
&\times \textstyle\prod_{k\in\mathbb{N},i,j\in\mathbb{Z},|i|+|j|+k\geq 2} e^{-4\lambda_3(z_k+z_{-k})(1-shK^{|i|+j+|k|-1})},
\end{aligned}$$

where x_i, y_j, z_k are the dimension of room (i, j, k). The condition $i+|j|+|k| \geq 2$ (or $|i| + j + |k| \geq 2, |i| + |j| + k \geq 2$) implies considering the interference from

the BSs out of the nearest room ($\delta = 0$). By deconditioning w.r.t. the channel coefficients $h \sim \exp(1)$,

$$\begin{aligned}
&\mathbb{E}[e^{-sI}|\delta = 0, \Psi] = \textstyle\sum_{n=1}^{\infty} \left(\frac{1}{1+s}\right)^{n-1} \mathbb{P}[N = n|\delta = 0, \Psi] \\
&\times \textstyle\prod_{i\in\mathbb{N},j,k\in\mathbb{Z}}^{i+|j|+|k|\geq 2} \exp(-2\lambda_h(x_i + x_{-i})(1 - \frac{1}{1+sK^{|i|+j+|k|-1}})) \\
&\times \textstyle\prod_{j\in\mathbb{N},i,k\in\mathbb{Z}}^{|i|+j+|k|\geq 2} \exp(-2\lambda_h(y_j + y_{-j})(1 - \frac{1}{1+sK^{|i|+j+|k|-1}})) \\
&\times \textstyle\prod_{k\in\mathbb{N},i,j\in\mathbb{Z}}^{|i|+|j|+k\geq 2} \exp(-4\lambda_s(z_k + z_{-k})(1 - \frac{1}{1+sK^{|i|+j+|k|-1}})).
\end{aligned}$$

2.8.3 Proof of Proposition 15

Lemma 2. Let $t_1, t_2, \cdots, t_{n-1} \in \mathbb{R}$ be $n-1$ i.i.d. random variables uniformly distributed on $[0, d]$, where $d \in \mathbb{R}^+$. These $n-1$ points divide $[0, d]$ into n intervals of length $y_1, y_2 \cdots, y_n$, where y_1 is the length of left-most interval and y_n is the right-most one. The Laplace transform of $(y_1, y_2, \ldots, y_n)$ is

$$\begin{aligned}
&\mathcal{L}_{y_1,y_2,\cdots,y_n}(s_1, s_2, \ldots, s_n) \\
&= \tfrac{(n-1)!}{d^{n-1}} \tfrac{1}{2\pi j} \textstyle\int_{c-j\infty}^{c+j\infty} e^{zd} \prod_{i=1}^{n} \frac{1}{z+s_i} dz,
\end{aligned}$$

where $c > \mathcal{R}\{s_i\}, \forall i \in [n]$.

Proof. The Laplace transform of $(y_1, y_2, \ldots, y_n)$ is $\mathcal{L}_{y_1,y_2,\ldots,y_n}(s_1, s_2, \ldots, s_n) = \mathbb{E}\prod_{i=1}^{n} e^{-s_i y_i}$. Since the random variables $\{t_i\}$ are i.i.d. with pdf $f_{t_i}(x) = \mathbb{1}_{[0,d]}(x)/d$, the $n!$ possible orders of the $n-1$ random variable happen with equal probability and the Laplace transform can be written as

$$\begin{aligned}
&\mathcal{L}_{y_1,y_2,\ldots,y_n}(s_1, s_2, \ldots, s_n) = \tfrac{(n-1)!}{d^{n-1}} \textstyle\int_0^d \int_0^{x_{n-2}} \int_0^{x_{n-3}} \cdots \int_0^{x_2} \\
&\textstyle\prod_{i=1}^{n} e^{-s_i(x_i - x_{i-1})} dx_1 dx_2 \ldots dx_{n-1},
\end{aligned}$$

where $x_0 = 0$ and $x_n = d$. Let $g_i(x) = e^{-s_i x}$. Then,

$$\mathcal{L}_{y_1,y_2,\ldots,y_n}(s_1, s_2, \ldots, s_n) = \frac{(n-1)!}{d^{n-1}} g_1 * g_2 * \cdots g_n(d),$$

where $*$ denotes convolution. Since $\mathcal{L}_{g_i}(z) = \frac{1}{z+s_i}$,

$$g_1 * g_2 * \cdots * g_n(x) = \frac{1}{2\pi j} \int_{c-j\infty}^{c+j\infty} e^{zd} \prod_{i=1}^{n} \frac{1}{z+s_i} dz,$$

where Mellin's inversion formula is used for the inverse Laplace transform. □

Due to the symmetricity of our network model, only interference coming from the BSs on the line segments which are parallel and negative direction to the v_1-axis is considered and then it is extended to the result without loss of generality. Let $\{\bar{x}_i\}$ be the length of line segments divided by v_1-orthogonal walls. Given $d_{v_{11}}$ and $n_{v_{11}}$ which is the number of v_1-orthogonal walls including the outermost walls, the interference distribution from the transmitters on line segments which are parallel to the v_1-axis and located on the $+v_1$ direction (which is denoted by $\tilde{I}_{f_{11}}$) becomes

$$\mathbb{E}[e^{-\tilde{I}_{f_{11}}} | d_{v_{11}}, n_{v_{11}}, \{\bar{x}_i\}] = \prod_{i=1}^{n_{v_{11}}} \exp(-4\lambda_1 \bar{x}_i$$
$$\sum_{j=-n_{v_{21}}+1}^{n_{v_{22}}-1} \sum_{k=-n_{v_{31}}+1}^{n_{v_{32}}-1} (1 - \frac{1}{1+sK_1^{|i|-1}K_2^{|j|}K_3^{|k|}})),$$

and by deconditioning w.r.t. $\{\bar{x}_i\}$,

$$\mathbb{E}[e^{-\tilde{I}_{f_{11}}} | d_{v_{11}}, n_{v_{11}}] = \frac{(n_{v_{11}}-1)!}{d_{v_{11}}^{n_{v_{11}}-1}} \frac{1}{2\pi j} \int_{c-j\infty}^{c+j\infty} e^{z d_{v_{11}}}$$

$$\prod_{i=1}^{n_{v_{11}}} \frac{1}{z+4\lambda_1 \sum_{j=-n_{v_{21}}+1}^{n_{v_{22}}-1} \sum_{k=-n_{v_{31}}+1}^{n_{v_{32}}-1} (1 - \frac{1}{1+sK_1^{|i|-1}K_2^{|j|}K_3^{|k|}})} dz,$$

where $n_{v_{21}}, n_{v_{22}}, n_{v_{31}}, n_{v_{32}}$ are the numbers of walls along the $-v_2, v_2, -v_3$ and v_3 directions respectively. Since the probability mass function of $n_{v_{11}}$ is $f_{n_{v_{11}}}(k) = \frac{(\mu_1 d_{v_{11}})^{k-1} e^{-\mu_1 d_{v_{11}}}}{(k-1)!}$, by deconditioning w.r.t. $n_{v_{11}}$ and considering interference from all transmitters, the result of Proposition 15 is obtained by considering all BSs in a finite size Poisson building.

Chapter 3

On the Effect of Shadowing Correlation on Wireless Network Performance

This chapter[1] proposes and analyzes a new shadowing field model meant to capture spatial correlations. This chapter shows that the evaluation of the considered metrics under the independent approximation is systematically pessimistic compared to the correlated shadowing model.

3.1 Introduction

3.1.1 Motivation

In wireless system level analysis, most models analyze propagation using distance-based path loss functions [32, 33]. Such a modeling is justified in the free space case but does not capture real-world environments with obstacles. By introducing a shadowing term, it is possible to model the effect of obstacle blockage. This term accounts for the fact that the received signal power is strongly attenuated by obstacles on the propagation path between transmitter and receiver. For a single link, this attenuation is typically modeled by a log-normal distribution [33], which is justified by the multiplicative

[1] This chapter has been published in [31]. I am the primary author of this work. Coauthor Dr. Françcois Baccelli is my supervisor.

blockage loss and the central limit theorem [34]. However, this does neither capture the fact that nearby links are often blocked by *common* obstacles nor the fact that the shadowing statistics highly depend on the spatial geometry of obstacles.

Stochastic geometry has been widely studied to analyze the performance of both infrastructure (e.g., cellular) and infrastructureless (e.g., D2D) networks. The papers in this research field provide highly tractable performance evaluation results in several scenarios. Since shadowing is a significant part of wireless communication, it is important to incorporate this feature in stochastic geometric models. However, as explained above, even though the shadowing effect is spatially correlated in real networks [35], most previous stochastic geometric models assume that shadowing is spatially independent over links.

The main purpose of this chapter is to question this independence assumption and to analyze the effect of correlated shadowing fields when using stochastic geometry. For this, this chapter provides the Laplace transforms of the interference associated with Poisson networks under spatially correlated and independent shadowing assumptions, and prove general ordering relations between them. Using the Laplace stochastic ordering [36], this chapter also gives the ordering of some important performance metrics of the two shadowing models. Especially when the metric is coverage probability, Shannon throughput or local delay, this chapter shows that the performance metric under the independent shadowing is in fact always evaluated in a pessimistic way

compared to the correlated case.

3.1.2 Related Works

3.1.2.1 Correlated Shadowing

In real networks, shadowing fields are spatially correlated [33]. However, few generative or tractable models have been proposed to represent this correlation. Gudmundson proposed the first model of correlation [35] to model the lognormal shadowing random process between a fixed base station and a moving user by an autoregressive process with an exponentially decaying autocorrelation. As a result, the spatial dependence of shadowing can be formulated by joint Gaussian distributions. The multi-base station [37] and multi-hop network [38] cases were also considered based on similar ideas. This approach also forms the basis of the models suggested by the 3GPP [39] and the 802.11 standardization groups [40].

These models have shortcomings. It is hard to give a clear physical interpretation to the joint Gaussian distribution used to model spatially correlated shadowing. These models give limited intuition on large and dense wireless networks. Also, complex simulation platforms are required.

3.1.2.2 Stochastic Geometry and Shadowing Models

Over the past decades, stochastic geometric models, and most notably the planar Poisson point process (PPP) model, have become popular for the analysis of network performance in wireless communications, in both

the D2D [41–44] and the cellular contexts [12, 29, 45]. While an independent shadowing field can easily be incorporated into the basic models [2–4], there is no known approach to combine general stochastic geometry models with correlated shadowing where links at nearby locations can be blocked by the same physical obstacles. Recently, by using a Poisson line process, correlated shadowing fields of urban networks [46, 47] and inbuilding networks [16] have been analyzed in a way taking this correlation into account. However, these models use blockage-based path loss functions and fail taking the distance based-term into account.

3.1.2.3 Comparison of Point Processes

Stochastic comparison tools have been used to investigate the clustering properties among point processes by evaluation of the Ripley K function, the pair-correlation function or the empty space function [48]. To quantify the impact of clustering properties among point processes, the directionally convex order on point processes [49] and the properties of positive and negative association [50, 51] have been proposed. This was for instance used to compare certain point processes with the Poisson point process [52].

This chapter considers a new type of comparison which is that of interference fields when a shadowing random field is introduced to model the blockage effects. The cases where this random field is spatially correlated or not are compared. Other propagation effects such as reflection are not considered.

3.1.3 Problem Statement and Main Contributions

As already explained, most of the previous research papers assigned shadowing variables to links independently by using an empirical distribution [33] or based on link length when topology is incorporated [2–4]. these models will be called (spatially) independent shadowing models.

A typical instance of the independent shadowing model is provided in [4]. Under this model, both the centers of blockages and the base stations are deployed as Poisson point processes. The shadowing random variable of a given link is determined by an independent Poisson random variable with mean proportional to the length of the link.

In contrast, in this chapter, in order to represent the spatial correlation property, some shadowing values based on the obstacle topology are assigned. For example, in Fig. 3.1, obstacles are random segments and the plane is divided into cells in which all base stations are blocked by the same number of obstacles, when seen from the origin. Such cells are not necessarily convex but connected. Another example is depicted in Fig. 3.2, when the base stations form a cluster process. In this network, the same shadowing random variable to the base stations which share the same mother point are assigned. In contrast to the situation of Fig. 3.1, even very close-by points can have different shadowing random variables. This is meant to model the situation where each cluster is located at a different altitude and has different shadowing properties. From these observations, this chapter introduce the concept of *Shadowing cell* where base stations in the same *Shadowing cell* have the same

shadowing random variable. Each base station should not belong to more than one *Shadowing cell*.

The main question of this chapter is the comparison of the interference distribution under the correlated and independent shadowing models in the stochastic ordering sense. To provide a fair comparison, the same marginal shadowing laws are used in both cases. This chapter computes the Laplace transforms of the interference observed by the typical user which is located at the origin under these two models, and then provides the ordering relation of the three metrics for the typical user, i.e., 1) coverage probability, 2) Shannon throughput, and 3) local delay. These three metrics will be shown completely monotone functions of the interference. From well known results on the relation between the Laplace transform ordering and completely monotone functions, the ordering relations are assigned under the two shadowing assumptions.

For the case where base stations form either a homogeneous Poisson point process or a Matérn cluster process on $\mathbb{R}^2$, exact expressions are provided for the Laplace transform of interference. These expressions are provided conditioned on the *Shadowing cells*, but provide a general ordering relation of the above metrics by deconditioning. Especially, if the *Shadowing cells* are Matérn disks [30], further closed form expressions can be obtained by deconditioning with respect to the *Shadowing cells*.

Our key findings can be summarized as follows:

- This chapter provides closed-form expressions for the Laplace transform of the interference measured at the origin under the two shadowing assumptions for some generic network examples.
- This chapter investigates the Laplace transforms of interference and their ordering relationship for point processes with the same point configuration but different joint shadowing distributions.
- By using the Laplace stochastic ordering and the formalism of completely monotone functions, this chapter also give the ordering relation of the three key performance metrics under the two different shadowing assumptions.

3.2 Laplace Stochastic Ordering and Completely Monotone Functions

This chapter first introduces some mathematical preliminaries. The following results and definitions are borrowed from [53]. They will be used to investigate the ordering of the network performance metrics in the next sections.

Definition 1 (Laplace stochastic ordering)**.** Let X and Y be random variables in $\mathbb{R}^+$. X is said to be less than Y in the *Laplace stochastic ordering* (written $X \leq_{\mathrm{L}} Y$), if the Laplace transforms $\mathcal{L}_X(s) = \mathbb{E}[e^{-sX}]$ and $\mathcal{L}_Y(s) = \mathbb{E}[e^{-sY}]$ satisfy

$$\mathcal{L}_X(s) \geq \mathcal{L}_Y(s) \quad \text{for all } s > 0. \tag{3.1}$$

***Remark* 7.** For X, Y which satisfy $\mathcal{L}_X(s) \geq \mathcal{L}_Y(s)$ for all $s > 0$, generally, $\mathbb{E}[X] \leq \mathbb{E}[Y]$ by definition of Laplace stochastic ordering relation. By using Taylor expansion,

$$\mathcal{L}_X(s) = 1 - s\mathbb{E}[X] + \frac{1}{2}s^2\mathbb{E}[X^2] + (\text{higher order terms}),$$
$$\mathcal{L}_Y(s) = 1 - s\mathbb{E}[Y] + \frac{1}{2}s^2\mathbb{E}[Y^2] + (\text{higher order terms}).$$

Since $\mathcal{L}_X(s) \geq \mathcal{L}_Y(s)$ even for very small $s > 0$, we can obtain $\mathbb{E}[X] \leq \mathbb{E}[Y]$. On the contrary, if $\mathbb{E}[X] > \mathbb{E}[Y]$, it is counterintuitive by definition of Laplace stochastic ordering.

Definition 2 (Completely monotone function)**.** A real function f is called *completely monotone* if all its derivatives $f^{(n)}$ exist and satisfy

$$(-1)^n f^{(n)}(x) \geq 0 \quad \text{for all } x \text{ and for all } n = 0, 1, 2, \ldots \tag{3.2}$$

Example 3. The following functions are completely monotone:

$$e^{-\alpha x}, \quad \text{for } \alpha > 0; \quad \frac{1}{(\lambda + \mu x)^\nu}, \quad \text{for } \lambda,\, \mu,\, \nu > 0;$$
$$\ln\left(b + \frac{c}{x+d}\right), \qquad \text{for } b \geq 1,\, c,\, d \geq 0.$$

***Remark* 8.** If $f(x)$ and $g(x)$ are completely monotone functions, so are following functions:

$$af(x) + bg(x), \text{ with } \; a, b \geq 0,$$
$$f(x)g(x), \; f^{(2m)}(x), \; -f^{(2m+1)}(x).$$

The following theorem states the connection between the expectation of completely monotone functions and the Laplace transform order.

Theorem 1. $X \leq_{\mathrm{L}} Y$ holds if and only if

$$\mathbb{E}f(X) \geq \mathbb{E}f(Y), \tag{3.3}$$

for all functions f with a completely monotone derivative, for which the integral exists.

Proof. See [53]. □

3.3 System Model

3.3.1 Network Model, Signal Model and Interference

This chapter considers a generic point process which features an infinite collection of base stations scattered on the 2-dimensional Euclidean space ($\mathbb{R}^2$). Let $\Phi = \{X_i\}$ be the point process giving the locations of base stations. This point process is assumed stationary and with intensity λ. A typical user is located at the origin (o) of $\mathbb{R}^2$. To circumvent technical difficulties, it is assumed that the serving base station of the typical user is not part of the point process, Φ.

A path-loss model based on a distance-based power law is used. The received signal power at y from x ($x \in \mathbb{R}^2$) is

$$P_{x \to y} = P_{TX} h_{xy} S_{xy} d_{xy}^{-\alpha}, \tag{3.4}$$

where P_{TX} is the transmit power, h_{xy}, S_{xy} and d_{xy} are the channel fading coefficient, the shadowing coefficient, and the length of the channel from x to y, respectively. Here, α is the path-loss exponent. $\alpha > 2$ is assumed. Without

loss of generality, $P_{TX} = 1$ is assumed, since this does not affect the signal to interference power plus noise ratio (SINR) distribution after proper rescaling of the thermal noise power. The fading coefficients of different links are assumed independent and it is assumed that all links are subject to Rayleigh fading, which is caused by multipath reception. The channel fading coefficients are hence modeled as exponential random variables, (i.e., $h_{xy} \sim \exp(1)$). A separate term S_{xy} is introduced to model the blockage effect. Since this chapter only computes the sum interference measured at o, for simple notation, h_x, S_x and d_x are used for representing the fading coefficient, the shadowing coefficient, and the distance of channel from x to o.

In previous wireless stochastic geometric research, the shadowing random variable, S_x, is either following a log-normal distribution or is a function of the length of that link which implicitly counts the number of obstacles. However, these assumptions cannot capture common blockages by the same obstacles. In contrast, the correlated shadowing model is obtained by assigning the shadowing random variables in function of the obstacle topology. For example, in Fig. 3.1, there are 2 common blockages between all points of region R_3 and the origin, which defines the correlated shadowing field. One of the main simplifications in this chapter is to only consider blockage and to ignore other effects such as scattering, reflection and so on.

Let $\{R_i\}_{i\in\mathbb{N}}$ be the set of *shadowing cells* in which base stations share a common shadowing random variable to the origin. One example is illustrated in Fig. 3.1. In this example, the shadowing cells are determined by the position

of the end points of the segments. Here, shadowing cells are connected but not necessarily convex. Another example is given in Fig. 3.2, where Φ is a Matérn cluster process. In this example, each R_i is a logical partition which is a set of daughter points sharing a common mother point. It is assumed that each mother point assigns a common shadowing variable to her daughter points. Further, instead of the realization of obstacles, consider a network in which the base stations with the same shadow are clustered. By assigning a shadow random variable T_i which follows the distribution $f_{T_i}(\cdot)$ to all x in R_i, namely by taking $S_x = T_i$ for all $x \in R_i$, it is possible to give different shadowing properties to different clusters.

For a fair comparison between the correlated and the independent shadowing fields, in both models, the same shadowing probability law is used for the points in the same shadow cell. The main difference between these two shadow assumptions is that the shadowing random variables are pathwise the same for all points in the same shadowing cell under the correlated shadowing, while they are i.i.d. under the independent shadowing model.

This chapter provides results for general T_i, but for computational analysis, some specific examples are considered. For example, this chapter will consider the case where the shadowing random variable of all base station in R_i by $T_i = K^{n_i}$ where $K(< 1)$ is the attenuation factor and n_i is the number of obstacles between the typical user and base stations in R_i. Another possible scenario is that where this part picks a representative point for each R_i and assign the shadowing random variable as a function of the link length between

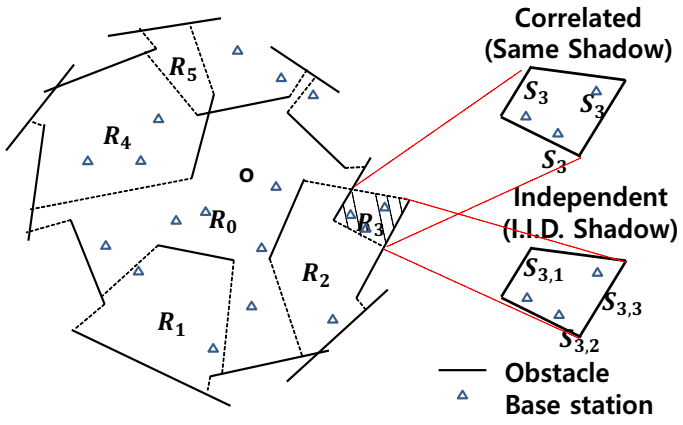

Figure 3.1: A network example with shadowing cells which are generated by line obstacles. Base stations in the same cell share a common shadowing random variable under the correlated shadowing model while base stations have i.i.d. shadowing random variable under the independent shadowing model.

this point and the origin.

Associated with a point process Φ, the interference field measured at the typical user is defined as

$$I(o) \triangleq \sum_{x\in\Phi} P_{x\to o} = \sum_{i} \sum_{x\in\Phi\cap R_i} h_x T_{i,x} d_x^{-\alpha},$$

where $T_{i,x}$ follows the distribution $f_{T_i}(\cdot)$. $T_{i,x}$ is the shadowing coefficient of x seen by the typical user when x is in R_i. Under the correlated model, $T_{i,x} = T_i$ for all x in R_i, while under the independent model, the random variables $T_{i,x}$ are i.i.d. The main comparison results bear on the difference of the distribution of $I(o)$ under independent and correlated S_x.

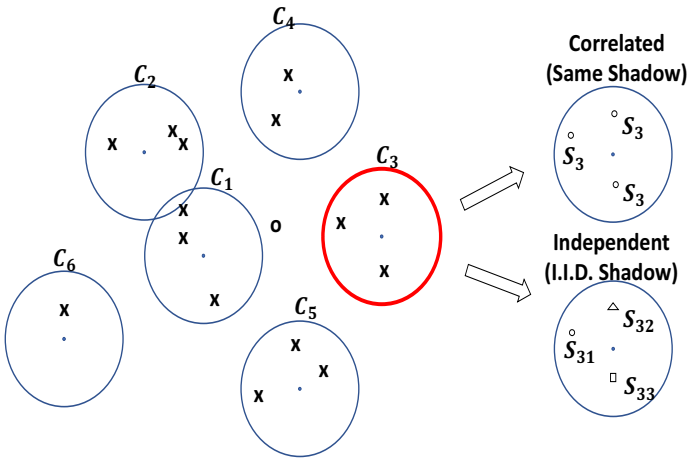

Figure 3.2: A network example based on a Matérn cluster process. In this example, shadowing cells are assumed as the Matérn disks.

3.3.2 SINR Distribution and Performance Metrics

The performance metrics considered in this part are all related to the SINR of the typical user, which is defined as

$$\mathrm{SINR}_o = \frac{P_{\delta \to o}}{\sum_i \sum_{x \in \Phi \cap R_i} h_x T_{i,x} d_x^{-\alpha} + N}. \tag{3.5}$$

Here, δ is the serving base station which is not included in Φ and N is the thermal noise power.

In this chapter, the following metrics are investigated.

3.3.2.1 Coverage Probability

The *coverage probability* of the typical user is

$$\mathbb{P}\left[\mathrm{SINR}_o > T\right], \tag{3.6}$$

where T is some target SINR for reliable communication. This can be thought as 1) the probability that the SINR of a random user exceeds T; 2) the average fraction of the network area within reliable communication at any time. This is the complementary cumulative distribution function (CCDF) of the SINR.

3.3.2.2 Shannon Throughput

The coverage probability is an outage-based metric. However, if a transmitter can adjust its coding rate with respect to the quality of its channel, in the so called adaptive coding case, the *Shannon throughput* [14] is a more relevant quantity. The *Shannon throughput* of the tagged user is

$$\mathbb{E}\left[\log(1+\mathrm{SINR}_o)\right]. \tag{3.7}$$

This can be thought as the expectation of the bit rate of a random user in the network when adaptive coding is used.

3.3.2.3 Local Delay

A packet model is also considered. One of the important metrics in this model is the mean time to transmit a packet, which is referred as the *local delay* [14]. This model requires a time-space structure.

In this setting, the realization of the set of transmitters Φ remains unchanged over time, while channel coefficients vary over time. More precisely, for a sequence of time slots $n = 1, 2, \ldots$, $\Phi(n) = \Phi$, where $\Phi(n)$ is the transmitter process at time n but $h_{\mathbf{xy}}(n)$ for all $\mathbf{x}, \mathbf{y} \in \mathbb{R}^2$ are i.i.d. channel random variables with respect to n.

The local delay given Φ is defined as the first n when the SINR of the typical link at the n-th time is larger than some threshold T, i.e.,

$$L_\Phi = \inf\{n \geq 1 : \mathrm{SINR}_o[n] \geq T|\Phi\}. \tag{3.8}$$

Here, $\mathrm{SINR}_o[n]$ is the typical user's SINR measured at time n:

$$\mathrm{SINR}_o[n] = \frac{h_\delta[n] T_\delta d_\delta^{-\alpha}}{\sum_i \sum_{x \in \Phi \cap R_i} h_x T_{i,x} d_x^{-\alpha} + N}, \tag{3.9}$$

where $h_y[n]$, T_y, d_y are the fading coefficient of the link between y and the typical user at time n, the shadowing random variable of y seen by the typical user, and the link length between y and the typical user, respectively, where $y \in \{x \in \Phi, \delta \text{ (serving base station)}\}$.

3.4 Interference Field of Poisson Shadowing with Common Randomness

This section provides the Laplace transforms of the interference field at the origin under Poisson assumptions for both the correlated and the independent shadowing fields.

There are several types of Poisson networks modeling both cellular and ad-hoc networks. Two types of networks are mainly considered where Φ is modeled by 1) a homogeneous PPP or 2) a Poisson cluster process (PCP). These point processes are widely used to model communication networks [12,54]. The interference measured at the origin under the homogeneous PPP model with the independent and the correlated shadowing are denoted

by $I_{ind,p}(o)$ and $I_{cor,p}(o)$, respectively, and by $I_{ind,c}(o)$ and $I_{cor,c}(o)$ under the homogeneous PCP model. respectively.

3.4.1 Poisson Point Process Network Model

Consider the case where Φ is a homogeneous PPP.

Theorem 2. When Φ is a homogeneous PPP with intensity λ and the channels are subject to Rayleigh fading, the conditional Laplace transforms of $I(o)$ given the shadowing cells $\{R_i\}$ are

$$\begin{aligned}&\mathcal{L}_{I_{ind,p}(o)|\{R_i\}}(s)\\&= \prod_i \exp\left(-\lambda \int_{R_i} \left(1 - \mathbb{E}_{T_i}\left[\frac{1}{1+s\|x\|^{-\alpha}T_i}\right]\right) dx\right),\end{aligned} \tag{3.10}$$

under the independent shadowing assumption, and

$$\begin{aligned}&\mathcal{L}_{I_{cor,p}(o)|\{R_i\}}(s)\\&= \prod_i \mathbb{E}_{T_i}\left[\exp\left(-\lambda \int_{R_i} (1 - \frac{1}{1+s\|x\|^{-\alpha}T_i})dx\right)\right],\end{aligned} \tag{3.11}$$

under the correlated shadowing assumption.

Proof. See [55]. □

Corollary 4. The mean interferences observed by the typical user under the correlated shadowing and the independent shadowing are the same.

$$\mathbb{E}[I_{cor,p(o)}] = \mathbb{E}[I_{ind,p(o)}]. \tag{3.12}$$

The means of the interference fields under the two shadowing assumptions are the same. This substantiates the claim of fairness of the comparison between the two shadowing assumptions.

Corollary 5. The variance of the interferences observed by the typical user under the correlated shadowing and the independent shadowing satisfy

$$var[I_{cor,p}(o)] \geq var[I_{ind,p}(o)]. \tag{3.13}$$

Proof. The mean and variance of a random variable can be obtained by differentiating its Laplace transform at $s = 0$.

$$\mathbb{E}[X] = -\frac{d}{ds}\mathcal{L}_X(s)|_{s=0}, \tag{3.14}$$

$$\begin{aligned} var[X] &= \mathbb{E}[X^2] - (\mathbb{E}[X])^2 \\ &= \frac{d^2}{ds^2}\mathcal{L}_X(s)|_{s=0} - \left(\frac{d}{ds}\mathcal{L}_X(s)|_{s=0}\right)^2. \end{aligned} \tag{3.15}$$

By leveraging these relations, it is possible to obtain the conditional mean and the variance of the interference given the shadowing cell $\{R_i\}_{i\in\mathbb{N}}$ as

$$\begin{aligned} &\mathbb{E}[I_{cor,p}(o)|\{R_i\}_{i\in\mathbb{N}}] = \mathbb{E}[I_{ind,p}(o)|\{R_i\}_{i\in\mathbb{N}}] \\ &= \lambda \sum_{i\in\mathbb{N}} \mathbb{E}[T_i] \int_{R_i} x^{-\alpha} dx, \end{aligned} \tag{3.16}$$

$$\begin{aligned} &var[I_{ind,p}(o)|\{R_i\}_{i\in\mathbb{N}}] \\ &= 2\lambda \sum_{i\in\mathbb{N}} \mathbb{E}[T_i^2] \int_{R_i} x^{-2\alpha} dx + \lambda^2 \sum_{i\in\mathbb{N}} \mathbb{E}[T_i]^2 \left(\int_{R_i} x^{-\alpha} dx\right)^2, \end{aligned} \tag{3.17}$$

$$\begin{aligned} &var[I_{cor,p}(o)|\{R_i\}_{i\in\mathbb{N}}] - var[I_{ind,p}(o)|\{R_i\}_{i\in\mathbb{N}}] \\ &= \lambda^2 \sum_{i\in\mathbb{N}} var[T_i] \left(\int_{R_i} x^{-\alpha} dx\right)^2 \geq 0. \end{aligned} \tag{3.18}$$

(3.12) and (3.13) are obtained by deconditioning with respect to $\{R_i\}_{i\in\mathbb{N}}$. □

***Remark* 9.** When two random variables, X and Y have the same mean but X has bigger variance, the Laplace transform of X is bigger than that of Y

for very small s. This comes from a Taylor series expansion of e^{-x}, and higher order terms are neglected for small s. So, for small s, $\mathcal{L}_{I_{cor,p}}(s) \geq \mathcal{L}_{I_{ind,p}}(s)$. The following and stronger ordering relation are obtained in the next corollary.

Theorem 3. For all $s > 0$,

$$\mathcal{L}_{I_{cor,p(o)}}(s) \geq \mathcal{L}_{I_{ind,p(o)}}(s). \tag{3.19}$$

Proof. This relation simply comes from Jensen's inequality by comparing Equations (3.10) and (3.11). (3.19) is obtained by deconditioning with respect to $\{R_i\}_{i\in\mathbb{N}^+}$. □

***Remark* 10.** From Corollary 5, the difference between $var[I_{cor,p}(o)|\{R_i\}_{i\in\mathbb{N}}]$ and $var[I_{ind,p}(o)|\ \{R_i\}_{i\in\mathbb{N}}]$ is $\lambda^2 \sum_{i\in\mathbb{N}} var[T_i] \left(\int_{R_i} x^{-\alpha} dx\right)^2$. Since $var[T_i] \neq 0$, equality holds if and only if $\left(\int_{R_i} x^{-\alpha} dx\right)^2$. This is achieved when the sizes of each R_i goes to zero. This relates to the fact that when all R_i are very small, all points have independent shadowing random variables almost surely and the model converges to the independent model.

3.4.2 Matérn Cluster Process Network Model

The PCP model is also widely used in wireless communications. Especially in urban networks, users tend to move to hot spot areas and this is quite well represented by PCPs. In this model, it is assumed that the shadowing cells are equivalent to the collection of daughter points sharing the same mother point. This is a quite reasonable assumption since the mother point can be thought as the representative point of that area. As already

explained, two daughter points with different mother points may be close in the Euclidean sense and yet have different shadows; this can be considered as the situation where these transmitters are at different heights and hence have different shadowing.

There are several types of PCP models. In what follows, this part mainly considers the Matérn cluster process. In this model, the daughter points are uniformly located in a disk with radius r_d centered on its mother point. However, the result may be generalized to other PCP models by changing the function $f(\cdot)$. The only assumption on $f(\cdot)$ is that $\int_{\mathbb{R}^2} f(x)dx < \infty$, which means the mean number of daughter points per mother point is finite. $f(\cdot)$ is used below to represent the density of the first moment measure of daughter points relative to their mother point.

The density of the mother point process is denoted by λ_m, and each mother point has some daughter point process which is a nonhomogeneous point process with intensity $\frac{\lambda_d}{\pi r_d^2}$ in a disk of radius r_d centered on the mother point, and 0 outside. So, the density of the PCP is $\lambda_m \lambda_d$.

Let T_y be the shadowing random variable of the shadowing cell centered at y.

Theorem 4. In the Poisson cluster process with independent marks on each cluster, under independent shadowing, the Laplace transform of the interfer-

ence measured at the typical user is

$$\begin{aligned}
&\mathcal{L}_{I_{ind,c(o)}}(s) \\
&= \exp\Bigg(- \lambda_m \int_{\mathbb{R}^2} \Bigg[1 - \exp\Big(- \lambda_d \\
&\int_{\mathbb{R}^2} \big(1 - \mathbb{E}_{T_y}\left[\frac{1}{1 + s(|x+y|)^{-\alpha} T_y}\right]\big) f(x) dx \Big) \Bigg] dy \Bigg),
\end{aligned} \tag{3.20}$$

where

$$f(x) = \begin{cases} \frac{1}{r_d^2}, & \text{if } \|x\| \leq r_d \\ 0, & \text{otherwise.} \end{cases} \tag{3.21}$$

In the Poisson cluster process with under correlated shadowing, the Laplace transform of the interference measured at the typical point is

$$\begin{aligned}
&\mathcal{L}_{I_{cor,c(o)}}(s) \\
&= \exp\Bigg(- \lambda_m \int_{\mathbb{R}^2} \Bigg[1 - \mathbb{E}_{T_y}\Big[\exp\big(- \lambda_d \\
&\int_{\mathbb{R}^2} \big(1 - \frac{1}{1 + s(|x+y|)^{-\alpha} T_y}\big) f(x) dx \big) \Big] \Bigg] dy \Bigg).
\end{aligned} \tag{3.22}$$

Proof. See [55]. □

Theorem 5. As in Theorem 3, it is possible to obtain the following ordering relation by Jensen's inequality.

$$\mathcal{L}_{I_{cor,c(o)}}(s) \geq \mathcal{L}_{I_{ind,c(o)}}(s). \tag{3.23}$$

Corollary 6. The mean interferences observed by the typical user under the

correlated shadowing and the independent shadowing are

$$\begin{aligned}\mathbb{E}[I_{cor,c}(o)] &= \mathbb{E}[I_{ind,c}(o)] \\ &= \lambda_m \lambda_d \int_{\mathbb{R}^2} \int_{\mathbb{R}^2} \mathbb{E}[T_y]|x+y|^{-\alpha} f(x) dx dy. \end{aligned} \tag{3.24}$$

Corollary 7. The variances of the interference observed by the typical user under the correlated shadowing and the independent shadowing are

$$\begin{aligned} var[I_{ind,c}(o)] &= 2\lambda_m \lambda_d \int_{\mathbb{R}^2} \int_{\mathbb{R}^2} \mathbb{E}_{T_y}[T_y^2]|x+y|^{-2\alpha} f(x) dx dy \\ &\quad + \lambda_m \lambda_d^2 \int_{\mathbb{R}^2} \int_{\mathbb{R}^2} |x+y|^{-2\alpha} \mathbb{E}[T_y]^2 f(x) dx dy, \end{aligned} \tag{3.25}$$

$$\begin{aligned} var[I_{cor,c}(o)] &= var[I_{ind,c}(o)] \\ &\quad + \lambda_m \lambda_d^2 \int_{\mathbb{R}^2} \int_{\mathbb{R}^2} |x+y|^{-2\alpha} var[T_y] f(x) dx dy. \end{aligned} \tag{3.26}$$

***Remark* 11.** When $\lambda = \lambda_m \lambda_d$ is fixed, as λ_m increases (or equivalently as λ_d decreases), the variances become the same. Since as λ_d decreases, the shadowing random variable of points become more independent and the correlated model converges to the independent one.

3.5 Performance Metrics Analysis

3.5.1 Coverage Probability

In these network models, this chapter assumes that the serving base station of the typical user, δ, is not included in Φ. It is assumed that the distance between the typical user and δ is d_{link}. The links between $x \in \Phi$ and the typical user are assumed to be subject to Rayleigh fading, whereas the channel between δ and the typical user is subject to any of the following fading conditions.

3.5.1.1 Rayleigh Fading

The instantaneous signal power is an exponential random variable with mean 1. So, the coverage probability under Rayleigh fading is

$$\mathbb{P}[\text{SINR}_o > \theta] = \mathcal{L}_{I(o)}(s)|_{s=\frac{\theta}{d_{\text{link}}^{\alpha}}}. \tag{3.27}$$

3.5.1.2 Rician Fading

Rician fading is similar to Rayleigh fading except for the existence of a dominant component. This component, for instance, can be the line-of-sight wave. When the power ratio of the dominant component over the other component, the so called Rician factor, is κ, the coverage probability is

$$\mathbb{P}[\text{SINR}_o > \theta] = e^{-\kappa} \sum_{n=0}^{\infty} \sum_{l=0}^{n} (-1)^l \frac{\kappa^n}{n!} \frac{s^l}{l!} \frac{d^l}{ds^l} \mathcal{L}_{I(o)}(s)|_{s=\frac{\theta}{d_{\text{link}}^{\alpha}}}, \tag{3.28}$$

which comes from the CCDF of Rician distribution.

Since the Laplace transform of a random variable X, $\mathcal{L}_X(s) = \mathbb{E}[e^{-sX}]$, is a completely monotone function, from Remark. 8, the expressions in Equations (3.27), (3.28) are also completely monotone functions. So, it is possible to apply Theorem 1 to get the following ordering relations of coverage probabilities under these fading cases.

Theorem 6. When the channel fading of the signaling link is Rayleigh or Rician, the coverage probability under correlated shadowing is better than under independent shadowing for all $\theta \geq 0$:

$$\mathbb{P}[\text{SINR}_{o,cor} > \theta] \geq \mathbb{P}[\text{SINR}_{o,ind} > \theta], \tag{3.29}$$

where $\text{SINR}_{o,cor}$ and $\text{SINR}_{o,ind}$ are the SINR measured at the typical user under the correlated and the independent shadowing field, respectively.

3.5.2 Shannon Throughput

Shannon throughput is one more example of completely monotone functions of interference. The following ordering result then follows:

Theorem 7. The mean Shannon throughput is always larger under the correlated shadowing than under the independent shadowing, i.e.,

$$\mathbb{E}[\log_2(1+\text{SINR}_{o,cor})] \geq \mathbb{E}[\log_2(1+\text{SINR}_{o,ind})]. \tag{3.30}$$

3.5.3 Local Delay

Lemma 3. Let $I = \sum_{X_i \in \Phi} G_i / l(|X_i|)$ denote the spatial interference field measured at the typical user, where Φ is some homogeneous PPP with intensity λ on $\mathbb{R}^2$, $\{G_i\}$ are i.i.d. random variables with Laplace transform $\mathcal{L}_G(s)$ and $l(r)$ is any response function. Let $\mathcal{L}_I(s|\Phi) = \mathbb{E}[e^{-sI}|\Phi]$ denote the conditional Laplace transform of I given Φ. Then,

$$\mathbb{E}\left[\frac{1}{\mathcal{L}_I(s|\Phi)}\right] = \exp\left(-2\pi\lambda \int_0^\infty v\left(1 - \frac{1}{\mathcal{L}_G(s/l(v))}\right) dv\right). \tag{3.31}$$

The proof can be found in [14].

The local delay expression is given under fast Rayleigh fading. Fast Rayleigh fading is the case where fading coefficients are resampled at every time slot.

Theorem 8. Under the network Φ with fast Rayleigh fading, the local delay of the tagged user is

$$\mathbb{E}[L_\Phi] = \exp(N\theta d_{d_{\text{link}}}^{-\alpha}) \left(\mathcal{L}_{I(o)}(\theta {d_{\text{link}}}^{-\alpha})\right)^{-1}, \tag{3.32}$$

where N is the thermal noise power, $l(\cdot)$ is the path-loss function and d_{link} is the distance between the typical receiver and its associated transmitter.

Proof. In the fast Rayleigh fading case,

$$\mathbb{P}[F d_{\text{link}}^{-\alpha} \geq \theta(N + I(o))] = \exp(-N\theta d_{\text{link}}^{-\alpha}) \mathcal{L}_{I(o)}(\theta d_{\text{link}}^{-\alpha}),$$

where F is the Rayleigh fading coefficient of the serving base station with mean 1. So, the conditional expectation of the local delay given Φ is

$$\begin{aligned}
\mathbb{E}[L_\Phi] &= \sum_{n\geq 1} \mathbb{P}[L \geq n|\Phi] \\
&= \sum_{n\geq 1} (1 - \exp(-N\theta d_{\text{link}}^{-\alpha}) \mathcal{L}_{I(o)}(\theta d_{\text{link}}^{-\alpha}))^{n-1} \\
&= \exp(N\theta d_{\text{link}}^{-\alpha}) \left(\mathcal{L}_{I(o)}(\theta d_{\text{link}}^{-\alpha})\right)^{-1}.
\end{aligned} \tag{3.33}$$

□

Corollary 8. From Theorem. 8, it is possible to conclude that

$$\mathbb{E}[L_{I_{cor}(o)}] \leq \mathbb{E}[L_{I_{ind}(o)}], \tag{3.34}$$

since the local delay is proportional to the inverse of the Laplace transform.

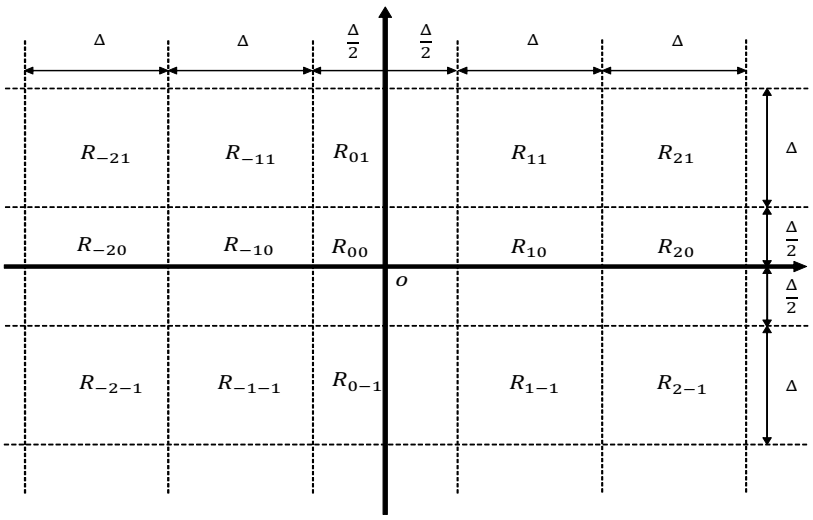

Figure 3.3: An example of random division of $\mathbb{R}^2$.

3.6 Computational Results

3.6.1 Comparison Settings

3.6.1.1 Poisson Point Process on Grid Shadowing Tessellations

For the shadowing tessellation case, this part focuses on the example of Fig. 3.3, where $\{R_i\}$ consists of squares with length Δ and the origin is located at the center of one square.

Three cases are considered: $\Delta = 1, 5, 15$ with $\alpha = 4$, $\lambda = 1$, $K = 0.1$. For the correlated shadowing model, as Δ increases, more points will be in a square, which implies more points will share the same shadowing random variable. As Δ goes to zero, the shadowing random variables of different points become independent and the model converges to that in [4].

Denote the square which contains the origin by R_{00}, and label the other squares by their relative positions with respect to R_{00} as on Fig. 3.3. The shadowing random variable of R_{ij} is assigned by T_{ij} and assumed $T_{ij} = K^{r_{ij}}$, where $0 \leq K \leq 1$ and r_{ij} is a Poisson random variable with mean $\lambda_b \Delta \sqrt{i^2 + j^2}$. Here, K is the attenuation factor when signal crosses an obstacle, and r_{ij} is the number of obstacles between the origin to any point in R_{ij}. In numerical evaluation, $K = 0.1$ is assumed. The underlying assumptions on r_{ij} are that the number of obstacles is Poisson distributed for a given link, as in [4]; λ_b is the implicit obstacle density and $\Delta \sqrt{i^2 + j^2}$ is the distance between the center of R_{ij} which is the representative point of R_{ij} and the origin. Here, $\lambda_b = 1$.

For the independent shadowing model, it is assumed that the shadowing random variables of points in R_{ij} are i.i.d. with distribution that of $K^{r_{ij}}$ instead of assigning one T_{ij} to all points in R_{ij}.

Further, the distance from the typical user to its serving base station, d, is assumed to be 0.5 and it is assumed that there is no obstacle between the typical user and its serving base station. The Rayleigh fading case is only considered.

In the following part, I provide the justification of how I chose the values of each parameter.

First of all, $K = 0.1$ comes from the typical penetration loss of brick walls at 1.8$\sim$2.6GHz. The values of λ_b, λ_{BS} and d are not from real network parameters. The followings are main rationale for choosing $\lambda_b = 0.5$, $\lambda_{BS} = 1$,

and $d = 0.5$.

1. In Figure 3.3, R_{00} is LOS region when the shadowing probability law for R_{ij} is $f_{R_{ij}}(\cdot) = K^{r_{ij}}$ where r_{ij} is a Poisson random variable with a mean $\lambda_b \Delta \sqrt{i^2 + j^2}$ where Δ is the height of each square. Since I assume the serving signal is not affected by the shadow, I want to locate the serving base station in R_{00}. Since the minimum Δ in my presentation was 1, I chose $d = 0.5$.

2. I designed Δ to investigate the following cases: A) many base stations share the same shadowing random variables and B) most base stations do not share the same shadowing random variable. When λ_{BS} is fixed, these cases can be generated by changing Δ. I assigned $\lambda_{BS} = 1$, and it is possible to make the second case with $\Delta = 1$ and the first case with larger Δ. Basically, I randomly chose λ_{BS}, Δ, and λ_b, but these parameters are scalable especially for interference-limited networks.

***Remark* 12** (log-normal compatibility)**.** With some examples of shadowing cells, $\{R_{ij}\}$, and their associated shadowing probability laws, $f_{T_{ij}}(\cdot)$ including the example in Figure 3.3, the path loss model is compatible with the lognormal shadowing model in the following sense. The received power at the origin form $x \in R_{ij}$ is

$$\begin{aligned} P_{x \to o} &= S_x h_x \|x\|^{-\alpha} \\ &= K^{r_{ij}} h_x \|x\|^{-\alpha} \\ &= \exp(r_{ij} \log(K)) h_x \|x\|^{-\alpha}, \end{aligned}$$

where r_{ij} is a Poisson random variable with a mean $\lambda_b \Delta \sqrt{i^2 + j^2}$. As λ_b or i, j goes to infinity, r_{ij} can be well approximated by a normal random variable and this model is hence compatible with a lognormal shadowing distribution asymptotically.

3.6.1.2 Matérn Cluster Shadowing Cell

For the correlated shadowing model, the common shadowing random variable of daughter points of the i-th mother point is denoted by T_i. $T_i = K^{r_i}$ is assumed where $0 \leq K \leq 1$ and r_i is a Poisson random variable with mean $\lambda_b |X_i|$ where $|X_i|$ is the distance between X_i and the origin. As in Sec. 3.4.1, the shadowing random variable of a daughter point of the i-th mother point is an i.i.d. Poisson random variable with mean $\lambda_b |X_i|$. In numerical evaluation, $\lambda_b = 1$ and $K = 0.1$ are assumed. For the link between the typical user and its serving base station, it is assumed that its length is 0.5 and that it is subject to Rayleigh fading with no blockage.

In order to compare interference among networks with the same density but different amounts of the correlation, this part fixes the base station density by taking $\lambda_m \lambda_d = 1$ and varies $\lambda_d = 1, 5, 10$. Under correlated shadowing, as λ_d increases, more transmitters are in the same shadowing cell and the amount of common randomness also increases. Further, $r_d = 1$.

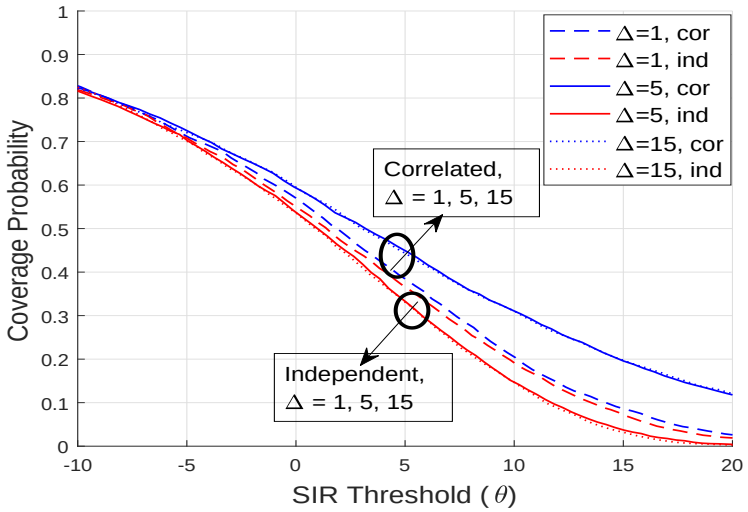

Figure 3.4: Coverage Probability under the model in Sec. 3.4.1. The link distance is 0.5 and $\Delta = 1, 5, 15$.

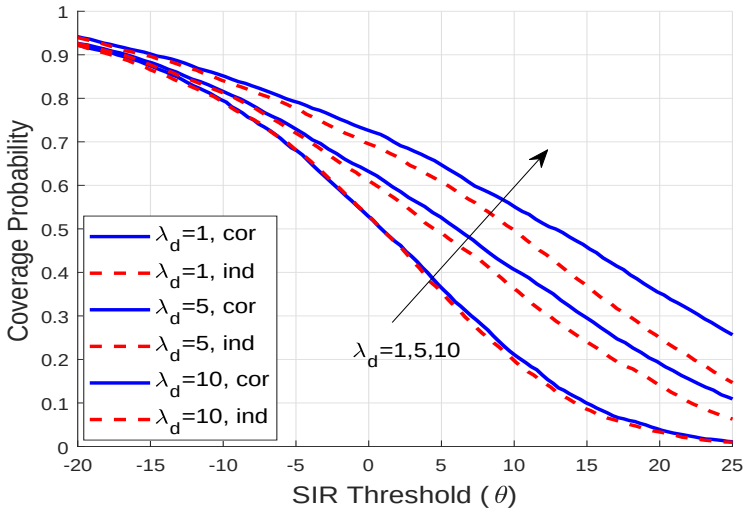

Figure 3.5: Coverage Probability under the model in Sec. 3.4.2. The link distance = 0.5 and $\lambda_d = 1, 5, 10$.

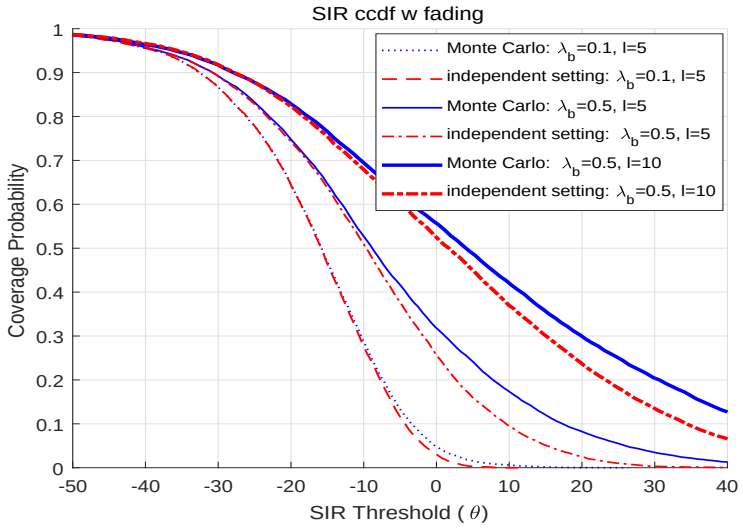

Figure 3.6: Comparison of coverage probability for Fig. 3.1 under Monte Carlo simulation and independent link assumption where $\lambda = 1$, $K = 0.01$, $N = 0$.

3.6.2 Interpretations of Simulation Results

3.6.2.1 Coverage Probability

Fig. 3.4 and 3.5 illustrate the coverage probabilities under the model in Sec. 3.6.1.1 and Sec. 3.6.1.2, respectively. Two facts are observed from these simulation results which are in line with or extending our mathematical derivations:

- the coverage probability under the correlated shadowing is larger than that under the independent shadowing, which confirm what is proven in Theorem. 6, and
- the gap of coverage probabilities between correlated and independent settings decreases as Δ and λ_d decrease.

***Remark* 13.** In Remark 10 and 11, it was shown that the variance of the correlated model converges to that of the independent model as the sizes of all R_i or λ_m decrease. From Fig. 3.4 and 3.5, it is possible to observe more general results about the convergence of higher order moments of interference between the two shadowing assumptions. The coverage probability is proportional to the Laplace transform with some positive argument when the link between the typical user and the serving base station is subject to Rayleigh fading, since

$$\mathbb{P}[\frac{hd_{\text{link}}^{-\alpha}}{I+N} > T] = e^{-d_{\text{link}}^{\alpha}N} \times \mathcal{L}_I(s)|_{s=Td_{\text{link}}^{\alpha}},$$

where $h \sim \exp(1)$ is the channel fading coefficient. In Fig. 3.4 and 3.5, the gap of coverage probability between the two shadowing assumptions is reduced as Δ (equivalently R_i) decreases or λ_d decreases. From these experimental results, it is possible to see that the Laplace transforms (or equivalently higher order moments) of the interference of the two shadowing models become asymptotically similar.

Now, this chapter provides the coverage probability results of the well known network example which is discussed in [4]. The base stations form a homogeneous PPP with a density λ, and the obstacles are represented by a Boolean model [5], where the centers of obstacles are distributed as a homogeneous PPP with intensity λ_b. It is assumed that the obstacles are line segments with length l. See Fig. 3.1. For this network, the path loss model presented in (3.4) is used under both the correlated and the independent shadowing. Further, it is assumed that the shadowing random variable of base station $x \in \Phi$

seen by the typical user is K^{N_x}, where $0 < K < 1$ is the attenuation factor and N_x is the number of obstacles on the path between x and the typical user.

In Fig. 3.6, the simulation results on the independent setting and the Monte Carlo simulation of the ground truth are given. Under the independent setting, N_x is distributed as a Poisson random variable with a mean $\frac{\lambda_b \times (\text{link length of } \overline{ox})}{2\pi}$. Under the Monte Carlo simulation, all base stations and obstacles are deployed, and N_x is counted for each $x \in \Phi$ of the realized network. For both cases, $\lambda = 1$, $K = 0.01$, $N = 0$ are assumed and the cases with $(\lambda_b, l) = (0.1, 5)$, $(0.5, 5)$, and $(0.5, 10)$ are considered. Also, it is assumed that all channels are subject to Rayleigh fading. Further, $d_{\text{link}} = 0.5$ with no obstacles is assumed.

Again, from Fig. 3.6, it is possible to see that the coverage probability under the correlated model is better than that under the independent approximation. Also, as λ_b or l increase, the coverage probability becomes larger since more interference power is blocked by obstacles. For a quantitative result, the case with $(\lambda_b, l) = (0.5, 5)$ is considered. In this case, the Monte Carlo simulation of the ground truth compared to the independent approximation is 23% better at 0dB and 79% better at 10dB.

3.6.2.1.1 Numerical Validation

Figures 3.7 and 3.8 show the comparison of coverage probabilities under 1) the real obstacles (line segments with a length $\frac{2}{\pi}$ for a fair comparison) deployment 2) the independent shadowing field and 3) the correlated shadow-

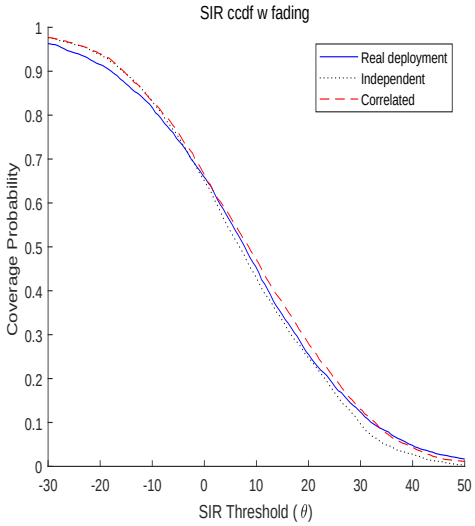

Figure 3.7: $\Delta = 1$

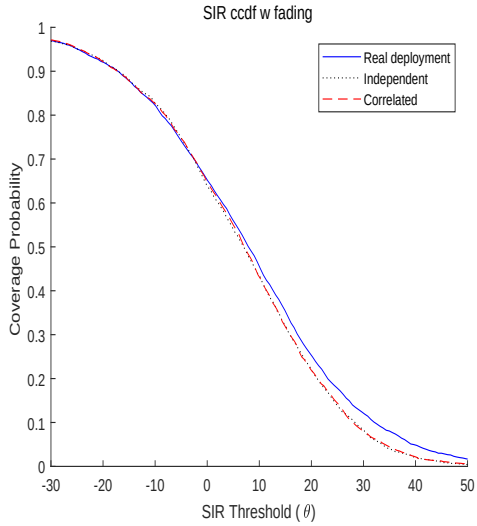

Figure 3.8: $\Delta = 0.1$

ing field when $\Delta = 1$ and 0.1. For both figures, I assume $d = 0.5$, $\lambda_b = 0.5$, $\lambda_{BS} = 1$ and $K = 0.1$. Again, $f_{T_{ij}}(\cdot) = K^{r_{ij}}$ where r_{ij} is a Poisson random variable with mean $\lambda_b \Delta \sqrt{i^2 + j^2}$ which is the implicit number of blockages between the origin and the center of r_{ij}.

When $\Delta = 1$, since the shadowing cell model is a two stage model (designing R_{ij} and assigning $f_{T_{ij}}(\cdot)$), coverage probabilities under the correlated and independent shadowing models exceed that under the real deployment scenario unlike the previous independent shadowing approximation. This comes from the fact that 1) the shadowing cell is too big, so sampling the number of obstacles at the center point of each cell cannot reflect the real situation and 2) $f_{T_{ij}}(\cdot)$ should be correlated to capture real networks as Dr. de Veciana mentioned. However, at least for some effective region such as $\theta > 0dB$, we

can see that the coverage probability under the independent shadowing model is evaluated pessimistically compared to both the correlated blockage model and the real deployment scenario.

When $\Delta = 0.1$, the discrepancy between the two shadowing fields is very small since the two shadowing models converge to the independent shadowing model as I explained in my defense. Under these two models, the coverage probability is evaluated in a pessimistic way, but the correlated case is slightly closer to the real deployment scenario.

My contribution is to provide mathematical rationale for why the independent approximation provides pessimistic performance metrics. It is hard to quantify the exact performance metrics under the correlated shadowing field. Further, my model has certain amount of independence (shadowing over cells), so it is hard to obtain the exact values. At least, my model provides answers on the comparison of the previous independent approximation and the correlated model closer to real network environments.

3.6.2.2 Shannon Throughput

The results for Shannon throughput under the models of Sec. 3.6.1.1 and 3.6.1.2 are summarized in Table. I. The network setting is the same as that of Fig. 3.4 and Fig. 3.5. For both models, the mean Shannon throughput under the correlated shadowing is larger than that under the independent approximation as shown in Theorem. 7. As for the coverage probability, as Δ and λ_d decrease, the Shannon throughput of the correlated case converges to

PPP			PCP		
Δ	cor	ind	$\lambda_m\lambda_d = 1$	cor	ind
1	1.9370	1.8942	$\lambda_d = 1$	2.0180	1.9075
5	2.7300	1.6358	$\lambda_d = 5$	3.5615	2.9402
15	2.7737	1.6101	$\lambda_d = 10$	5.2018	4.1043

Table 3.1: Shannon Throughput

that of the independent approximation. Under the model in Sec. 3.6.1.1, the mean Shannon rate of the correlated case compared to that of the independent approximation is from 2% to 72% better as Δ increases from 1 to 15, and under the model in Sec. 3.6.1.2, the benefits of the correlated case over the independent approximation ranges from 6% to 27% as λ_d increases from 1 to 10.

3.6.2.3 Local Delay

Fig. 3.9 and Fig. 3.10 illustrate the local delays under the models introduced in Sec. 3.4.1 and Sec. 3.4.2. In both figures, the x-axis is in dB scale for a better visualization, and the y-axis is the probability that the local delay is larger than x. For example, in Fig. 3.9, when $\Delta = 5$ under the independent case, the probability that the local delay is larger than 1 is 0.45. From this interpretation, it is possible to see that the local delay under the correlated case is less than that under the independent approximation. The probabilities that the local delay is larger than 1 under the correlated case are from 3.3% to 11.7% below those under the independent approximation when $\Delta = 1, 15$ in Fig. 3.9 and from 1.7% to 7.6% when $\lambda_d = 1, 10$ in Fig. 3.10.

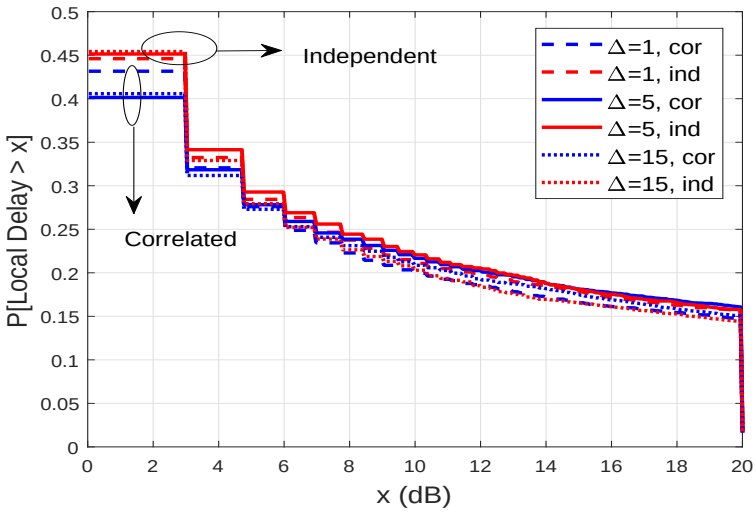

Figure 3.9: Local delay under the model in Sec. 3.4.1.

For both figures, it is possible to see that the probabilities that the local delay exceeds 100 are nonzero. It is considered that if a network with a given topology cannot succeed in transmitting a packet in 100 time slots, it is possible to transmit packets in that topology.

3.7 Conclusions

In this chapter, the impact of correlated shadowing fields is analyzed using stochastic geometry and stochastic ordering. It is shown that the Laplace transform of the interference experienced by the typical user is always larger than under the independent approximation. From this Laplace stochastic ordering, further ordering results on network performance are derived. The main result is that when ignoring the spatial correlations of shadowing, widely

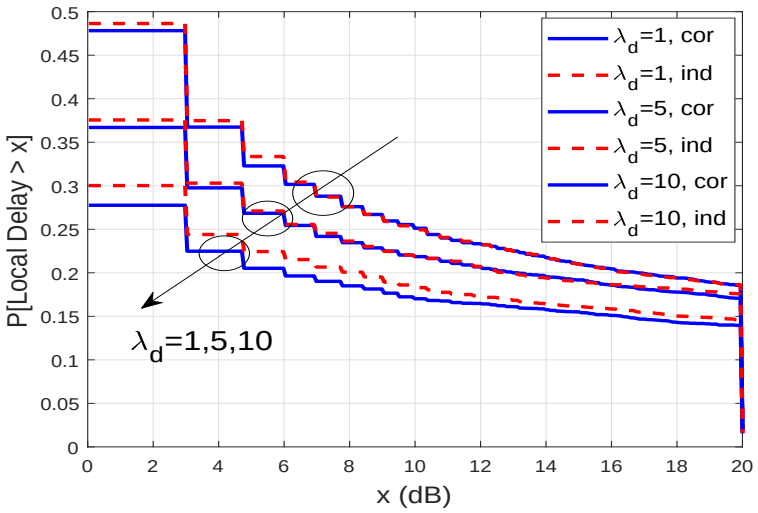

Figure 3.10: Local delay under the model in Sec. 3.4.2.

used metrics such as coverage probability, Shannon throughput, local delay are systematically evaluated in a pessimistic way. For better understanding this physical phenomenon, this chapter has provided two network examples by deriving the exact Laplace transform of the interference distribution under the correlated and independent assumptions. By using the fact that the three key metrics are completely monotone functions, this chapter could also prove ordering results on these metrics under the two shadowing settings.

3.8 Appendix

3.8.1 Probability Generating Functional of a Poisson Point Process

A classical lemma is given for the a probability generating functional (PGFL) [30] of a Poisson point process (PPP).

Lemma 4. Let Φ be a homogeneous PPP with intensity λ on $\mathbb{R}^2$ and $f(\cdot) : \mathbb{R}^2 \to [0,1]$. Then,

$$\mathbb{E}\left[\prod_{X_i \in \Phi} f(X_i)\right] = \exp\left(-\lambda \int_{\mathbb{R}^2} (1 - f(x))dx\right). \tag{3.35}$$

In Equation (3.35), X_i denotes both point X_i and its coordinate.

For the proofs in the next chapter, the definition of an *independent marking* of a point process [5] and a lemma are used.

Definition 3 (Independently marked point process)**.** A marked point process is said to be independently marked if, given the location of the points, the marks are mutually independent random vectors, and if the conditional distribution of mark M_i of a point $x_i \in \Phi$ depends only on the location of x_i it is attached to; i.e., $\mathbb{P}[M_i \in A|\Phi] = \mathbb{P}[M_i \in A|x_i] = F_{x_i}(dM)$ for some probability kernel function.

Lemma 5. For an independently marked homogeneous PPP with density λ on $\mathbb{R}^2$ and marks with distribution $F_x(dm)$ on $\mathbb{R}^l$, its Laplace transform is

$$\begin{aligned}\mathcal{L}_\Phi(f) &= \mathbb{E}[e^{-\sum_i \bar{f}(x_i, M_i)}] \\ &= \exp\left[-\lambda \int_{\mathbb{R}^2} \left(1 - \int_{\mathbb{R}^l} e^{-\bar{f}(x,M)} F_x(dM)\right)\right], \end{aligned} \tag{3.36}$$

for all functions $\bar{f} : \mathbb{R}^{2+l} \to \mathbb{R}^+$.

From Lemma 4 and 5, it is possible to obtain the Laplace transform of the interference fields of Poisson networks. There are several types of Poisson networks modeling both cellular and ad-hoc networks. Two types of networks

are mainly considered where Φ is modeled by 1) a homogeneous PPP or 2) a Poisson cluster process (PCP). These are widely used point processes to model communication networks. The interference measured at the origin under the homogeneous PPP model with the independent and the correlated shadowing is denoted by $I_{ind,p}(o)$ and $I_{cor,p}(o)$, respectively, and by $I_{ind,c}(o)$ and $I_{cor,c}(o)$ under the homogeneous PCP model. respectively.

3.8.2 Proof of Theorem 2

When Φ is a homogeneous PPP with intensity λ, the conditional Laplace transform of $I_{ind,p}(o)$ given $\{R_i\}$ is

$$\begin{aligned}\mathcal{L}_{I_{ind,p}(o)|\{R_i\}}(s) &= \mathbb{E}[e^{-sI_{ind,p}(o)}|\{R_i\}] \\ &= \mathbb{E}[e^{-s\sum_{x\in\Phi} h_x S_x d_x^{-\alpha}}|\{R_i\}] \\ &= \mathbb{E}[e^{-s\sum_i \sum_{x\in\Phi\cap R_i} h_x T_i d_x^{-\alpha}}|\{R_i\}].\end{aligned}$$

By deconditioning $h_x \sim \exp(1)$ and using Lemma 5, the conditional Laplace transform of $I_{ind,p}(o)$ given $\{R_i\}$ becomes

$$\begin{aligned}&\mathcal{L}_{I_{ind,p}(o)|\{R_i\}}(s) \\ &= \exp\left(-\lambda \sum_i \int_{R_i} \left(1 - \mathbb{E}_{T_i,h_x}\left[e^{-sh_x\|x\|^{-\alpha}T_i}\right]\right) dx\right) \\ &= \exp\left(-\lambda \sum_i \int_{R_i} \left(1 - \mathbb{E}_{T_i}\left[\frac{1}{1+s\|x\|^{-\alpha}T_i}\right]\right) dx\right) \\ &= \prod_i \exp\left(-\lambda \int_{R_i} \left(1 - \mathbb{E}_{T_i}\left[\frac{1}{1+s\|x\|^{-\alpha}T_i}\right]\right) dx\right). \qquad (3.37)\end{aligned}$$

In the same manner, it is possible to obtain the Laplace transform of $I_{cor,p}(o)$ as

$$\begin{aligned}
&\mathcal{L}_{I_{cor,p}(o)|\{R_i\}}(s) \\
&= \prod_i \mathbb{E}_{T_i}\left[e^{-s\sum_{x\in\Phi\cap R_i} h_x T_i d_x^{-\alpha}} | \{R_i\}\right] \\
&= \prod_i \mathbb{E}_{T_i}\left[\exp\left(-\lambda \int_{R_i} (1-\mathbb{E}_{h_x}[e^{-sh_x\|x\|^{-\alpha}T_i}])dx\right) | \{R_i\}\right] \\
&= \prod_i \mathbb{E}_{T_i}\left[\exp\left(-\lambda \int_{R_i} (1-\frac{1}{1+s\|x\|^{-\alpha}T_i})dx\right)\right]. \qquad (3.38)
\end{aligned}$$

The main difference between (3.37) and (3.38) is the location of the expectation, $\mathbb{E}_{T_i}$.

3.8.3 Proof of Theorem 4

For a given mother point, its daughter points and their common shadowing random variable (for the correlated case) or their i.i.d. shadowing random variables are independent mark of the mother point. So, by applying Lemma 5, it is possible to obtain the Laplace transform of interference.

Let Φ be the Matérn cluster process with a Matérn radius R_d, the intensity of mother Poisson point process λ_m, and the mean number of daughter points per mother λ_d. The generating functional of Matérn process is also given by [48, 56]

$$\begin{aligned}
&\mathbb{E}[\prod_{x\in\Phi} g(x)] \\
&= \exp\left(-\lambda_m \int_{\mathbb{R}^2} \left[1 - M\left(\int_{\mathbb{R}^2} g(x+y)f(y)dy\right)\right] dx\right), \qquad (3.39)
\end{aligned}$$

where $M(z) = \exp(-\lambda_d(1-z))$ and $f(\cdot)$ is in (3.21).

Under the independent shadowing field, the Laplace transform of $I_{ind,c}(o)$ is

$$\begin{aligned}
\mathcal{L}_{I_{ind,c}(o)}(s) &= \mathbb{E}[e^{-sI_{ind,c}(o)}] = \mathbb{E}[\prod_{x\in\Phi} e^{-sh_x S_x \|x\|^{-\alpha}}] \\
&\overset{(a)}{=} \exp\Bigg(-\lambda_m \int_{\mathbb{R}^2} \Bigg[1 - M\Big(\\
&\qquad \mathbb{E}_{h_x,T_y}[\int_{\mathbb{R}^2} h_x T_y \|x+y\|^{-\alpha} f(y)dy] \Big) \Bigg] dx \Bigg) \\
&\overset{(b)}{=} \exp\Bigg(-\lambda_m \int_{\mathbb{R}^2} \Big[1 - \exp\Big(-\lambda_d \int_{\mathbb{R}^2} \\
&\quad \left(1 - \mathbb{E}_{T_y}\left[\frac{1}{1+s(|x+y|)^{-\alpha} T_y} \right] \right) f(x)dx \Big) \Big] dy \Bigg).
\end{aligned} \tag{3.40}$$

where (a) comes from Lemma 5 and (3.39), and (b) is by deconditioning the channel fading coefficient h_x and the shadowing random variable T_y. In the same manner, the Laplace transform of $I_{cor,c}(o)$ is obtained as

$$\begin{aligned}
&\mathcal{L}_{I_{cor,c}(o)}(s) \\
&= \exp\Bigg(-\lambda_m \int_{\mathbb{R}^2} \Big[1 - \mathbb{E}_{T_y}[\exp\Big(-\lambda_d \\
&\qquad \int_{\mathbb{R}^2} \left(1 - \frac{1}{1+s(|x+y|)^{-\alpha} T_y} \right) f(x)dx \Big)] \Big] dy \Bigg).
\end{aligned} \tag{3.41}$$

As in Theorem 2, the main difference is the location of the expectation of T_y induced by common and independent random variables.

Chapter 4

Multihop Connectivity of Millimeter-Wave Networks

4.1 Introduction

Millimeter wave (mmWave) is the band of spectrum from 30 to 300GHz, where wavelengths are from 1 to 10mm [57]. The main applications in this band so far were radio astronomy, remote sensing, and radar. However, it is currently being seriously considered for 5G wireless communication systems [58], since the spectrum in the sub 3GHz bands is saturated and not sufficient to meet the expected increase in wireless data traffic. Further, the mmWave band is still rather underutilized and a huge bandwidth is available. Even though the mmWave band has a great potential for the future 5G network, there are many critical issues to overcome for commercial applications. For example, the fact that mmWave signals cannot penetrate certain blockages due to physical properties makes coverage one of the main challenges.

In multihop wireless networks, one or more nodes along a path receive and forward data packets over wireless links. Compared to single hop networks, there are several benefits. First of all, multihop wireless networks can extend coverage and improve connectivity [59, 60]. So, multihop relaying is

essential in future mmWave communications. Also, transmitting over several short links might use smaller transmit power than over a single long link. This is particularly important since transmit power is one of main issues in mmWave bands due to severe path loss and wide-band utilization. Further, multihop communications enable higher data rates and efficient use of the wireless medium. In addition, several paths are available which increases the robustness of the network.

In this contribution, I propose a stochastic geometric approach to analyze mmWave multihop networks in the presence of blockages. The modeling of blockage is critical for analyzing connectivity of mmWave networks. To do so, I use a random Boolean model [5] for representing spatially distributed blockages. More precisely, the centers of the blockages are modeled by a homogeneous Poisson point process (PPP) and the shapes of blockages are assumed to be random.

I consider two blockage models: *independent blockage model* and *correlated blockage model*. The *independent blockage* model is considered in order to get exact analytical expressions of connectivity results. In this model, the blockage process is independent over links as in [4] even though two links are close to each other. Then, I consider the *correlated blockage* model which is induced by common blockages, and closer to real environments. I provide exact expressions of connectivity results under the *independent blockage* setting and compare some of these results between two blockage models since it is hard to obtain exact expressions under the correlated blockage model. To the

best of our knowledge, this comparison has not been discussed in the mmWave multihop setting.

Further, I consider both ad-hoc and cellular networks. In ad-hoc network model, there is only a single point process for representing users while there are two independent point processes for modeling users and base stations in cellular network model. I mainly consider the distributions of users connected to a typical user, a typical base station or any base stations. The derived results shed light on the system capacity and cell planning in the mmWave networks.

4.1.1 Related Works

4.1.1.1 Stochastic Geometry and Millimeter Wave Networks

In order to evaluate the performance of wireless networks, system level simulation is crucial. However, a major limitation of simulations is that each wireless scenario should be simulated separately when different system parameters are used. As networks become complicated, system level simulation consumes much time and becomes expensive. As an alternative to system level simulation, stochastic geometry is now recognized as a tractable analytical tool for deriving key performance metrics of networks by utilizing spatial point process to model the location of users and base stations. With this point process theory, it became possible to analyze the performance of cellular networks [12, 29, 45, 61] and ad-hoc networks [41–43] for legacy microwave networks.

However, these mathematical frameworks cannot directly be applied to mmWave networks since the path loss models are quite different. Especially at mmWave frequencies, Line-of-Sight (LOS) signals and Non Line-of-Sight (NLOS) signals have very different distributions. In particular, a link subject to blockages may be too weak to be established. Stochastic geometry has already been used for system level performance of cellular networks [13, 62, 63] and ad-hoc networks [64] under mmWave assumptions. In this literature, blockages are modeled by Boolean models [4]. However, the analysis in these works is restricted to a single hop transmission.

4.1.1.2 Multihop Communication and Connectivity

Multihop communication [33] is a basic technique to improve the performance of wireless networks. It is used to extend coverage and improve connection quality such as robustness with several available paths. Also, as already mentioned, transmission over multiple short links requires less transmit power and energy. These are essential in mmWave communications since mmWave has several issues due to severe path loss.

Multihop communication networks have been analyzed under the stochastic geometric approaches. The optimum transmission range maximizing throughput in multihop packet radio networks was analyzed in [65, 66]. In [67], the authors computed bounds on the end-to-end delay, the optimum hop lengths in TDMA, and ALOHA multihop networks. Also, ALOHA type access control mechanisms for mobile multihop wireless networks were analyzed in [42, 68].

The optimization problem for the product of the successful transmission per unit space by the average range of the transmission was also considered. Further, the gain of opportunistic routing schemes compared to classical routing schemes was analyzed in [69].

However, there are not many attempts to analyze mmWave multihop communications in the spatial network modeling context. [70] provides the connection probability between two points with given Euclidean distance, but it only considers one hop paths and no multiple users or base stations. To the best of our knowledge, this paper is the first to provide general multihop connectivity results for both ad-hoc and cellular networks in the mmWave context.

4.1.1.3 Correlated Shadowing (Blockage)

Even though shadowing fields are spatially correlated [33], only few tractable models have been proposed to represent this correlation. In [35], Gudmundson proposed the first model of correlation between a fixed base station and a moving user by using an autogressive process with an exponential decaying autocorrelation. The correlation effect was also considered in the multiple base station setting [37] and for multihop networks [38]. The 3GPP [39] and IEEE 802.11 standardization groups [40] also suggest models for correlated shadowing based on similar ideas. However, these models give limited intuition on large and dense wireless networks. Also, complex simulation tools are required.

Over the past decades, the shadowing field was incorporated into basic planar PPP models, but the field was assumed independent over wireless links since this approximation leads to simple analytical expressions [2–4]. A first approach to combine correlated shadowing and stochastic geometry was proposed in [46, 47] for urban networks and in [16] for in-building networks. These models analyzed the correlation effect in the special case of blockages represented by Poisson line processes. They are however restricted to blockage based path loss functions and do not allow one to use a distance based term in the path loss function. In [31], a new stochastic geometric model for capturing the spatial correlations was suggested, and the effect of correlation on wireless performance metrics was discovered under single hop communications.

4.1.2 Main Contributions

In this paper, I propose a new mathematical framework for analyzing connectivity of mmWave multihop communications, and more generally in all situations where obstructing by blockages is critical. Under the stochastic geometric framework, the distributions of users connected to the typical user, the typical base station or any base stations are investigated.

I consider the independent and correlated blockage models. Under the independent blockage model, the blockage process is generated per link. So, the blockage process is independent over links. The independent blockage model can be analyzed in terms of the *random connection model* [71] in which the blockage probability of a link is a function of its length. Using well known

results on this *random connection model*, it is possible to obtain exact expressions on network connectivity. However, it is hard to provide exact forms of metrics under the correlated blockage model. The main new results on the matter are comparing results between the independent and correlated blockage models.

I summarize our contributions as follows.

- I first consider the independent blockage model, which is an approximation of real networks allowing one to derive closed form analytical expressions. Under this model, the connectivity results of multihop ad-hoc networks are analyzed by leveraging classical results of the *random connection model* [71]. I *randomly choose* a user and refer to this user as the typical user. It is shown that users connected to the typical user in one hop form an inhomogeneous PPP. From this result, I obtain 1) the mean number of users connected to the typical user in a single hop and 2) the distribution of the distance between the typical user and its nearest connected user. Further, by leveraging classical results on the random connection model, I provide the mean number of k-hop paths starting from (or ending to) the typical user. Finally, I will discuss the critical user density for the existence of an infinite cluster of connected users by using percolation theory [72].

- Under the independent blockage model, I also analyze the multihop cellular networks [73]. Similar to the definition of the typical user, I *randomly*

choose a base station and refer to this base station as the typical base station. I first compute the distribution of base stations connected to the typical user in one hop and that of users connected to the typical base station in one hop. Then, I provide exact expressions of the distributions of users which are connected to any base stations in exactly one hop and two hops, which have not been discussed in previous studies. Also, I derive the distribution of isolated users, neither connected to any base stations nor to any other users. Finally, I also consider a multihoming scenario for a user in an infinite cluster of connected users.

- I also consider the connectivity results of the correlated blockage model. I show that the mean numbers of users connected to the typical user, the typical base station or any base stations in one hop are the same under two blockage models. I also discuss the existence of an infinite size cluster of connected users under the correlated blockage model. Unlike the independent blockage model, there exists no critical user density under some blockage conditions. As in the independent blockage model, a multihoming scenario for a user in a cluster of infinitely many connected users is considered if such cluster exists.

4.2 System Models

4.2.1 Network Model: Ad-hoc Networks and Cellular Networks

In this contribution, I consider two network architectures: ad-hoc networks and cellular networks. In ad-hoc networks, there is only one network

element type, namely mobile users, while in cellular networks, there are two types of network elements, mobile users and base stations. All network elements may act as a source, a relay, and a destination. As in most previous papers on the modeling of wireless networks using stochastic geometry, such network entities are modeled as independent homogeneous PPPs [5]. I also assume that mobile users and base stations form independent homogeneous PPPs in the 2-dimensional Euclidean space ($\mathbb{R}^2$) with positive and finite intensities λ_u and λ_{BS}, respectively. Let Φ_u and Φ_{BS} denote the locations of the mobile users and the base stations.

In order to represent blockages, I consider a Boolean model [5]. Let Ψ_b be the set of blockages; each element $s \in \Psi_b$ represents an blockage. Let Φ_b be the center points of Ψ_b, which forms a homogeneous PPP with intensity λ_b. Each blockage has a random shape. In this paper, I mainly consider two examples which are 1) line segments with isotropic orientation and length l_b and 2) balls with radius r_b.

4.2.2 Connectivity in Millimeter Wave Networks with Multi-Hop Communications

4.2.2.1 Line-of-Sight (LOS)

In this paper, I assume that NLOS mmWave signals are too weak to reach receivers, and LOS is needed for a link connection. Although it has been shown that high data rate can be supported by NLOS links through reflected paths in mmWave networks [74], there still could be a considerable performance degradation compared to LOS links. It becomes more crucial

to maintain a LOS link for users requiring very high data rate to support the 5G immersive experiences [75]. In this paper, I mainly consider the LOS connectivity of mmWave networks and will remain the NLOS connectivity for future works.

4.2.2.2 Signal-to-Noise Ratio

Due to the directivity of mmWave signals, signal-to-noise (SNR) ratio might be more appropriate than signal-to-interference-plus-noise ratio (SINR) in order to measure the quality of wireless connections. Instead of using SNR threshold for a link connection, I equivalently consider a communication range from transmitters. For a link connection, the link distance should be less than R.[1] I assume transmit powers from all users are the same.

The validity of this SNR-based model under mmWave systems is presented by [59, 76–78] which showed that thermal noise dominated interference. The simulation studies in [59] showed the noise-limited nature of these networks and [63] provided similar obsevation in analytical approaches.

4.2.2.3 Multihop Communications

I assume that a link is connected if a) that link is LOS and b) the length of that link is less than R. In the ad-hoc network model, I mainly consider the

[1] In cellular networks, the transmit power of base stations is usually much larger than that of mobile users. However, a cell size is determined by the uplink RF coverage for link connection. So, R can be understood as the maximum reachable range from a mobile user.

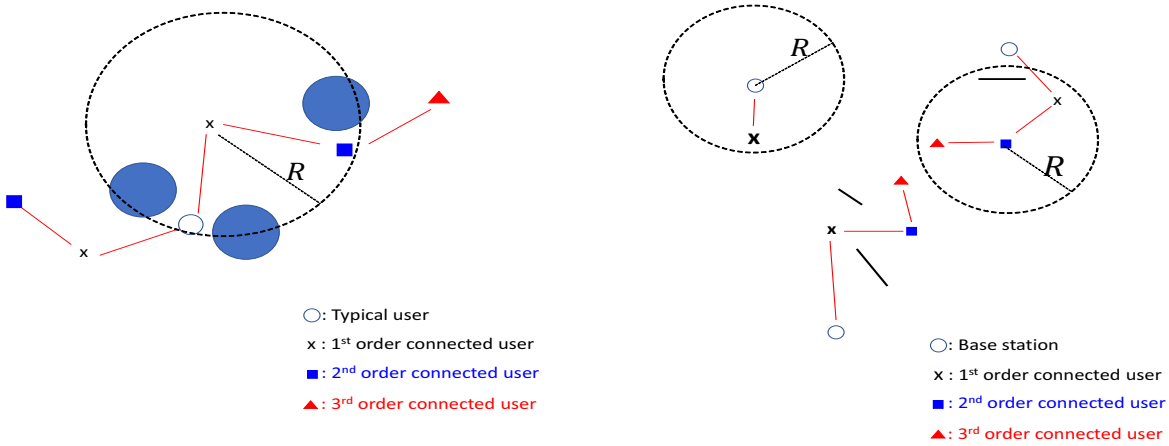

(a) Ad-hoc network model with ball blockages.

(b) Cellular network model with line segment blockages.

Figure 4.1: Network model

distributions of users connected to the typical user located at the origin[2]. A point in Φ_u is defined as a k-th order connected user (to the typical user) if it can reach the origin in k-hops and not in less. Similarly, in cellular networks, I define k-th order connected users as users in Φ_u which are connected to any base stations in k-hops and not in less. See Figure 4.1.

4.2.3 Correlated and Independent Blockage Models

I analyze networks under the correlated and independent blockage models. Under the independent blockage model, each link is independently blocked with a probability function which only depends on its length. This is an ex-

[2]By Slivnyak's theorem [5], it is possible to add the typical user at the origin.

ample of independent shadowing approximations which ignore blockage correlations.

I define a LOS probability function, $L(a,b)$, which is the probability that the link connecting a and b is LOS under the independent blockage model. Depending on the shape of blockages, there are different $L(a,b)$ functions.

Example 4. When the blockages are line segments with isotropic orientation and length l_b, the probability that a given link between a and b is LOS is $L(a,b) = \exp\left(-\mu_1\|a-b\|\right)$, where $\mu_1 = \frac{2\lambda_b l_b}{\pi}$. Also, when the blockages are balls with radius r_b, $L(a,b) = \exp(-\lambda_b r_b^2\pi)\exp\left(-\mu_2\|a-b\|\right)$, where $\mu_2 = 2r_b\lambda_b$.

Proof. The probability function $L(a,b)$ with line segment blockages is derived in [4]. For ball blockages, let us consider a link connecting O and A with length x as in Figure 4.2. With ball blockages, this link is LOS if and only if there exists no point of Φ_b in the shadowed region of Figure 4.2. Since Φ_b is a homogeneous PPP with intensity λ_b and the width of the shadowed region is $2r_b x + r_b^2\pi$, the probability that the link is LOS is $\exp(-\lambda_b \times (2r_b x + r_b^2\pi))$. □

I will use a connectivity probability function $C(a,b) = L(a,b)\mathbb{1}_{\|a-b\|<R}$ for the independent blockage model. Here, $\mathbb{1}_{\text{argument}}$ is the indicator function which takes value 1 if the argument is true and 0 otherwise. With this function, I will analyze the connectivity of networks under the independent shadowing model.

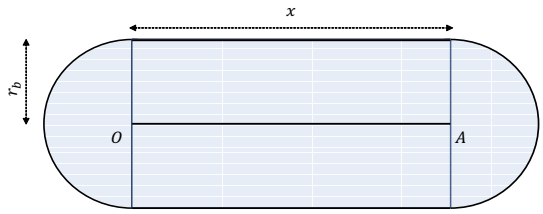

Figure 4.2: Link OA is LOS if and only if no points of Φ_b lies on the shadowed region under the independent shadowing field with ball blockages.

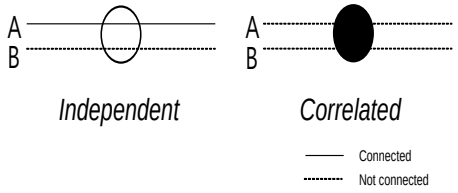

Figure 4.3: Comparison of shadowing models. Under the independent shadowing model, even though two links, A and B are very close, it is possible that one of them is only connected and the other is not.

This independent blockage model is a good approximation if the size of blockages is small or the density of blockages are low, since correlations induced by common blockages are reduced. However, this independent blockage model cannot capture the spatial correlations of networks. Figure 4.3 shows a comparison between the correlated and independent blockage models. Let us assume that two line segments A and B are very close to each other with the same length. Assume that one of them is blocked by blockages with probability p. Then, the probability that both links are blocked is p^2 under the independent blockage model while is almost p under the correlated blockage model. So, the independent blockage model may provide limited intuitions on real networks even though it is possible to obtain simple expressions of important wireless performance metrics.

4.3 Independent Blockage Model

I first consider the independent blockage model. As explained above, a link between $a, b \in \mathbb{R}^2$ is connected with a probability $C(a, b)$ which only depends on the link distance, $\|a - b\|$. So, the model used in this section is an instance of the *random connection model* [72].

4.3.1 Ad-Hoc Networks

A first interesting question is how many users are connected to the typical user in one hop or in multiple hops. To analyze this, I use Palm calculus [5] and focus on the typical user which is located at the origin (o) of $\mathbb{R}^2$. The distribution of users connected to the typical user provides insights on the connectivity properties of the whole ad-hoc network.

4.3.1.1 First Order Connected Users Process

The next lemma provides the distribution of the first order connected users to the typical user.

Lemma 6 (Connected user process)**.** The first order connected users to the typical user form an inhomogeneous PPP with intensity measure

$$\Lambda_a(B) = \int_B \lambda_u C(x, o) dx, \quad B \in \mathcal{B}(\mathbb{R}^2).$$

Proof. This theorem can be proven by the independent thinning of PPPs [5]. The retention function of the independent thinning is $p_a(x) = C(x, o)$ for $x \in \mathbb{R}^2$. Since Φ_u is a homogeneous PPP with intensity measure $\lambda_u dx$, I can

obtain the intensity measure of the first order connected users as

$$\Lambda_a(B) = \int_B p_a(x)\lambda_u dx = \int_B \lambda_u C(x,o)dx, \quad B \in \mathcal{B}(\mathbb{R}^2).$$

□

Since the first order connected users forms a PPP, the number of users connected to the typical user in one hop is a Poisson random variable with a mean $\Lambda_a(\mathbb{R}^2)$.

Corollary 9. The mean number of first order connected users to the typical user is $\Lambda_a(\mathbb{R}^2)$, and the probability that there are no connected users to the typical user is $\exp(-\Lambda_a(\mathbb{R}^2))$.

Before I give an example, I define a function to be used in the remaining of this paper:

$$m(a,b,c) = \frac{2\pi a}{b^2}\left(1 - \frac{1+bc}{\exp(bc)}\right),$$

and especially, when $c = \infty$,

$$m(a,b,\infty) = \frac{2\pi a}{b^2},$$

since $\exp(bc) = 1 + bc + c^2\sum_{i=2}^{\infty}\frac{b^i c^{i-2}}{i!}$.

Example 5. When the blockages are line segments with isotropic orientation and length l_b, the mean number of first order connected users to the typical user is $m(\lambda_u, \mu_1, R)$ and the probability that no user is connected to the

typical user is $\exp(-m(\lambda_u, \mu_1, R))$. When the blockages are balls with radius r_b, the mean number of first order connected users to the typical user is $m(\lambda_u \exp(-\lambda_b r_b^2 \pi), \mu_2, R)$ and the probability that there is no connected user is $\exp(-m(\lambda_u \exp(-\lambda_b r_b^2 \pi), \mu_2, R))$.

I can obtain the statistics of LOS users to the typical user by plugging in $R = \infty$ since when $R = \infty$, $C(x, o) = L(x, o)\mathbb{1}_{\|x-o\|<\infty} = L(x, o)$.

Corollary 10. The LOS users from the typical user's view form an inhomogeneous PPP with intensity measure

$$\Lambda_{\mathrm{LOS},a}(B) = \int_B \lambda_u L(x, o) dx, \quad B \in \mathcal{B}(\mathbb{R}^2).$$

Also, the mean number of LOS users from the typical user's perspective is $\Lambda_{\mathrm{LOS},a}(\mathbb{R}^2)$, and the probability that there exists no LOS user to the typical user is $\exp(-\Lambda_{\mathrm{LOS},a}(\mathbb{R}^2))$.

Example 6. When the blockages are line segments with isotropic orientation and length l_b, the mean number of LOS users with respect to the typical user is $m(\lambda_u, \mu_1, \infty) = \frac{2\pi\lambda_u}{\mu_1^2}$ and the probability that there is no LOS user to the typical user is $\exp(-m(\lambda_u, \mu_1, \infty)) = \exp\left(-\frac{2\pi\lambda_u}{\mu_1^2}\right)$. When the blockages are balls with radius r_b, the mean number of LOS users with respect to the typical user is $m(\lambda_u \exp(-\lambda_b r_b^2 \pi), \mu_2, \infty) = \frac{2\pi\lambda_u}{\exp(\lambda_b r_b^2 \pi)\mu_2^2}$ and the probability that there is no LOS user to the typical user is $\exp(-m(\lambda_u \exp(-\lambda_b r_b^2 \pi), \mu_2, \infty)) = \exp\left(-\frac{2\pi\lambda_u}{\exp(\lambda_b r_b^2 \pi)\mu_2^2}\right)$.

The next interesting property is the distribution of the distance between the typical user and its nearest connected user.

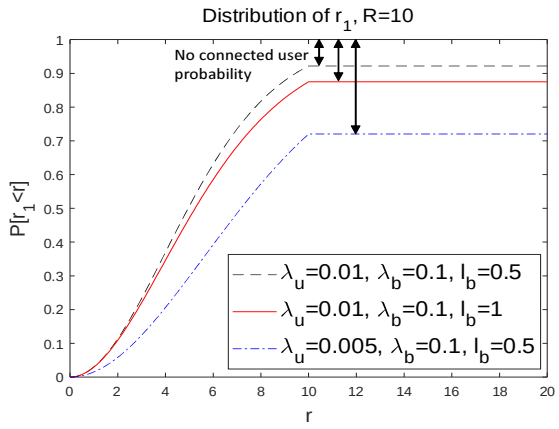

Figure 4.4: Distribution of the distance between the typical user and its nearest connected user. In this figure, blockages are line segments with length l_b and uniformly random orientation.

Corollary 11. The distribution of r_1 which is the distance between the typical user and its nearest connected user is

$$\mathbb{P}[r_1 \leq r] = 1 - \exp\left(-\Lambda_a(\mathcal{B}(0, r - (r-R)\mathbb{1}_{r>R}))\right),$$

where $\mathcal{B}(x, d)$ is a ball centered at x and with radius d.

Proof. Since the first order connected users form an inhomogeneous PPP,

$$\mathbb{P}[r_1 > r] = \mathbb{P}[\text{no connected user in } \mathcal{B}(o, r)] = \exp\left(-\Lambda_a(\mathcal{B}(o, r - (r-R)\mathbb{1}_{r>R}))\right). \tag{4.1}$$

□

Some examples of the distribution of r_1 are illustrated in Figure 4.4. For all cases, the cumulative distribution functions do not converge to 1 since the

typical user may not have any connected users under some PPP configurations. Further, as the density of users decreases or the size of blockages increases, the horizontal asymptote, which is the probability of the existence of at least one connected user, also decreases.

***Remark* 14.** Corollary 11 is related to the result in Corollary 9 which provides the probability that no users are connected to the typical user. By plugging in $r = R$ in (4.1), I get

$$\begin{aligned}
\mathbb{P}[r_1 > R] &= \exp\left(-\Lambda_a(\mathcal{B}(o,R))\right) \\
&= \exp\left(-\int_{\mathcal{B}(o,R)} \lambda_u C(x,o)dx\right) \\
&\overset{(a)}{=} \exp\left(-\int_{\mathbb{R}^2} \lambda_u C(x,o)dx\right) \\
&= \exp\left(-\Lambda_a(\mathbb{R}^2)\right),
\end{aligned}$$

which is the probability of no connected users. (a) is by the fact that $C(x,o) = 0$ for $\|x\| > R$. With $r = R = \infty$, (4.1) becomes the probability of no LOS users to the typical user in $\mathbb{R}^2$.

4.3.1.2 Mean number of k-th order multihop paths

A k-th order multihop path is a path with k hops between a k-th order connected user and the typical user. By definition, a k-th order connected user may have more than one k-th order path to the typical user. The following lemma is a classical result for counting k-hop paths in random connection model.

Lemma 7 (k-th order multihop paths)**.** The mean number of k-th order multihop paths starting from the typical user is

$$\lambda_u^k \int_{\mathbb{R}^2} \cdots \int_{\mathbb{R}^2} \left(\prod_{i=0,\ldots,k-1} C(X_{i+1}, X_i) \right) \left(\prod_{i=0,\ldots,k-2}^{i+1<j\leq k} (1 - C(X_j, X_i)) \right) dX_1 dX_2 \ldots dX_k, \tag{4.2}$$

where $X_0 = o$.

Proof. I focus on the case with $k = 2$, and it can be easily extended to $k > 2$. The mean number of the second order multihop paths is

$$\mathbb{E}\left[\sum_{X_i, X_j \in \Phi_u}^{X_i \neq X_j} \mathbb{1}_{X_i \text{ and } o \text{ are connected.}} \mathbb{1}_{X_j \text{ and } o \text{ are not connected.}} \mathbb{1}_{X_i \text{ and } X_j \text{ are connected.}} \right] \tag{4.3}$$

In (4.3), X_j is a second order connected user and X_i is a relay between x_j and the typical user, respectively. (4.3) considers all such X_i, and X_j pairs. So (4.3) is the mean number of 2-hop paths to the typical user. (4.2) with $k = 2$ is obtained by leveraging Campbell's formula for higher order moment measures of PPPs [5].

For general k, (4.2) counts the paths starting from $X_0 = o$, X_1, ... to X_k with the same manner. □

***Remark* 15.** The mean number of the second order multihop paths starting from the typical user, (4.3), is an upper bound on the mean number of second order connected users to the typical user since one second order user may have several second order paths. However, I can obtain tighter upper bound to

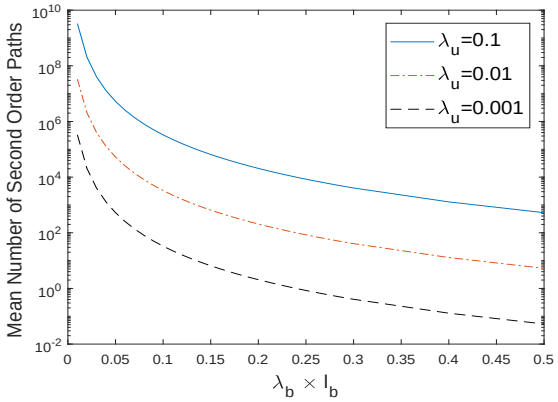

Figure 4.5: Mean numbers of second order multihop paths with line segment blockages when $R = \infty$.

the mean number of second order connected users by removing some of these paths.

$$\mathbb{E}\Bigg[\sum_{X_i,X_j,X_k\in\Phi_u}^{X_i\neq X_j,X_j\neq X_k,X_k\neq X_i} \mathbb{1}_{X_i \text{ and } o \text{ are connected.}}\mathbb{1}_{X_j \text{ and } o \text{ are not connected.}}\mathbb{1}_{X_k \text{ and } o \text{ are connected.}}$$

$$\mathbb{1}_{X_j \text{ and } X_k \text{ are connected.}}\mathbb{1}_{X_j \text{ and } X_k \text{ are connected.}}\mathbb{1}_{\|X_i-X_j\|<\|X_k-X_j\|}\Bigg]$$

$$=\lambda_u^3\left(\int_{\mathbb{R}^2}\int_{\mathbb{R}^2}\int_{y\in\mathbb{R}^2:\{y:\|x-y\|<\|z-y\|\}} C(x,o)[1-C(y,o)]C(z,o)C(x,y)C(y,z)dydxdz\right). \tag{4.4}$$

In (4.4), X_j is the second order user and X_i, X_k are connected to both the typical user and X_j, and I remove a second order multihop path connecting o, X_k and X_j by multiplying by $\mathbb{1}_{\|X_i-X_j\|<\|X_k-X_j\|}$. This expression is still not the exact value but is tighter. However, if the blockage process is very dense or the size of the blockages is large enough, (4.3) and (4.4) converge to the mean

number of second order connected users since the probability that a second order connected user has multiple second order paths will decrease.

4.3.1.3 Percolation

In this part, I focus on a global property of networks related to percolation theory [72]. The most common percolation model is to take a regular lattice and make it into a random network by randomly occupying sites (vertices) or bonds (edges) with an independent probability p. When p is larger than a critical threshold p_o, large clusters and long-range connectivity appears and p_o is called the percolation threshold. Several studies considered percolation problem under networks generated by PPP instead of a regular lattice.

In terms of connectivity, I are interested in multihop paths supporting infinite long distance communication and this question would reduce to a bond-percolation problem [79] under the independent blockage model. Generally, the connectivity funcion $C(\cdot, \cdot)$ is a decreasing function with respect to the length. So, I can expect that there exists an infinite cluster of connected users when the density of users is very high. In this part, I present the existence of a critical density $0 < \lambda_c < \infty$ such that, if $\lambda_u > \lambda_c$, then an infinite connected component of users exists with probability one whereas if $\lambda_u < \lambda_c$, no infinite cluster exists almost surely. This phenomenon is the percolation phase transition [5] of the random connection model [72].

The following theorem is the phase transition of the existence of an infinite cluster of connected users under the random connection model.

Theorem 9 (Percolation for ad-hoc networks)**.** There exists a critical density $\lambda_c^a \in (0, \infty)$ such that

$$\lambda_c^a \geq \frac{1}{\int_{\mathbb{R}^2} C(x, o)dx},$$

where if $\lambda_u > \lambda_c^a$, then the there exists almost surely an infinite cluster of users while if $\lambda_u < \lambda_c^a$, there is almost surely no infinite cluster of connected users.

Proof. See Appendix 4.6.1. □

***Remark* 16.** In Theorem 9, I assume that all users may work as a repeater for delivering other's messages. However, in some case, a user may not be willing to work as a repeater for other users. Let p^a be the probability that each user works as a repeater.[3] There is a critical value $p_c^a = \frac{\lambda_c^a}{\lambda_u}$ such that if $p^a > p_c^a$, then there exists almost surely an infinite cluster of idle users while if $p^a < p_c^a$, there is almost surely no infinite cluster of idle connected users. From the independent thinning of PPPs, users who can work as repeaters form a homogeneous PPP with intensity $p^a\lambda_u$. So by Theorem 9, if $p^a > p_c^a = \frac{\lambda_c^a}{\lambda_u}$, i.e., $p_a\lambda_u > \lambda_c^a$, then there exists an infinite size user cluster with probability 1, while if $p^a < p_c^a$, there exists almost surely no infinite connected component.

4.3.2 Cellular Networks

Now, I consider the multihop cellular network model [73]. I recall that in this model, there are two network entities, base stations and users, which form independent homogeneous PPPs with intensity λ_{BS} and λ_u, respectively.

[3] So Theorem 9 is the case with $p^a = 1$.

In this part, I define a connected user as a user connected to any base stations. Further, a k-th order connected user is a user connected with any base stations in k-hops and not in less.

4.3.2.1 Typical User and Typical Base Station

I start to analyze connectivity of the typical user and typical base station. As in Section 4.3.1.1, distributions of users connected to the typical base station in one hop and base stations connected to the typical user in one hop can be obtained from the next lemma.

Lemma 8. Under the Palm probability of Φ_u, the point process of base stations connected to the typical user in one hop is an inhomogeneous PPP with intensity measure

$$\Lambda_c(B) = \int_B \lambda_{\mathrm{BS}} C(x, o) dx,$$

where $B \in \mathcal{B}(\mathbb{R}^2)$. So, the mean number of connected base stations to the typical user in one hop is $\Lambda_c(\mathbb{R}^2)$ and the probability that no base stations are connected to the typical user in one hop is $\exp(-\Lambda_c(\mathbb{R}^2))$. Similarly, under the Palm probability of Φ_{BS}, users connected to the typical base station in one hop is an inhomogeneous PPP with intensity measure

$$\Lambda_a(B) = \int_B \lambda_u C(x, o) dx,$$

as in Lemma 6. So, the mean number of connected users to the typical base station in one hop is $\Lambda_a(\mathbb{R}^2)$ and the probability that no users are connected to the typical base station in one hop is $\exp(-\Lambda_a(\mathbb{R}^2))$.

Proof. This theorem is a rephrasing of Lemma 6. □

***Remark* 17.** From Lemma 8, it is possible to obtain 1) the mean number of base stations connected to the typical user, 2) the probability that no users are connected to the typical base station, and 3) the distribution of the distance between the typical base station and its nearest connected user as the results in Corollaries 9 and 11.

4.3.2.2 First Order Connected Users Process

From now, I will investigate properties of the user process. In this part, I focus on the first order connected users. Denote the first order connected users by Φ_u^1 and the other users by Φ_u^{1+}. So, $\Phi_u^1 \cup \Phi_u^{1+} = \Phi_u$.

Theorem 10 (Distribution of Φ_u^1 and Φ_u^{1+} conditioned on Φ_{BS})**.** Conditioned on $\Phi_{\mathrm{BS}} = \{X_i\}_{i\in\mathbb{N}}$, Φ_u^1 and Φ_u^{1+} are independent inhomogeneous PPPs. The conditional intensity measures of Φ_u^1 and Φ_u^{1+} given Φ_{BS} are

$$\Lambda^1_{c|\Phi_{\mathrm{BS}}}(B) = \int_B \lambda_u \left(1 - \prod_{X_i\in\Phi_{\mathrm{BS}}} (1 - C(x, X_i))\right) dx, \tag{4.5}$$

and

$$\Lambda^{1+}_{c|\Phi_{\mathrm{BS}}}(B) = \int_B \lambda_u \prod_{X_i\in\Phi_{\mathrm{BS}}} (1 - C(x, X_i)) dx, \tag{4.6}$$

with $B \in \mathcal{B}(R^2)$, respectively.

Proof. Conditioned on $\Phi_{\mathrm{BS}} = \{X_i\}_{i\in\mathbb{N}}$, a user located at x is connected to any base station with probability $1 - \prod_{X_i\in\Phi_{\mathrm{BS}}}(1 - C(x, X_i))$. By the independent

thinning theorem of PPPs, I can obtain the conditional intensity measures of Φ_u^1 and Φ_u^{1+} as (4.5) and (4.6). □

Next, I give the distribution of Φ_u^1 and Φ_u^{1+} after deconditioning with respect to Φ_{BS}.

Theorem 11 (Distribution of Φ_u^1, Φ_u^{1+})**.** Φ_u^1 and Φ_u^{1+} are stationary point processes with intensities

$$\lambda_u^1 = \lambda_u \left(1 - \exp\left(-\Lambda_c(\mathbb{R}^2)\right)\right),$$

and

$$\lambda_u^{1+} = \lambda_u \exp\left(-\Lambda_c(\mathbb{R}^2)\right),$$

respectively.

Proof. First, I will show that Φ_u^1 is a stationary point process. For $A \in \mathcal{B}(\mathbb{R}^2)$,

$$\mathbb{P}[\Phi_u^1(A) = k] = \mathbb{P}[\Phi_u^1(A + t) = k],$$

for any $t \in \mathbb{R}^2$ and $k \in \mathbb{N} \cup \{0\}$, since Φ_u and Φ_{BS} are homogeneous PPPs and the same connectivity function is used for both $\Phi_u^1(A)$ and $\Phi_u^1(A+t)$. Further, under the independent blockage model, the connectivity function only depends on the link distance. So Φ_u^1 is a stationary point process. Similarly, Φ_u^{1+} is a stationary point process.

From Lemma 8, the Palm probability that the typical user is connected to any base stations in one hop is $1 - \exp(-\Lambda_c(\mathbb{R}^2))$. It follows from results

in Palm calculus [80] that the densities of Φ_u^1 and Φ_u^{1+} are the product of the user intensity, λ_u, and the Palm probability that the typical user is connected in one hop or not, respectively. □

***Remark* 18.** Conditioned on Φ_{BS}, Φ_u^1 and Φ_u^{1+} are independent PPPs. However, after deconditioning with respect to Φ_{BS}, Φ_u^1 and Φ_u^{1+} are no more PPPs. Φ_u^1 and Φ_u^{1+} are Cox point processes [48] after deconditioning.

4.3.2.3 Second Order Connected Users Process

Let Φ_u^2 be the second order connected users. Since $\Phi_u^{1+} = \Phi \setminus \Phi_u^1$, I have $\Phi_u^2 \subset \Phi_u^{1+}$.

Theorem 12 (Distribution of Φ_u^2 conditioned on Φ_{BS})**.** Conditioned on $\Phi_{\text{BS}} = \{X_i\}_{i\in\mathbb{N}}$, the intensity measure of Φ_u^2 is

$$\Lambda^2_{u|\Phi_{\text{BS}}}(B) = \lambda_u \int_B \left(1 - \exp(-\int_{\mathbb{R}^2} (1 - C(x,y))dy)\right) \prod_{X_i \in \Phi_{\text{BS}}} (1 - C(x, X_i))dx,$$

where $B \in \mathcal{B}(\mathbb{R}^2)$.

Proof. See Appendix 4.7. □

In next theorem, I give the distribution of Φ_u^2 after deconditioning Φ_{BS}.

Theorem 13 (Distribution of Φ_u^2)**.** Φ_u^2 is a stationary point process and its density is

$$\lambda_2 = \lambda_u \int_{\mathcal{B}} e^{-\lambda_{\text{BS}} \int_{\mathbb{R}^2} C(z,x)dx} dz - \lambda_u \int_{\mathcal{B}} e^{-\lambda_u \int_{\mathbb{R}^2} C(z,y)dy} \Bigg[\sum_{k=0}^{\infty} \frac{\lambda_u^k}{k!} \int_{\mathbb{R}^2} \dots \int_{\mathbb{R}^2} C(z,y_1) \dots C(z,y_k)$$
$$\times\, e^{-\lambda_{\text{BS}} \int_{\mathbb{R}^2} \left(1 - \prod_{j=1}^{k} (1 - C(y_j,x))(1 - C(z,x))\right) dx} dy_1 \dots dy_k \Bigg] dz,$$

where $\mathcal{B}$ is any Borel set with $|\mathcal{B}| = 1$.

Proof. From Theorem 11, Φ_u^1 and Φ_u^{1+} are stationary point processes. Since I use the independent connectivity function over links, I obtain that

$$\mathbb{P}[\Phi_u^2(A) = k] = \mathbb{P}[\Phi_u^2(A + t) = k],$$

for any $t \in \mathbb{R}^2$ and $k \in \mathbb{N} \cup \{0\}$ and this implies that Φ_u^2 is a stationary point process.

For the density of Φ_u^2, see Appendix 4.7.1. □

4.3.2.4 Isolated User

I define a totally isolated user as a user which is not connected to any base station or any other users.

Theorem 14 (Isolated users)**.** The probability that the typical user is totally isolated is

$$\exp\left(-(\Lambda_a(\mathbb{R}^2) + \Lambda_c(\mathbb{R}^2))\right).$$

Proof. As in Lemmas 6 and 8, base stations and users connected in one hop to the origin form an inhomogeneous PPP with intensity measure

$$\int_B (\lambda_u + \lambda_{\mathrm{BS}}) C(x, o) dx = \Lambda_a(B) + \Lambda_c(B),$$

for $B \subset \mathbb{R}^2$, since the superposition of Φ_{BS} and Φ_u is a homogeneous PPP with intensity $\lambda_{\mathrm{BS}} + \lambda_u$. Since the number of users or base stations connected

to the user at the origin is a Poisson random variable, the probability that this user is isolated is $\exp\left(-(\Lambda_a(\mathbb{R}^2)+\Lambda_c(\mathbb{R}^2))\right)$. □

Corollary 12. Denote the isolated user process by Φ_u^{iso}. Then Φ_u^{iso} is a stationary point process and its density is $\lambda_u \exp\left(-(\Lambda_a(\mathbb{R}^2)+\Lambda_c(\mathbb{R}^2))\right)$.

Proof. I will skip the proof of the stationarity but it is similar with the proof of Theorem 11. Since Φ_u^{iso} is a stationary stationary point process, its intensity is $\lambda_u \exp\left(-(\Lambda_a(\mathbb{R}^2)+\Lambda_c(\mathbb{R}^2))\right)$ as in Theorem 11. □

4.3.2.5 Multihoming

This part is motivated by *multihoming* [81]. For enhancing reliability, users try to maintain multiple simultaneous associations with different base stations and this is referred to as *multihoming*. In this part, I assume there exists an infinite cluster of connected users, i.e., λ_u is larger than λ_c^a in Theorem 9. I focus on a user in this infinite size cluster and answer how many base stations are connected to this user using multihop connections. For obvious reason, I only consider multihop paths from this user to base stations with no intermediate base station node. Simply, I might think base stations are end nodes of multihop links starting from the considered user.

Theorem 15 (Multihoming for a user in an infinite user cluster)**.** If $\lambda_u > \lambda_c^a$, there exists a cluster of infinitely many connected users. Then, each user in this infinite cluster are connected to infinitely many base stations.

Proof. To prove this theorem, I will show that infinitely many base stations are connected to the infinite user cluster for any given realized user process.

Denote by $\mathcal{U}$ the set of users in the infinite user cluster. Among $\mathcal{U}$, I can select infinitely many users such that the distance between any pair is larger than $2R$. Denote the set of these users by $\mathcal{U}_s$. Since the communication range is R, a base station cannot be connected in one hop to more than two users in $\mathcal{U}_s$. Since the probability that each user in $\mathcal{U}_s$ is connected to any base station in one hop is positive and the cardinality of $\mathcal{U}_s$ is infinite, there are infinitely many base stations connected to $\mathcal{U}_s$, which means infinitly many base stations can support multihoming service to users in this infinite cluster. □

4.4 Effects of Blockage Correlation

In this section, I revisit the results in Section 4.3 under the correlated blockage setting. As in Section 4.3, blockages are modeled by a Boolean model. In Section 4.3, blockage process is independently generated for each link, but not in this section.

I present three results in this section. First, I will show that the mean numbers of the connected links given any n links are the same under the correlated and independent blockage models. Then, I will investigate percolation under the correlated blockage model. Finally, multihoming result under the correlated blockage model is presented.

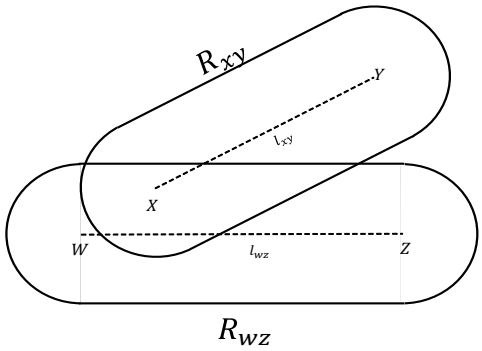

Figure 4.6: Under the independent blockage model with ball blockages, $R_{xy} \cup R_{wz}$ is not considered.

4.4.1 Preliminary

Before I compare the connectivity results between the correlated and independent blockage models, I present the following theorem.

Theorem 16. Given n links, the probability that these n links are either all LOS or all NLOS is less than under the independent blockage model that under the correlated blockage model. Further, the probability that these n links are either all connected or all non connected is less under the independent blockage model than under the correlated one.

Proof. I start from the case $n = 2$. A link connecting a and b is denoted by $\overline{ab}$. I prove when blockages are balls with radius r_b but it can be extended to the case with line segments.

Let us consider $\overline{xy}$ and $\overline{wz}$ with their lengths l_{xy}, l_{wz}, respectively. Also, let R_{xy} and R_{wz} be regions for determining $\overline{xy}$ and $\overline{zw}$ are LOS or NLOS as

in Figure 4.2. If the blockages are balls, then, the areas of R_{xy} and R_{wz} are $r_b^2\pi + 2r_b l_{xy}$, $r_b^2\pi + 2r_b l_{xz}$, respectively. See Figure 4.6.

Under the correlated blockage model, the probability that both links are LOS is

$$\mathbb{P}[\text{no } \Phi_b \text{ in } R_{xy} \cup R_{wz}] = \exp\left(-\lambda_b |R_{xy} \cup R_{wz}|\right) \geq \exp\left(-\lambda_b (|R_{xy}| + |R_{wz}|)\right),$$

which is that under the independent blockage model.

The probability that both links are NLOS under the correlated blockage model is

$$\begin{aligned}
&\mathbb{P}[\text{Both } \overline{xy} \text{ and } \overline{wz} \text{ are NLOS.}] \\
&\overset{(a)}{=} 1 - \exp(-\lambda_b(|R_{xy} \cap R_{wz}|)) \\
&+ \exp(-\lambda_b(|R_{xy} \cap R_{wz}|))(1 - \exp(-\lambda_b(|R_{xy} \cap R_{wz}^c|)))(1 - \exp(-\lambda_b(|R_{xy}^c \cap R_{wz}|))) \\
&= 1 - \exp(-\lambda_b|R_{xy}|) - \exp(-\lambda_b|R_{wz}|) + \exp(-\lambda_b|R_{xy} \cup R_{wz}|) \\
&\geq (1 - \exp(-\lambda_b|R_{xy}|))(1 - \exp(-\lambda_b|R_{wz}|)),
\end{aligned}$$

which is that under the independent blockage model. The first line of (a) means considering the case that at least one center of blockage is in $R_{xy} \cap R_{wz}$ and the second line of (a) is considering the case that no center of blockage is in $R_{xy} \cap R_{wz}$.

The case with general n can be proved by induction. Let us assume that the case with $n = k$ is proved. I will add one new link where k links are deployed. Denote the region for the existing k links is R_k and the region for

the new link is R_{k+1}. In order to prove the case with $n = k + 1$, it is enough to follow the above arguments by plugging R_k into R_{xy} and R_{k+1} into R_{wz}. So the statement is proved for general n by induction.

Since the connectivity condition consists in satisfying both 1) the LOS condition and 2) that the link distance is less than R, the connectivity part can be naturally extended by considering links with a length less than R. □

4.4.2 Connectivity of the Typical User/Base Station

In the next theorem, I show that the mean numbers of connected links for given n links are the same for both blockage models.

Theorem 17 (Blockage model comparison: mean number of the connected links)**.** For given n links ((x_i,y_i), $i = 1, \ldots, n$, $x_i \neq y_i \forall i$), the mean numbers of the connected links are

$$\sum_{i=1,\ldots,n} C(x_i, y_i),$$

under the two blockage models.

Proof. See Appendix 4.7.2. □

Corollary 13. In the ad-hoc network model, the mean numbers of users connected to the typical user are the same under the independent and the correlated blockage models when x_i is the typical user and y_i are the other users. Similarly, in the cellular network model, the mean numbers of users connected to any base stations are the same under two blockage models when x_i are users and y_i are base stations.

***Remark* 19.** In Lemma 6, I show that users connected to the typical user in one hop form an inhomogeneous PPP under the independent blockage model. However, from Theorem 16 and Corollary 13, it is no more PPP under the correlated blockage model since the distributions of the first order connected users are different for both blockage models.

4.4.3 Percolation

The existence of the critical density for percolation, λ_c^a, is investigated under the independent blockage model in Section 4.3. By Theorem 9, under the independent blockage model, when $\lambda_u > \lambda_c^a$, there exists almost surely a cluster of infinitely many connected users for any size and density of blockages. The next theorem results that there is no infinite user cluster under the correlated blockage model when the volume fraction of blockages exceeds a certain value.

In this part, I assume that blockages are balls with a radius r_b. As in [82,83], I consider the *void space* which is a space not occupied by blockages. Especially, the *void percolation* problem is investigated for the existence of infinitely connected void space.

Theorem 18 (Percolation in the Correlated Blockage Model)**.** When there is no infinite connected void space, there is no cluster with infinitely many connected users when the density of users is finite. In other words, there exists no finite critical user density.

Proof. By the connection rule, two network elements are connected only when

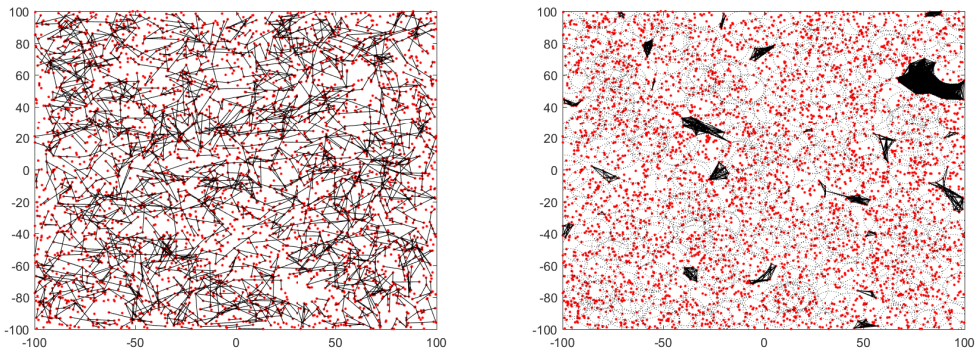

(a) independent, $\lambda_u = 0.1, R = 20, \lambda_b = 0.01, r_b = 9$

(b) correlated, $\lambda_u = 0.1, R = 20, \lambda_b = 0.01, r_b = 9$

Figure 4.7: User percolation model: In above figures, lines are connected links, dotted circles in Figure 4.7b are blockages and points are users.

these are on the same connected void space. Since λ_u is finite, there is no infinite size cluster of connected users on any finite size connected void space.

□

***Remark* 20.** The *void percolation* problem has been investigated numerically in several papers. Especially, when the blockages are spheres with the same radius, there is simulation evidence there exists no infinitely connected void space when the volume fraction of blockages is larger than 0.968 ± 0.004 [82]. Figures 4.7a and 4.7b illustrate this case. In these figures, the same realized point process is used when the volume fraction of blockages is larger than 0.968 ± 0.004. Unlike the independent case (Figure 4.7a), there is no infinite cluster of connected users since each void space is surrounded by blockages in the correlated case (Figure 4.7b).

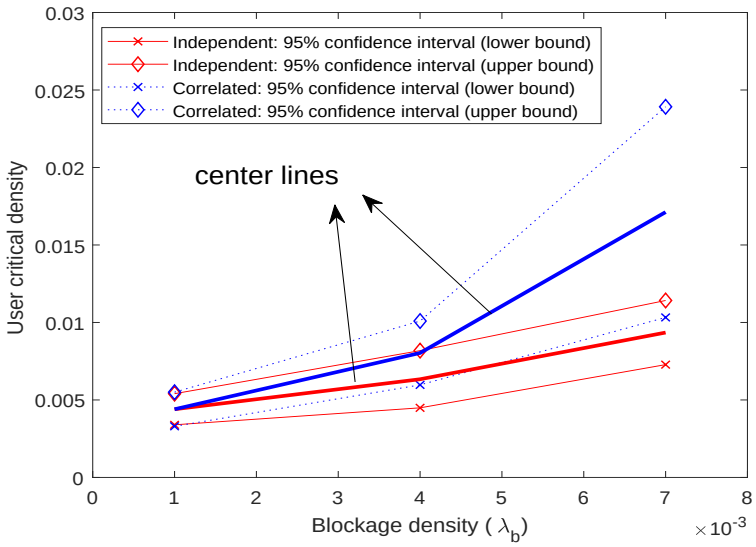

Figure 4.8: User critical density vs blockage density (λ_b)

In the next part, I will present the case when there exists an infinite size connected void space.

Conjecture 1. When there exists an infinite size connected void space with dominant blockage effects, the independent blockage model has more chance to have an infinite size connected users cluster than the correlated blockage model under the same network parameters.

***Remark* 21.** Figure 4.8 illustrates the user critical densitiy λ_u^c with respect to the blockage density, λ_b, under the correlated and independent blockage models. I obtained λ_u^c when the radius of blockages $r_b = 5$, and considered three cases: $\lambda_b = 0.001$ (low blockage effect), 0.004 (intermediate blockage effect), and 0.007 (dominant blockage effect). For the correlated blockage model, I

generated 100 blockage processes and obtained user critical density for each blockage process. Since I consider $[-100, 100] \times [-100, 100]$ networks, I assume that there exists an infinite connected user cluster if there exists at least one multihop path connecting from leftmost to rightmost and at least one multihop path from bottom to top. As it can be shown in Figure 4.8, when the blockage effect is dominant, the user critical density under the independent case is smaller than that under the correlated case. Further, it is harder to check the ordering relation of critical densities between the correlated and independent model when the blockage effect is small. Nevertheless, this simulation result supports the conjecture in my thesis.

In the above methodology, I changed λ_b under fixed r_b for investigating the blockage effects on the user percolation problem. Another way to observe the blockage effects is changing r_b under fixed λ_b. Even though the latter case may provide interesting physical intuition, the former case is more relevant to the real wireless network environments.

4.4.4 Multihoming

I revisit the multihoming scenario. In Theorem 15, I showed that infinitely many base stations are connected to a user in a cluster of infinitely many connected users under the independent blockage model. The following theorem answers the same question but under the correlated one.

Theorem 19 (Multihoming under the correlated blockage model)**.** If there exists a cluster of infinitely many connected users under the correlated blockage

model, infinitely many base stations are connected to a user in this cluster.

Proof. Theorem 15 shows that the number of connected links between a user in an infinite cluster and a base station is infinite under the independent blockage model, and Theorem 17 states that the mean numbers of connected links among any set of links are the same under the two blockage models. So, I can conclude that infinitely many base stations are connected to this cluster under the correlated one. □

4.5 Conclusion

I investigated the connectivity results of multihop mmWave communication using stochastic geometry. Under the independent blockage model, I provided general results on the distribution of connected users to the typical user or the typical base station by leveraging classical results in random connection model. By using the percolation theory of the random connection model, the condition for existing an infinite connected user cluster is presented. For the cellular network model, I obtained the distribution of users connected to any base stations in one hop and two hops, and considered multihoming scenario where an infinite users cluster exists. Finally, the correlated blockage model is considered. I showed that the mean numbers of the connected links to the typical user/base station are the same for both blockage models. Unlike the independent blockage model, under a certain condition of blockages, there is no infinite connected user cluster. Multihoming scenario in the correlated

blockage setting is also considered.

4.6 Appendix

4.6.1 Lemma for Theorem 9

Lemma 9 (Percolation for the random connection model)**.** Let Φ be a homogeneous PPP in $\mathbb{R}^2$ of intensity $\lambda > 0$ and $f : \mathbb{R}^+ \to [0,1]$ be a nonincreasing function. Assume that each pair of points $x, y \in \Phi$ is connected with probability $f(\|x-y\|)$, independently of other pairs. Then, this graph has a critical density $\lambda_f \in (0, \infty)$

$$\lambda_f \geq \frac{1}{2\pi \int_0^\infty r f(r) dr},$$

such that, if $\lambda > \lambda_f$, then there exists a.s. an infinite connected component in this graph while, if $\lambda < \lambda_f$, then there is a.s. no infinite connected component.

The details of proof are in [72]. By plugging our connectivity function $C(\cdot,\cdot)$ and changing integral range from polar coordinate to Cartesian coordinate, Theorem 9 is obtained.

4.7 Proof of Theorem 12

The conditional intensity measures of Φ_u^1 and Φ_u^{1+} given $\Phi_{\mathrm{BS}} = \{X_i\}_{i\in\mathbb{N}}$ are

$$\Lambda^1_{c|\Phi_{\mathrm{BS}}}(B) = \int_B \lambda_u \left(1 - \prod_{X_i \in \Phi_{\mathrm{BS}}} (1 - C(x, X_i))\right) dx,$$

and

$$\Lambda^{1+}_{c|\Phi_{\mathrm{BS}}}(B) = \int_B \lambda_u \prod_{X_i \in \Phi_{\mathrm{BS}}} (1 - C(x, X_i))dx,$$

as in (4.5) and (4.6).

So by independent thinning of PPPs, the conditional intensity measure of Φ^2_u given $\Phi_{\mathrm{BS}} = \{X_i\}_{i\in\mathbb{N}}$ and $\Phi_u = \{Y_j\}_{j\in\mathbb{N}}$ is

$$\Lambda^2_{c|\Phi_{\mathrm{BS}},\Phi^1_u}(B) = \lambda_u \int_B \prod_{Y_j \in \Phi^1_u} (1 - C(x, Y_j)) \prod_{X_i \in \Phi_{\mathrm{BS}}} (1 - C(x, X_i))dx,$$

where $B \in \mathcal{B}(\mathbb{R}^2)$.

Finally, the conditional intensity meausre of Φ^2_u given $\Phi_{\mathrm{BS}} = \{X_i\}_{i\in\mathbb{N}}$ is

$$\Lambda^2_{u|\Phi_{\mathrm{BS}}}(B) = \lambda_u \int_B \left(1 - \exp(-\int_{\mathbb{R}^2} (1 - C(x, y))dy)\right) \prod_{X_i \in \Phi_{\mathrm{BS}}} (1 - C(x, X_i))dx,$$

and obtained by Laplace functional of PPPs [5].

4.7.1 Proof of Theorem 13

To compute the density of Φ^2_u, λ_2, the expectation of the number of points of Φ^2_u in $\mathcal{B}$ will be computed where $|\mathcal{B}| = 1$. Since Φ_{BS} and Φ^1_u are PPP

conditioned on Φ_{BS}, the properties of PPP are used for computing λ_2.

$$\begin{aligned}
\lambda_2 &\overset{(a)}{=} \mathbb{E}\left[\sum_{z\in\Phi_u^{1+}} \mathbb{1}_{z\in\mathcal{B}}\left(1-\prod_{y_j\in\Phi_u^1}(1-C(z,y_j))\right)\right] \\
&= \mathbb{E}_{\Phi_{\text{BS}}}\left[\mathbb{E}\left[\sum_{z\in\Phi_u^{1+}} \mathbb{1}_{z\in\mathcal{B}}\left(1-\prod_{y_j\in\Phi_u^1}(1-C(z,y_j))\right)|\Phi_{\text{BS}}\right]\right] \\
&\overset{(b)}{=} \mathbb{E}_{\Phi_{\text{BS}}}\left[\mathbb{E}_{\Phi_u^{1+}}\left[\sum_{z\in\Phi_u^{1+}} \mathbb{1}_{z\in\mathcal{B}}\left(1-\mathbb{E}_{\Phi_u^1}\left[\prod_{y_j\in\Phi_u^1}(1-C(z,y_j))\right]\right)|\Phi_{\text{BS}}\right]\right].
\end{aligned} \tag{4.7}$$

In (a), $\left(1-\prod_{y_j\in\Phi_u^1}(1-C(z,y_j))\right)$ is the probability that z is connected to at least one point of Φ_u^1. (b) comes from the fact that Φ_u^1 and Φ_u^{1+} are conditionally independent. By probability generating functional (PGFL) of a PPP [30], the expectation term over Φ_u^1 in (4.7) becomes

$$\begin{aligned}
\mathbb{E}_{\Phi_u^1}\left[\prod_{y_j\in\Phi_u^1}(1-C(z,y_j))\right] &\overset{(c)}{=} e^{-\int_{\mathbb{R}^2}(1-(1-C(z,y)))\Lambda^1_{c|\Phi_{\text{BS}}}(dy)} \\
&= e^{-\int_{\mathbb{R}^2} C(z,y)\Lambda^1_{c|\Phi_{\text{BS}}}(dy)}.
\end{aligned} \tag{4.8}$$

(c) comes from the fact that Φ_1 is a PPP conditioned on Φ_{BS}, and $\Lambda^1_{c|\Phi_{\text{BS}}}(\cdot)$ is defined in (4.5). By plugging (4.8) into (4.7),

$$
\begin{aligned}
\lambda_2 &= \mathbb{E}_{\Phi_{\text{BS}}}\left[\mathbb{E}_{\Phi_u^{1+}}\left[\sum_{z\in\Phi_u^{1+}} \mathbb{1}_{z\in\mathcal{B}}\left(1-e^{-\int_{\mathbb{R}^2} C(z,y)\Lambda^1_{c|\Phi_{\text{BS}}}(dy)}\right)|\Phi_{\text{BS}}\right]\right] \\
&= \mathbb{E}_{\Phi_{\text{BS}}}\left[\int_{\mathcal{B}}\left(1-e^{-\int_{\mathbb{R}^2} C(z,y)\Lambda^1_{c|\Phi_{\text{BS}}}(dy)}\right)\Lambda^{1+}_{c|\Phi_{\text{BS}}}(dz)\right] \\
&= \mathbb{E}_{\Phi_{\text{BS}}}\left[\int_{\mathcal{B}}\left(1-e^{-\int_{\mathbb{R}^2} C(z,y)\lambda_u(1-\prod_{x_i\in\Phi_{\text{BS}}}(1-C(y,x_i)))dy}\right)\lambda_u\prod_{x_i\in\Phi_{\text{BS}}}(1-C(z,x_i))dz\right] \\
&\overset{(d)}{=} \lambda_u\int_{\mathcal{B}}\mathbb{E}_{\Phi_{\text{BS}}}\left[\left(1-e^{-\lambda_u\int_{\mathbb{R}^2} C(z,y)(1-\prod_{x_i\in\Phi_{\text{BS}}}(1-C(y,x_i)))dy}\right)\prod_{x_i\in\Phi_{\text{BS}}}(1-C(z,x_i))\right]dz \\
&= \lambda_u\int_{\mathcal{B}}\mathbb{E}_{\Phi_{\text{BS}}}\left[\prod_{x_i\in\Phi_{\text{BS}}}(1-C(z,x_i))\right]dz \\
&\quad - \lambda_u\int_{\mathcal{B}}\mathbb{E}_{\Phi_{\text{BS}}}\left[e^{-\lambda_u\int_{\mathbb{R}^2} C(z,y)(1-\prod_{x_i\in\Phi_{\text{BS}}}(1-C(y,x_i)))dy}\prod_{x_i\in\Phi_{\text{BS}}}(1-C(z,x_i))\right]dz \\
&\overset{(e)}{=} \lambda_u\int_{\mathcal{B}} e^{-\lambda_{\text{BS}}\int_{\mathbb{R}^2} C(z,x)dx}dz \\
&\quad - \lambda_u\int_{\mathcal{B}} e^{-\lambda_u\int_{\mathbb{R}^2} C(z,y)dy}\mathbb{E}_{\Phi_{\text{BS}}}\left[e^{\lambda_u\int_{\mathbb{R}^2} C(z,y)\prod_{x_i\in\Phi_{\text{BS}}}(1-C(y,x_i))dy}\prod_{x_i\in\Phi_{\text{BS}}}(1-C(z,x_i))\right]dz.
\end{aligned}
\tag{4.9}
$$

(d) is by Fubini's theorem and $\Lambda^{1+}_{c|\Phi_{\text{BS}}}(\cdot)$ is defined in (4.6). (e) is by PGFL of a homogeneous PPP [30].

The expectation term over Φ_{BS} in (4.9) is

$$\begin{aligned}
&\mathbb{E}_{\Phi_{\text{BS}}}\left[e^{\lambda_u \int_{\mathbb{R}^2} C(z,y)\prod_{x_i\in\Phi_{\text{BS}}}(1-C(y,x_i))dy}\prod_{x_i\in\Phi_{\text{BS}}}(1-C(z,x_i))\right]\\
\overset{(f)}{=}&\mathbb{E}_{\Phi_{\text{BS}}}\left[\sum_{k=0}^{\infty}\frac{(\lambda_u\int_{\mathbb{R}^2}C(z,y)\prod_{x_i\in\Phi_{\text{BS}}}(1-C(y,x_i))dy)^k}{k!}\prod_{x_i\in\Phi_{\text{BS}}}(1-C(z,x_i))\right]\\
=&\sum_{k=0}^{\infty}\frac{1}{k!}\mathbb{E}_{\Phi_{\text{BS}}}\left[\left(\lambda_u\int_{\mathbb{R}^2}C(z,y)\prod_{x_i\in\Phi_{\text{BS}}}(1-C(y,x_i))dy\right)^k\prod_{x_i\in\Phi_{\text{BS}}}(1-C(z,x_i))\right].
\end{aligned}$$

(f) is by Taylor's expansion.

The k-th order term is

$$\begin{aligned}
&\frac{\lambda_u^k}{k!}\mathbb{E}_{\Phi_{\text{BS}}}\left[\left(\int_{\mathbb{R}^2}C(z,y)\prod_{x_i\in\Phi_{\text{BS}}}(1-C(y,x_i))dy\right)^k\prod_{x_i\in\Phi_{\text{BS}}}(1-C(z,x_i))\right]\\
=&\frac{\lambda_u^k}{k!}\mathbb{E}_{\Phi_{\text{BS}}}\left[\int_{\mathbb{R}^2}\dots\int_{\mathbb{R}^2}C(z,y_1)\dots C(z,y_k)\prod_{x_i\in\Phi_{\text{BS}}}\Big((1-C(y_1,x_i))\dots(1-C(y_k,x_i))\right.\\
&\left.\times(1-C(z,x_i))\Big)dy_1\dots dy_k\right]\\
=&\frac{\lambda_u^k}{k!}\int_{\mathbb{R}^2}\dots\int_{\mathbb{R}^2}C(z,y_1)\dots C(z,y_k)e^{-\lambda_{\text{BS}}\int_{\mathbb{R}^2}\left(1-\prod_{j=1}^k(1-C(y_j,x))(1-C(z,x))dx\right)}dy_1\dots dy_k.
\end{aligned}\tag{4.10}$$

By plugging (4.10) into (4.9),

$$\begin{aligned}
\lambda_2=&\lambda_u\int_{\mathcal{B}}e^{-\lambda_{\text{BS}}\int_{\mathbb{R}^2}C(z,x)dx}dz\\
&-\lambda_u\int_{\mathcal{B}}e^{-\lambda_u\int_{\mathbb{R}^2}C(z,y)dy}\left[\sum_{k=0}^{\infty}\frac{\lambda_u^k}{k!}\int_{\mathbb{R}^2}\dots\int_{\mathbb{R}^2}C(z,y_1)\dots C(z,y_k)\right.\\
&\left.\times e^{-\lambda_{\text{BS}}\int_{\mathbb{R}^2}\left(1-\prod_{j=1}^k(1-C(y_j,x))(1-C(z,x))\right)dx}dy_1\dots dy_k\right]dz,
\end{aligned}$$

where $|\mathcal{B}| = 1$.

4.7.2 Proof of Theorem 17

n links with length less than R are considered and let R_i be the region for determining the i-th link is connected as in Figure 4.2. Then, the mean numbers of the connected links among them are

$$\sum_{i=1\ldots n} \exp(-|R_i|),$$

for both the correlated and the independent cases.

The proof is simple for the independent case, since the i-th link is connected with probability $\exp(-|R_i|)$ and the connectivity is independent over links.

Now let us consider the correlated case. The i-th link is connected if and only if any points in Φ_b are not in R_i. The probability that only the k links with length $L_1, L_2, \ldots, L_k$ are connected is

$$\begin{aligned}
&\mathbb{P}\left[\left|\Phi_b \cap \bigcup_{i=1,\ldots,k} R_i\right| = 0, \text{ and } |\Phi_b \cap R_l| \geq 1 \text{ for } l = (k+1), \ldots, n\right] \\
&= \exp\left(-\lambda_b \left|\bigcup_{i=1,\ldots,k} R_i\right|\right) - \sum_{j_1 \in \{1,\ldots,n\}\setminus\{1,\ldots,k\}} \exp\left(-\lambda_b \left|\bigcup_{i=1,\ldots,k} R_i \cup R_{j_1}\right|\right) \\
&+ \ldots + (-1)^{n-k} \sum_{j_1,\ldots,j_{n-k} \in \{1,\ldots,n\}\setminus\{1,\ldots,k\}} \exp\left(-\lambda_b \left|\bigcup_{i=1,\ldots,k} R_i \cup \bigcup_{j=j_1,\ldots,j_{n-k}} R_j\right|\right),
\end{aligned} \tag{4.11}$$

when there exists n links.

(4.11) can be proven by induction. The case with $n = 1$ is simple since the probability that $k = 1$ is $\exp(-\lambda_b|R_1|)$ and the probability that $k = 0$ is $1 - \exp(-\lambda_b|R_1|)$. Now, it is assumed that (4.11) holds for $k \in \{0, 1, \ldots, m\}$ for $n = m$. Now, (4.11) for the case with $k \in \{0, 1, \ldots, m+1\}$ for $n = m+1$ will be proven.

First, the case with $k \in \{1, \ldots, m+1\}$ is considered when $n = m+1$. The probability that only k links with $L_1, L_2, \ldots, L_k$ are connected is

$$
\begin{aligned}
&\mathbb{P}\left[\left|\Phi_b \cap \bigcup_{i=1,\ldots,k} R_i\right| = 0, \text{ and } |\Phi_b \cap R_l| \geq 1 \text{ for } l = (k+1), \ldots, m+1\right] \\
&= \mathbb{P}\left[\left|\Phi_b \cap \bigcup_{i=1,\ldots,k} R_i\right| = 0\right] \times \mathbb{P}\left[\left|\Phi_b \cap (R_l \cap \left(\bigcup_{i=1,\ldots,k} R_i\right)^c)\right| \geq 1 \text{ for } l = (k+1), \ldots, m+1\right] \\
&\overset{(a)}{=} \exp\left(-\lambda_b \left|\bigcup_{i=1,\ldots,k} R_i\right|\right) \times \left(1 - \sum_{j_1 \in \{k+1,\ldots,m+1\}} \exp\left(-\lambda_b \left|R_{j_1} \cap \left(\bigcup_{i=1,\ldots,k} R_i\right)^c\right|\right)\right. \\
&\left. + \ldots + (-1)^{m+1-k} \sum_{j_1,\ldots,j_{m+1-k} \in \{k+1,\ldots,m+1\}} \exp\left(-\lambda_b \left|\bigcup_{j=j_1,\ldots,j_{m+1-k}} \left(R_j \cap \left(\bigcup_{i=1,\ldots,k} R_i\right)^c\right)\right|\right)\right) \\
&= \exp\left(-\lambda_b \left|\bigcup_{i=1,\ldots,k} R_i\right|\right) - \sum_{j_1 \in \{1,\ldots,m+1\} \setminus \{1,\ldots,k\}} \exp\left(-\lambda_b \left|\bigcup_{i=1,\ldots,k} R_i \cup R_{j_1}\right|\right) \\
&+ \ldots + (-1)^{m+1-k} \sum_{j_1,\ldots,j_{m+1-k} \in \{1,\ldots,m+1\} \setminus \{1,\ldots,k\}} \exp\left(-\lambda_b \left|\bigcup_{i=1,\ldots,k} R_i \cup \bigcup_{j=j_1,\ldots,j_{m+1-k}} R_j\right|\right),
\end{aligned}
$$

where A^c is the complement set of A. (a) is obtained by the induction assumption with index changing.

Under the case for $k = 0$ when $n = m + 1$,

$$\mathbb{P}\left[(\text{no link is connected})\right] = 1 - \sum_{j=1}^{m+1} \mathbb{P}[(j \text{ links are connected.})]$$

$$= 1 - \sum_{j_1 \in \{1,\ldots,m+1\}} \exp\left(-\lambda_b \left|R_{j_1}\right|\right)$$

$$+ \ldots + (-1)^{m+1} \sum_{j_1,\ldots,j_{m+1} \in \{1,\ldots,m+1\}} \exp\left(-\lambda_b \left| \bigcup_{j=j_1,\ldots,j_{m+1}} R_j \right|\right).$$

More precisely, the coefficient of a randomly chosen term

$$\exp\left(-\lambda_b \left| \bigcup_{i=i_1,i_2,\ldots,i_l} R_i \right|\right),$$

for $l \leq m+1$ and $\{i_1, \ldots, i_l\} \in \{1, \ldots, m+1\}$ is

$$-\left(1 - \binom{l}{1} + \binom{l}{2} - \ldots + (-1)^{l-1}\binom{l}{l-1}\right) = -(1-1)^l + (-1)^l = (-1)^l. \tag{4.12}$$

In (4.12), $\binom{l}{i}$ comes from the probability of the sum of $l - i$ connected links.

Now, it will be shown that the mean number of connected links under the correlated shadowing is $\sum_{i=1,\ldots,n} \exp(-\lambda_b |R_i|)$. The mean number of connected links is

$$\sum_{s=1}^{n} s \sum_{l_1,\ldots,l_s \in \{1,\ldots,n\}} \mathbb{P}\left[j_1, \ldots, j_s\text{-th link are connected.}\right]$$

$$= \sum_{s=1}^{n} s \left[\sum_{l_1,\ldots,l_s \in \{1,\ldots,n\}} \left(\exp\left(-\lambda_b \left| \bigcup_{i=l_1,\ldots,l_s} R_i \right|\right) - \sum_{j_1 \in \{1,\ldots,n\}\setminus\{l_1,\ldots,l_s\}} \exp\left(-\lambda_b \left| \bigcup_{i=l_1,\ldots,l_s} R_i \cup R_{j_1} \right|\right) \right.\right.$$

$$\left.\left. + \ldots + (-1)^{n-s} \sum_{j_1,\ldots,j_{n-s} \in \{1,\ldots,n\}\setminus\{l_1,\ldots,l_s\}} \exp\left(-\lambda_b \left| \bigcup_{i=l_1,\ldots,l_s} R_i \cup \bigcup_{j=j_1,\ldots,j_{n-s}} R_j \right|\right) \right) \right]$$

$$\overset{(b)}{=} \sum_{s=1,\ldots,n} \exp(-\lambda_b |R_s|).$$

(b) is obtained since the coefficient of

$$\exp\left(-\lambda_b \left| \bigcup_{j=j_1,\ldots,j_k} R_j \right| \right),$$

for $k \geq 1$ is

$$\begin{aligned} & k - \binom{k}{1}(k-1) + \binom{k}{2}(k-2) - \ldots + (-1)^{k-1}\binom{k}{k-1} \\ & = k\left(1 - \binom{k-1}{1} + \binom{k-1}{2} - \ldots + (-1)^{k-1}\binom{k-1}{k-1}\right) \\ & = k(1-1)^{k-1} = 0, \end{aligned}$$

and the coefficient of $\exp(-\lambda_b|R_i|)$ is 1 which is obtained the probability of only i-th link is connected.

Chapter 5

Scaling Laws for Ergodic Spectral Efficiency in MIMO Poisson Networks

This chapter[1] considers MIMO ad-hoc networks modeled by a *Poisson bipolar network*. This chapter shows that spatial multiplexing transmission methods are essential for obtaining better ergodic spectral efficiency in random wireless networks with multiple antennas.

5.1 Introduction

A multiple-input-multiple-output mobile ad hoc network (MIMO-MANET) is an infrastructure-less network in which a large number of transmit-and-receive pairs, each with multiple antennas, communicate by sharing some common spectrum [85, 86]. Such networks are fundamental in a variety of applications including car-to-car and device-to-device communication systems [87–89]. It is therefore of great importance to characterize the system-level performance of such networks [6, 7, 90].

Despite extensive research over a few decades, analytical expressions

[1]This chapter has been published in [84]. I am the primary author of these works. Coauthor Dr. Namyoon Lee has provided many discussions and insightful feedbacks to this work, and Dr. Françcois Baccelli is my supervisor.

for the spectral efficiency of such systems are still missing. The principal difficulty has been the lack of a tractable model quantifying uncoordinated inter-node interference together with inter-stream interference at a receiver equipped with multiple antennas. In this chapter, this chapter leverages two analytical tools to cope with this difficulty. The first one is stochastic geometry which models the locations of links as Poisson dipoles [14] and allows one to compute the distribution of the interference power. The second one is random matrix theory [91], which is exploited for calculating the distribution of inter-stream interference power under different MIMO detection techniques. Combining these tools, this chapter characterizes the ergodic spectral efficiencies and the scaling laws of a super-dense MIMO-MANET system, under Poisson assumptions on the node locations, and when considering two types of channel knowledge at receivers. By leveraging the integral-form expressions which are derived, this chapter highlights the interplay among four key system parameters determining the scaling laws, namely the number of antennas at the transmitter, the number of antennas at the receiver, the node density, and the path-loss exponent.

5.1.1 Related Works

There has been extensive work on the capacity of MIMO-MANETs. MIMO-MANETs can be modeled as MIMO interference networks in which a finite number of transmit-and-receiver pairs communicate by sharing the same spectrum, without transmitter cooperation. [6] studied the capacity of

a MIMO-MANET by treating inter-node interference as additional noise at a receiver, and derived the optimal power allocation strategy for the MIMO transmission. For instance, in a certain range of interference-to-noise ratios, it turns out that allocating the whole power to one antenna (i.e., using a single stream transmission) is optimal. [7] and [8] extended the result of [6], and demonstrated that the asymptotic spectral efficiency is improved by sending multiple data streams. A common assumption of these studies is that the distances between any two nodes in the network are deterministic [6] or identical [7], which is unrealistic to model MANETs in practice. This approach cannot be used to assess which MIMO transmission techniques provide the highest gains in large random MANETs.

When considering more realistic random network topology assumptions, the rates achievable in MANETs have been studied in [85, 90, 92–96]. The study of scaling laws within this context was initiated by Gupta and Kumar's seminal paper [85]. Under the assumption that n nodes are randomly located in the unit disk, Gupta and Kumar showed that multihop routing based on a decode-and-forward scheme can reach to a total throughput which scales as $\Theta(\sqrt{n/\log n})$. By using percolation theory, it was later shown in [92] that a better scaling law of order $\Theta(\sqrt{n})$ is achievable. Subsequently, improved scaling results were derived in MANETs, assuming that some specific additional assumptions hold on mobility [94], bandwidth [95], or node-cooperation [90]. The main differences between our work and this line of research are the following: (1) our model is based on Poisson dipoles

and assumes that source-destination pairs communicate with each other relying upon single-hop transmissions, i.e., neither multi-hop routing schemes nor node-cooperation are allowed (in a sense, this chapter is more focussed on D2D than on MANETs). (2) this chapter focuses on the use of multiple antennas at both transmitters and receivers, while this line of research was centered on the scenario with a single antenna at both transmitters and receivers. (3) our performance metric is spatially-averaged ergodic spectral efficiency, while the work alluded to above focused on transport capacity. (4) even if new scaling laws are our main results, our approach also provides exact formulas for the mean Shannon rate of a typical link and the spectral efficiency per unit area (see e.g. Theorems 20 and 21 below), and goes hence beyond the scaling law setting.

This chapter assumes that the interferer locations are Poisson distributed over the plane [5, 97], which is an appropriate model for e.g. D2D, where transmitters are randomly located in an uncoordinated manner. Using this model, the transmission capacity of ad hoc networks, which quantifies the maximum allowable spatial density of successful transmissions per unit area, subject to a given outage probability constraint, was characterized in certain settings. For example, the transmission capacity expressions of ad hoc networks were found when adopting spread spectrum techniques [9, 98], interference cancellation [99–101], and multiple-antenna transmission methods [10, 11, 102–107]. In particular, in [10], it was demonstrated that interference cancellation techniques at a receiver employing multiple antennas can

provide a linear increase of the transmission capacity of ad hoc networks with the node density. In [11], it was shown that for a MIMO setting, a single stream transmission is optimal in terms of transmission capacity, when all the degrees of freedom of the receive antennas are used for interference cancellation.

Arguably, a common shortcoming of the transmission capacity metric is that it cannot capture the effects of rate adaptation techniques, which are the key features used in many modern wireless systems to track and exploit channel variations [108]. The main novelty of this chapter compared to this line of thought is the analysis of the ergodic spectral efficiency (rather than transport capacity), which quantifies the achievable Shannon transmission rate per unit area when adapting the rate to the different local conditions. For a single-input-multiple-output (SIMO) setting, the recent work in [109] showed that the sum spectral efficiency can increase linearly with both the density and the path loss exponent provided the number of antennas is a linear function of the density. For a MIMO setting, however, it is still unknown whether *spatial multiplexing* transmission techniques [110] can improve the scaling laws of the sum spectral efficiency. This chapter recalls that *spatial multiplexing* consists in transmitting different data streams on the transmit antennas and in identifying/discriminating between these streams at the receiver, while *transmit diversity* consists in sending the same data symbols over multiple transmit antennas to enhance the reliability. The main qualitative achievement of this chapter is a proof that the answer to this question is positive and more precisely the identification of the network densities and antenna configurations

for which *spatial multiplexing* strategies achieve higher sum spectral efficiency per unit area than the methods based on *transmit diversity*.

5.1.2 Main Contributions

This chapter considers a random network with a topology modeled by a *Poisson bipolar network* [14] with density λ on $\mathbb{R}^2$. In this model, each transmitter has its receiver at some random distance. Also, each transmitter has N_{t} antennas and is assumed to send N_{t} data streams to its associated receiver which has $N_{\mathrm{r}}(\geq N_{\mathrm{t}})$ antennas. Our key findings can be summarized as follows:

- This chapter first considers the case where each receiver has knowledge of the state of the channel between its transmitter and itself only. This chapter refers to this channel knowledge assumption as *direct channel state information (CSI)* at receiver (DCSIR). Under the premise of this channel knowledge, and under zero-forcing (ZF) detection and ZF-based successive interference cancellation (ZF-SIC) detection respectively, this chapter derives analytical expressions for the sum spectral efficiency as a function of 1) the network density λ, 2) the number of transmit and receive antennas (N_{t} and N_{r}), 3) the path-loss exponent α, and 4) the signal-to-noise ratio (SNR). By deriving closed forms of lower and upper bound on this sum spectral efficiency, this chapter shows that, as λ goes to infinity, when $N_{\mathrm{t}} = c_1\lambda^{\beta_1}$, $N_{\mathrm{r}} = c_2\lambda^{\beta_2}$ for some constants $c_1, c_2 > 0$, $\beta_1 \leq \beta_2$ and $\alpha > 2$, the scaling laws of the ergodic spectral efficiency per

link is

$$\Theta(\lambda^{\beta_1} \log_2(1 + \lambda^{\beta_2 - \beta_1 - \frac{\alpha}{2}})),$$

for both ZF and ZF-SIC. One important implication of this scaling law is that when $\beta_2 \geq \beta_1 + \frac{\alpha}{2}$, transmitting multiple streams is more beneficial in the scaling law sense than sending just a single stream, which strongly contrasts with the result derived on transmission capacity [11]. In fact, this result agrees with the intuition that it should be possible to improve the data rates per link by having $N_{\mathrm{t}} = c_1 \lambda^{\beta_1}$ and by transmitting multiple data streams (*multiplexing gain*), provided the remaining degrees of freedom at the receiver are sufficient to cancel both inter-stream interference and inter-node interference and to discriminate between the independent data streams. Furthermore, this scaling law expression generalizes the result for the SIMO case derived in [109] to the MIMO case.

- This chapter also considers the case where each receiver is able to learn the CSI of its L-nearest interferers with $(0 < L \leq \lfloor \frac{N_{\mathrm{r}}}{N_{\mathrm{t}}} \rfloor - 1)$[2], which is referred to here as *local CSI* at receiver (LCSIR)[3]. Using a ZF-SIC detection technique for suppressing both inter-stream and inter-node interference, this chapter gives an exact expression of the sum spectral

[2] $\lfloor x \rfloor$ denotes the largest integer no more than x.

[3] This assumption can be justified by a practical protocol, FlashlinQ [111]. FlashlinQ operates using a protocol, in which each transmitter sends pilot signals using orthogonal resources across neighbors and the receivers estimate the neighbors' channel state information to perform the SIR-aware scheduling, which is referred to as *transmit and receive yieldings*. It was showed that the protocol can successfully discover up to a few thousand devices over a 1 km radius. By leveraging this protocol, the receiver is able to learn CSIR locally.

efficiency. By leveraging this expression, an achievable scaling law of the sum spectral efficiency per link is obtained as:

$$\Omega(\lambda^{\beta_1}(\log_2(1+\lambda^{(\beta_2-\beta_1-1)\frac{\alpha}{2}}))),$$

when $N_{\mathrm{t}} = c_1\lambda^{\beta_1}$ and $N_{\mathrm{r}} = c_2\lambda^{\beta_2}$, for some constants $c_1, c_2 > 0$ and $\beta_1 \leq \beta_2$, $\alpha > 2$, and for $L = \lfloor \frac{N_{\mathrm{r}}}{N_{\mathrm{t}}} \rfloor - 1$. This result also demonstrates that MIMO transmission improves the scaling law of the ergodic spectral efficiency per link by increasing multiplexing gains, provided $\beta_2 \geq \beta_1 + 1$. Comparing to DCSIR, it is possible with LCSIR to increase the sum spectral efficiency when acting on both the path-loss exponent and the number of transmit antennas. This multiplicative gain in the achievable scaling law comes from the fact that the receiver exploits LCSIR.

This chapter is organized as follows. The network model, the performance metrics, and the receiver schemes are discussed in Section 5.2. The exact expression and the scaling law for ergodic spectral efficiency are provided in Section 5.3 in the DCSIR case and in Section 5.4 in the LCSIR case. This chapter concludes in Section 5.5.

5.2 System Model

5.2.1 Network Model

This chapter considers a *Poisson bipolar network model* which features an infinite number of transmitter-receiver pairs scattered in the Euclidean plane. Let $\Phi = \{X_i\}_{i\in\mathbb{N}}$ denote the locations of the transmitters, which are

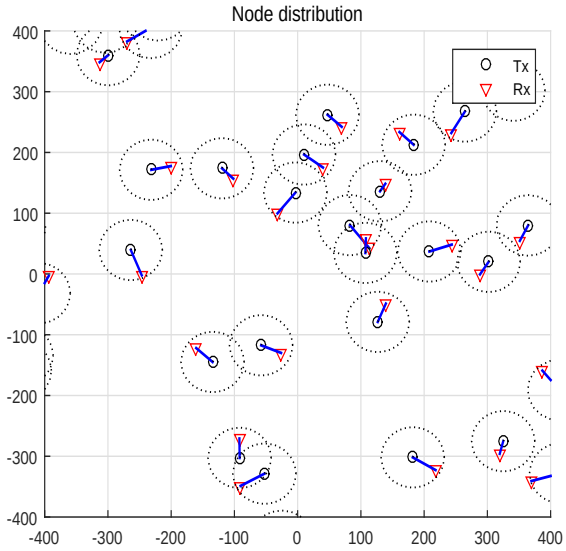

Figure 5.1: A snapshot of bipolar MANET where $\lambda = 0.00004/m^2$ and $R_d = 50m$.

assumed to form some realization of a homogeneous Poisson point process (PPP) with positive and finite intensity λ on $\mathbb{R}^2$. Let $\bar{\Phi} = \{Y_i\}_{i\in\mathbb{N}}$ denote the locations of the receivers. Y_i, the receiver of X_i, is assumed to be uniformly distributed on a ring with inner radius 1 and outer radius R_d centered at X_i, where $R_d > 1$. Fig. 5.1 provides a snapshot of network topology with $R_d = 50m$ and $\lambda = 0.000004/m^2$. This chapter assumes that each receiver is equipped with a fixed number of N_r antennas, whereas transmitters have a random number N_t in $[1, N_\mathrm{r}] \in \mathbb{N}$ of antennas. The probability of having k transmit antennas is denoted by p_k, where $\sum_{k=1}^{N_\mathrm{r}} p_k = 1$. The number of transmit antennas is assumed independent and identically distributed (i.i.d.) over links.

5.2.2 Signal Model

A transmitter $X_k \in \Phi$ communicates with its associated receiver Y_k, and sends a signal $\mathbf{s}_k \in \mathbb{C}^{N_{\mathrm{t},k}\times 1}$ when X_k has $N_{\mathrm{t},k}$ antennas, $(1 \leq N_{\mathrm{t},k} \leq N_{\mathrm{r}})$, with power constraint $\mathbb{E}[\|\mathbf{s}_k\|^2] = P$. Here, it is assumed that the transmit power is equally allocated to all antennas. Assuming a frequency-flat channel, the received signal at the k-th receiver, $\mathbf{y}_k \in \mathbb{C}^{N_{\mathrm{r}}\times 1}$ is

$$\mathbf{y}_k = \sum_{l, X_l \in \Phi} d_{k,l}^{-\frac{\alpha}{2}} \mathbf{H}_{k,l}\mathbf{s}_l + \mathbf{z}_k, \tag{5.1}$$

where $\mathbf{H}_{k,l} \in \mathbb{C}^{N_{\mathrm{r}}\times N_{\mathrm{t},l}}$ is the channel matrix and $d_{k,l}$ the distance from X_l to Y_k, respectively. Moreover, $\mathbf{z}_k \in \mathbb{C}^{N_{\mathrm{r}}\times 1}$ is the noise vector at receiver Y_k. Furthermore, it is assumed that all entries of $\mathbf{H}_{k,l}$ are i.i.d. complex Gaussian random variables with zero mean and unit variance, i.e. $\mathcal{CN}(0,1)$, and that all entries of $\mathbf{z}_k$ are i.i.d. $\mathcal{CN}(0,\sigma^2)$, where σ^2 is the noise variance.

5.2.3 Receive Filters and Performance Metrics

It is assumed that receiver Y_k can measure CSI from its associated transmitter X_k and from the L_k nearest transmitters, i.e. $\{X_{k_i}\}_{i=1}^{L_k}$, where $0 \leq L_k \leq \max\{n | \sum_{i=1}^{n} N_{\mathrm{t},j_i} \leq N_{\mathrm{r}} - N_{\mathrm{t},k}\}$[4]. It will be assumed that X_k sends $N_{\mathrm{t},k}$ data streams without using any precoding, i.e., that an open-loop MIMO transmission is used, and also that the receiver uses linear receive filters to

[4]With this condition, the number of received data streams at Y_k is no larger than N_{r}. This assumption is necessary for decoding the independent data streams in ZF and ZF-SIC. If all transmitters are equipped with N_{t} antennas, $L_k = \lfloor \frac{N_{\mathrm{r}}}{N_{\mathrm{t}}} \rfloor - 1, \forall k \in \mathcal{K}$. Further, the j-th nearest interferer from Y_k is denoted by X_{k_j}.

detect the desired data symbol by eliminating the *inter-stream interference* and the *inter-node interference*.

Let $\mathbf{v}_k(m) \in \mathbb{C}^{N_\mathrm{r}\times 1}$, $m = 1, \ldots, N_{\mathrm{t},k}$, denote the receive filter vector used at Y_k for detecting the m-th data stream from its transmitter. Then, the resulting signal-to-interference-and-noise ratio (SINR) for the m-th data stream of the k-th link is

$$\mathrm{SINR}_k(m) = \frac{H_{k,k}(m) d_{k,k}^{-\alpha}}{I_{k1}(m) + I_{k2}(m) + I_{k3}(m) + \frac{N_{\mathrm{t},k}\sigma^2}{P}}, \tag{5.2}$$

where

$$\begin{aligned}
H_{k,k}(m) &= \|\mathbf{v}_k^*(m)\mathbf{H}_{k,k}(:,m)\|^2, \\
I_{k1}(m) &= \sum_{i=1,\ldots,N_{\mathrm{t},k}}^{i\neq m} \|\mathbf{v}_k^*(m)\mathbf{H}_{k,k}(:,i)\|^2 d_{k,k}^{-\alpha}, \\
I_{k2}(m) &= \sum_{l\in\{k_1,k_2,\ldots,k_{L_k}\}} \|\mathbf{v}_k^*(m)\mathbf{H}_{k,l}\|^2 d_{k,l}^{-\alpha}, \\
I_{k3}(m) &= \sum_{l,X_l\in\{\Phi\setminus X_k, X_{k_1}, X_{k_2},\ldots,X_{k_{L_k}}\}} \|\mathbf{v}_k^*(m)\mathbf{H}_{k,l}\|^2 d_{k,l}^{-\alpha}.
\end{aligned}$$

Here, the conjugate transpose is denoted by $*$ and the i-th column of the matrix $\mathbf{A}$ by $\mathbf{A}(:,i)$. As can be seen in (5.2), the total amount of interference at the receiver can be decomposed into three factors: 1) the *inter-stream interference* I_{k1}, 2) the *inter-node interference* from the L_k-dominant interferers, I_{k2}, and 3) the *inter-node interference*, I_{k3}, which is the interference from the other nodes. Then, the achievable rate of the k-th link is

$$C_k = \sum_{m=1}^{N_{\mathrm{t},k}} C_k(m) = \sum_{m=1}^{N_{\mathrm{t},k}} \log_2(1 + \mathrm{SINR}_k(m)).$$

The main target performance metric in this chapter is *ergodic spectral efficiency*. The sum spectral efficiency per unit area is defined by

$$\begin{aligned} C &= \tfrac{1}{|\mathcal{A}|} C_{\mathcal{A}} = \tfrac{1}{|\mathcal{A}|} \mathbb{E}\left[\textstyle\sum_{k, Y_k \in \mathcal{A}} C_k\right] \\ &= \lambda \mathbb{E}^0 \left[\sum_{m=1}^{N_{\mathrm{t},0}} \log_2(1 + \mathrm{SINR}_0(m))\right], \end{aligned} \tag{5.3}$$

where for any $\mathcal{A} \subset \mathbb{R}^2$, $|\mathcal{A}|$ is the area of $\mathcal{A}$, $C_{\mathcal{A}}$ is the sum spectral efficiency of $\mathcal{A}$, and $\mathbb{E}^0$ denotes the Palm expectation [5] of the receiver PPP. The fact that the last expression does not depend on the choice of $\mathcal{A}$ results from the stationarity assumptions [5]. Here, SINR_0 denotes the SINR measured at the receiver located at the origin[5]. Furthermore, the *spectral efficiency of the typical link*, or equivalently the *spectral efficiency* per link is defined by

$$C_{\mathrm{link}} = \frac{1}{\lambda} C = \mathbb{E}^0 \left[\sum_{m=1}^{N_{\mathrm{t},0}} \log_2(1 + \mathrm{SINR}_0(m))\right].$$

Here, for the above quantities, the terms ergodic spectral efficiency or ergodic spectral efficiency per link will be used, respectively. The ergodicity is over both the time-domain (averaging over the small-scale multipath fading) and over space (averaging over all Poisson configurations).

The sum spectral efficiency per unit area will be denoted by C^{ZF} under ZF, and by C^{SIC} under ZF-SIC, the sum spectral efficiency in region $\mathcal{A} \subset$

[5]By *Slivnyak's theorem* [5], it is possible locate the typical receiver at the origin. the typical transmitter and the typical receiver are labelled by X_0 and $Y_0 = 0$, respectively. The distance between Y_0 and $\{X_k\}_{k \in \{0\} \cup \mathbb{N}}$, the channel matrix $\mathbf{H}_{0,l}, l \in \{0\} \cup \mathbb{N}$, the linear receiver filter $\mathbf{v}_0(m)$, $I_0(m)$, and the j-th nearest interferers from Y_0, i.e., X_{0_j} are defined similarly.

$\mathbb{R}^2$ with ZF by $C_{\mathcal{A}}^{\mathrm{ZF}}$ under ZF and by $C_{\mathcal{A}}^{\mathrm{SIC}}$ under ZF-SIC, and the spectral efficiency per link by $C_{\mathrm{link}}^{\mathrm{ZF}}$ under ZF by $C_{\mathrm{link}}^{\mathrm{SIC}}$ under ZF-SIC.

5.2.3.1 ZF detection

The main idea of the *ZF-decorrelator* [110] is to construct $\mathbf{v}_k(m)$ so as to remove both $I_{k1}(m)$ and $I_{k2}(m)$ simultaneously by projecting the received signal vector onto the subspace orthogonal to that spanned by the vectors $\mathbf{H}_{k,k}(:,1),\ldots,\mathbf{H}_{k,k}(:,m-1),\mathbf{H}_{k,k}(:,m+1),\ldots,\mathbf{H}_{k,k}(:,N_{\mathrm{t},k})$, and the column vectors of $\mathbf{H}_{k,k_1},\ldots,\mathbf{H}_{k,k_{L_k}}$. Let $\mathbf{U}_k(m)$ be the null space of these column vectors; the dimension of $\mathbf{U}_k(m)$ is $N_{\mathrm{r}} \times (N_{\mathrm{r}} - (N_{\mathrm{t},k}-1) - \sum_{i=1}^{L_k} N_{\mathrm{t},k_i})$ with probability 1.[6] By definition of L_k, $N_{\mathrm{r}} - (N_{\mathrm{t},k}-1) - \sum_{i=1}^{L_k} N_{\mathrm{t},k_i} \geq 1$.

This chapter considers maximizing the desired signal power by choosing $\mathbf{v}_k(m)$ in the space spanned by $\mathbf{U}_k(m)$. More precisely, $\mathbf{v}_k(m)$ is designed for maximizing $|\mathbf{v}_k^*(m)\mathbf{H}_{k,k}(:,m)|^2$. If the columns of $\mathbf{U}_k(m)$ are orthonormal bases of the null space, then the following filter maximizes $|\mathbf{v}_k^*(m)\mathbf{H}_{k,k}(:,m)|^2$:

$$\mathbf{v}_k(m) = \mathbf{U}_k(m)\mathbf{U}_k^*(m)\mathbf{H}_{k,k}(:,m).$$

By applying this filter, $I_{k1}(m)$ and $I_{k2}(m)$ are suppressed and the resulting SINR becomes

$$\mathrm{SINR}_k^{\mathrm{ZF}}(m) = \frac{H_{k,k}(m)d_{k,k}^{-\alpha}}{I_k(m) + \frac{N_{\mathrm{t},k}\sigma^2}{P}},$$

[6] $N_{\mathrm{t},k}-1$ comes from the dimension of the subspace spanned by $\mathbf{H}_{k,k}(:,1),\ldots,\mathbf{H}_{k,k}(:,m-1),\mathbf{H}_{k,k}(:,m+1),\ldots,\mathbf{H}_{k,k}(:,N_{\mathrm{t},k})$ and $\sum_{i=1}^{L_k} N_{\mathrm{t},k_i}$ from the dimension of $\mathbf{H}_{k,k_1},\ldots,\mathbf{H}_{k,k_{L_k}}$.

where

$$I_k(m) = I_{k3}(m) = \sum_{l, X_l \in \{\Phi \setminus X_k, X_{k_1}, X_{k_2}, \ldots, X_{k_{L_k}}\}} H_{k,l}(m) d_{k,l}^{-\alpha}$$

and $H_{k,k}(m) = \|\mathbf{v}_k^*(m)\mathbf{H}_{k,k}\|^2$ is a Chi-squared random variable[7] with $2(N_{\mathrm{r}} - N_{\mathrm{t},k} - \sum_{l=1}^{L_k} N_{\mathrm{t},k_l} + 1)$ degrees of freedom [110] and $H_{k,l}(m) = \|\mathbf{v}_k^*(m)\mathbf{H}_{k,l}\|^2$ is distributed as a Chi-squared with $2N_{\mathrm{t},l}$ degrees of freedom [110]. Since ZF receivers does not change the interference power distribution from each interferer, interference is the sum of i.i.d. $N_{t,l}$ exponential random variables. This is the main reason why the interferemce measured at the typical receiver is the sum of $\mathcal{X}_{2N_{t,l}}$. The sum spectral efficiency per unit area hence becomes

$$C^{\mathrm{ZF}} = \lambda C_{\mathrm{link}}^{\mathrm{ZF}} = \lambda \mathbb{E}^0 \left[\sum_{m=1}^{N_{\mathrm{t},0}} \log_2(1 + \mathrm{SINR}_0^{\mathrm{ZF}}(m)) \right]. \tag{5.4}$$

5.2.3.2 ZF-SIC detection

The key idea of ZF-SIC decoding [110] is to recover and to subtract a data stream successively for obtaining the remaining data streams. This provides a power gain as well as an interference cancellation gain. For decoding the m-th data stream of the k-th link, the 1st to $(m-1)$-th data streams are

[7] The probability density function of the Chi-square distribution with $2n$ degrees of freedom, $\mathcal{X}_{2n}^2$, is $f_{\mathcal{X}_{2n}^2}(x) = \frac{x^{n-1}e^{-x}}{(n-1)!}$. Further, since the decoding procedure is performed at each receiver with known information, the randomness of the number of transmit antenna $N_{t,k}$ disappears. Therefore, it is possible to conclude that $H_{k,k}(m)$ is a Chi-squared random variable.

subtracted off from the received vector $\mathbf{y}_k$ and the decorrelator for the m-th data stream is applied to the subtracted vector for suppressing the $(m+1)$-th to $N_{\mathrm{t},k}$-th streams of the k-th link. In other words, the corresponding projection is onto the subspace orthogonal to $\mathbf{H}_{k,k}(:, m+1), \ldots, \mathbf{H}_{k,k}(:, N_{\mathrm{t},k})$ (say $\tilde{\mathbf{U}}_k(m)$), as opposed to being to the subspace orthogonal to $\mathbf{H}_{k,k}(:, 1), \ldots, \mathbf{H}_{k,k}(:, m-1), \mathbf{H}_{k,k}(:, m+1), \ldots, \mathbf{H}_{k,k}(:, N_{\mathrm{t},k})$ and the column spaces of $\mathbf{H}_{k,k_1}, \ldots, \mathbf{H}_{k,k_{L_k}}$ in the previous subsection. By choosing $\tilde{\mathbf{v}}_k(m)$ in $\tilde{\mathbf{U}}_k(m)$ to maximize the signal power, the resulting SINR becomes

$$\mathrm{SINR}_k^{\mathrm{SIC}}(m) = \frac{\tilde{H}_{k,k}(m) d_{k,k}^{-\alpha}}{\tilde{I}_k(m) + \frac{N_{\mathrm{t},k}\sigma^2}{P}},$$

where

$$\tilde{I}_k(m) = I_{k3}(m) = \sum_{l, X_l \in \{\Phi \setminus X_k, X_{k_1}, X_{k_2}, \ldots, X_{k_{L_k}}\}} \tilde{H}_{k,l}(m) d_{k,l}^{-\alpha},$$

and $\tilde{H}_{k,k}(m) = \|\tilde{\mathbf{v}}_k^*(m)\mathbf{H}_{k,k}\|^2$ is a Chi-squared random variable with $2(N_{\mathrm{r}} - N_{\mathrm{t},k} + m)$ degrees of freedom[8] and $\tilde{H}_{k,l}(m) = \|\tilde{\mathbf{v}}_k^*(m)\mathbf{H}_{k,l}\|^2$ is distributed as a Chi-squared with $2N_{\mathrm{t},l}$ degrees of freedom.

Similarly, the sum spectral efficiency per unit area achieved by the ZF-SIC is given by

$$C^{\mathrm{SIC}} = \lambda C_{\mathrm{link}}^{\mathrm{SIC}} = \lambda \mathbb{E}^0 \left[\sum_{m=1}^{N_{\mathrm{to}}} \log_2(1 + \mathrm{SINR}_0^{\mathrm{SIC}}(m)) \right]. \tag{5.5}$$

[8]With the SIC structure, the subspace spanned by $\mathbf{H}_{k,k}(:, m+1), \ldots, \mathbf{H}_{k,k}(:, N_{\mathrm{t},k})$ is suppressed for recovering the m-th data stream.

Even though neither ZF nor ZF-SIC are optimal in the information theoretic sense, these are quite commonly used and in addition amenable to analysis. With these receiving architectures, the exact expressions of the sum spectral efficiency and the corresponding scaling laws are given in the following sections.

5.2.4 Transmision Capacity and Ergodic Spectral Efficiency

The definitions of transmission capacity and ergodic spectral efficiency are as follows:

- Transmission capacity (TC): Maximal spatial density of successful transmissions per unit area (λ) subject to a given outage probability constraint $\mathbb{P}[SIR < \theta] < \epsilon$
- Ergodic spectral efficiency (ESE): achievable Shannon transmission rate:

$$\mathbb{E}[\sum_{i=1}^{N_\mathrm{t}} \log_2(1 + SIR(i))], \tag{5.6}$$

  where N_t is number of transmit antennas and $SIR(i)$ is the SIR of the i-th data stream.

Both metrics are used to analyze wireless networks. TC is more focused on the amount of simultaneous successful transmit links whereas ESE is more focused on achievable information theoretical capacity.

5.3 Direct CSIR

In this section, the exact analytical expressions of the sum spectral efficiency for both ZF and ZF-SIC detection are obtained with DCSIR, i.e., $L_k = 0$ for all $X_k \in \Phi$. Then, a lower and an upper bounds are derived with closed-forms. The announced scaling laws will be obtained from these closed from expressions.

In our closed-form expressions, the Gamma function is used, which is defined as $\Gamma(x) = \int_0^\infty t^{x-1}e^{-t}dt$.

.

5.3.1 Sum Spectral Efficiency

Theorem 20 (ZF with DCSIR)**.** When using ZF detection, the sum spectral efficiency per unit area of DCSIR is

$$C^{\mathrm{ZF}} = \sum_{v=1}^{N_\mathrm{r}} \frac{\alpha\lambda v p_v}{2\ln 2} \int_1^{R_d} \int_0^\infty \frac{e^{-\frac{v\sigma^2}{P}\left(\lambda\pi\sum_{k=1}^{N_\mathrm{r}} p_k \frac{\Gamma(k+\frac{2}{\alpha})\Gamma(1-\frac{2}{\alpha})}{\Gamma(k)u}\right)^{-\frac{\alpha}{2}} - u}}{u} \left(1 - \left(1+ \left(\lambda\pi r^2 \sum_{k=1}^{N_\mathrm{r}} p_k \frac{\Gamma(k+\frac{2}{\alpha})\Gamma(1-\frac{2}{\alpha})}{\Gamma(k)u}\right)^{-\frac{\alpha}{2}}\right)^{-N_\mathrm{r}+v-1}\right) du \frac{2r}{R_d^2-1} dr. \tag{5.7}$$

Proof. See Appendix 5.6.2. □

Theorem 21 (ZF-SIC with DCSIR)**.** When using ZF-SIC detection, the sum

spectral efficiency per unit area of DCSIR is

$$C^{\mathrm{SIC}} = \sum_{v=1}^{N_{\mathrm{r}}} \Bigg[\frac{\alpha\lambda p_v}{2\ln 2} \int_1^{R_d} \int_0^{\infty} \frac{e^{-\frac{v\sigma^2}{P}\left(\lambda\pi \sum_{k=1}^{N_{\mathrm{r}}} p_k \frac{\Gamma(k+\frac{2}{\alpha})\Gamma(1-\frac{2}{\alpha})}{\Gamma(k)u}\right)^{-\frac{\alpha}{2}} - u}}{u} \sum_{m=1}^{v} \Bigg(1 - \Bigg(1 + \left(\lambda\pi r^2 \sum_{k=1}^{N_{\mathrm{r}}} p_k \frac{\Gamma(k+\frac{2}{\alpha})\Gamma(1-\frac{2}{\alpha})}{\Gamma(k)u}\right)^{-\frac{\alpha}{2}} \Bigg)^{-N_{\mathrm{r}}+v-m} \Bigg) du \frac{2r}{R_d^2-1} dr \Bigg]. \tag{5.8}$$

Proof. See Appendix 5.6.2. □

Corollary 14. When all transmitters have N_{t} antennas, i.e. $p_{N_{\mathrm{t}}} = 1$, (5.7) simplifies to

$$C^{\mathrm{ZF}} = \frac{\alpha\lambda N_{\mathrm{t}}}{2\ln 2} \int_1^{R_d} \int_0^{\infty} \frac{e^{-\frac{N_{\mathrm{t}}\sigma^2}{P}\left(\lambda\pi \frac{\Gamma(N_{\mathrm{t}}+\frac{2}{\alpha})\Gamma(1-\frac{2}{\alpha})}{\Gamma(N_{\mathrm{t}})u}\right)^{-\frac{\alpha}{2}} - u}}{u} \Bigg(1 - \left(1 + \left(\lambda\pi r^2 \frac{\Gamma(N_{\mathrm{t}}+\frac{2}{\alpha})\Gamma(1-\frac{2}{\alpha})}{\Gamma(N_{\mathrm{t}})u}\right)^{-\frac{\alpha}{2}} \right)^{-N_{\mathrm{r}}+N_{\mathrm{t}}-1} \Bigg) du \frac{2r}{R_d^2-1} dr, \tag{5.9}$$

and (5.8) reduces to

$$C^{\mathrm{SIC}} = \frac{\alpha\lambda}{2\ln 2} \int_1^{R_d} \int_0^{\infty} \frac{e^{-\frac{N_{\mathrm{t}}\sigma^2}{P}\left(\lambda\pi \frac{\Gamma(N_{\mathrm{t}}+\frac{2}{\alpha})\Gamma(1-\frac{2}{\alpha})}{\Gamma(N_{\mathrm{t}})u}\right)^{-\frac{\alpha}{2}} - u}}{u} \sum_{m=1}^{N_{\mathrm{t}}} \Bigg(1 - \left(\frac{1}{1+\left(\lambda\pi r^2 \frac{\Gamma(N_{\mathrm{t}}+\frac{2}{\alpha})\Gamma(1-\frac{2}{\alpha})}{\Gamma(N_{\mathrm{t}})u}\right)^{-\frac{\alpha}{2}}} \right)^{N_{\mathrm{r}}-N_{\mathrm{t}}+m} \Bigg) du \frac{2r}{R_d^2-1} dr. \tag{5.10}$$

These explicit formulas show how the sum spectral efficiency is determined by the system parameters. Fig. 5.2 plots the sum spectral efficiency of transmitters in region $\mathcal{A} \subset \mathbb{R}^2$ for a path-loss exponent $\alpha = 4$, $|\mathcal{A}| = \pi 500^2 (m^2)$, $R_d = 50m$, $P = -20dBm$, $p_{N_{\mathrm{t}}} = 1$ and $\sigma^2 = -104dBm$.

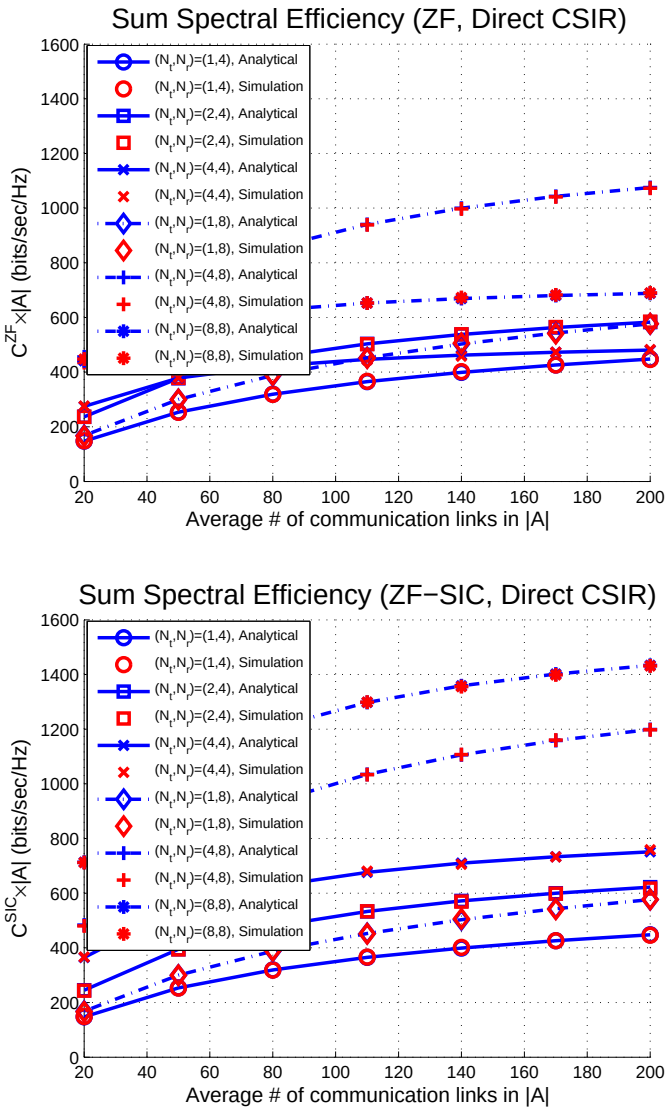

Figure 5.2: The sum efficiency with DCSIR when $|\mathcal{A}| = \pi 500^2(m^2)$, $\alpha = 4$, $R_d = 50(m)$, $P = -20(dBm)$, $\sigma^2 = -104(dBm)$, $p_{N_t} = 1$

The gain of the SIC decorrelator can be found by comparing the two figures in Fig. 5.2.

***Remark* 22.** A drawback of ZF-SIC is error propagation. In the high SNR regime, however, ZF-SIC detection always provides a higher sum spectral efficiency than ZF detection, as can be checked in Fig. 5.2.

One of the interesting observations is that increasing the number of streams N_{t} for a given N_{r} and λ does not necessarily increase the sum spectral efficiency. On the one hand, for a small node density λ, it is possible to increase the sum spectral efficiency per area linearly with the number of spatial multiplexing streams N_{t}. On the other hand, the sum spectral efficiency per area increases sub-linearly with λ as shown in Fig. 5.2. This implies that, for fixed N_{t} and N_{r}, increasing λ will degrade the spectral efficiency per link due to large interference.

To further obtain insights from the derived expressions, it is instructive to consider some examples:

Example 7. When $d_{k,k} = d$ for all $k \in \mathcal{K}$ and $p_{N_{\mathrm{t}}} = 1$, Equations (5.9) and

(5.10) can be simplified as follows

$$C^{\mathrm{ZF}} = \frac{\lambda\alpha N_{\mathrm{t}}}{2\ln 2} \sum_{n=1}^{N_{\mathrm{r}}-N_{\mathrm{t}}+1} \binom{N_{\mathrm{r}}-N_{\mathrm{t}}+1}{n} \times \int_0^{\infty} \frac{e^{-u}}{u} \frac{\left(\frac{\Gamma(N_{\mathrm{t}})u}{\lambda\Gamma(N_{\mathrm{t}}+\frac{2}{\alpha})\Gamma(1-\frac{2}{\alpha})\pi d^2}\right)^{n\frac{\alpha}{2}}}{\left(1+\left(\frac{\Gamma(N_{\mathrm{t}})u}{\lambda\Gamma(N_{\mathrm{t}}+\frac{2}{\alpha})\Gamma(1-\frac{2}{\alpha})\pi d^2}\right)^{\frac{\alpha}{2}}\right)^{N_{\mathrm{r}}-N_{\mathrm{t}}+1}} du \tag{5.11}$$

$$C^{\mathrm{SIC}} = \frac{\lambda\alpha}{2\ln 2} \sum_{m=1}^{N_{\mathrm{t}}} \sum_{n=1}^{N_{\mathrm{r}}-N_{\mathrm{t}}+m} \binom{N_{\mathrm{r}}-N_{\mathrm{t}}+m}{n} \times \int_0^{\infty} \frac{e^{-u}}{u} \frac{\left(\frac{\Gamma(N_{\mathrm{t}})u}{\lambda\Gamma(N_{\mathrm{t}}+\frac{2}{\alpha})\Gamma(1-\frac{2}{\alpha})\pi d^2}\right)^{n\frac{\alpha}{2}}}{\left(1+\left(\frac{\Gamma(N_{\mathrm{t}})u}{\lambda\Gamma(N_{\mathrm{t}}+\frac{2}{\alpha})\Gamma(1-\frac{2}{\alpha})\pi d^2}\right)^{\frac{\alpha}{2}}\right)^{N_{\mathrm{r}}-N_{\mathrm{t}}+m}} du, \tag{5.12}$$

in the interference-limited case ($\sigma^2 = 0$). This simplified single integral form provides a better intuition on the impact of network design parameters on sum spectral efficiency. For example, increasing N_{r} always provides higher performance, and optimizing N_{t} for fixed N_{r} is an important and interesting question.

Example 8. Following Example 7, it is assumed that $N_{\mathrm{t}} = N_{\mathrm{r}}$, $\alpha = 4$. In this case, the sum spectral efficiency per unit area with the ZF-receiver is

$$C^{\mathrm{ZF}} = \frac{2\lambda N_{\mathrm{t}}}{\ln 2} \left\{ \sin(\kappa) \left(\frac{\pi}{2} - Si(\kappa) \right) - \cos(\kappa)\, Ci(\kappa) \right\}, \tag{5.13}$$

where $\kappa = \frac{\pi\lambda d^2 \Gamma(N_{\mathrm{t}}+\frac{1}{2})\Gamma(\frac{1}{2})}{\Gamma(N_{\mathrm{t}})}$, $Si(z) = \int_0^z \frac{\sin(t)}{t} dt$ and $Ci(z) = -\int_z^{\infty} \frac{\cos(t)}{t} dt$ are the sine integral and cosine integral functions, respectively.

In Example 8, if $d = \sqrt{\frac{\Gamma(N_{\mathrm{t}})}{2\lambda\Gamma(N_{\mathrm{t}}+\frac{1}{2})\Gamma(\frac{1}{2})}}$, which means that the distance of communication links is of order of $\lambda^{-\frac{1}{2}}$, the sum spectral efficiency per unit

area becomes

$$C^{\mathrm{ZF}} = \frac{2\lambda N_{\mathrm{t}}}{\ln 2}\left(\frac{\pi}{2} - Si\left(\frac{\pi}{2}\right)\right) \simeq 0.5772\lambda N_{\mathrm{t}}. \tag{5.14}$$

So, if the assumptions in Example 8 and the above relation of d and λ hold, it is possible to guarantee that the sum spectral efficiency per unit area is at least $0.5772 N_{\mathrm{t}}\lambda$.

Throughout this chapter, the main scaling is that of the number of transmit and receive antennas with respect to the network density λ, while this example scales the link distance with respect to λ. In what follows, the distance d will be kept fixed.

5.3.2 Scaling Law

This section provides both a lower and an upper bound with a closed-form on the sum spectral efficiency. This allows us to obtain the announced scaling law. This part focuses on the case where $p_{N_{\mathrm{t}}} = 1$.

Theorem 22 (Direct CSIR, ZF, Scaling Law)**.** Assume that $p_{N_{\mathrm{t}}} = 1$, $N_{\mathrm{t}} = c_1\lambda^{\beta_1}$, $N_{\mathrm{r}} = c_2\lambda^{\beta_2}$, for some constants $c_1, c_2 > 0$, and that $\beta_1 \leq \beta_2$. Then, in the interference limited regime,

$$C^{\mathrm{ZF}} = \Theta(\lambda^{\beta_1+1}\log_2(1+\lambda^{\beta_2-\beta_1-\frac{\alpha}{2}})). \tag{5.15}$$

Proof. See Appendix 5.6.3. □

Theorem 23 (Direct CSIR, Scaling Law, ZF-SIC)**.** Under the same assumptions as in Theorem 22, in the interference limited regime,

$$C^{\mathrm{SIC}} = \Theta(\lambda^{\beta_1+1}\log_2(1+\lambda^{\beta_2-\beta_1-\frac{\alpha}{2}})). \tag{5.16}$$

Proof. See Appendix 5.6.3. □

C^{ZF} and C^{SIC} are functions of λ but here this chapter just uses them instead of $C^{ZF}(\lambda)$ and $C^{SIC}(\lambda)$ for simple notations and the consistency with the previous notations.

***Remark* 23.** The first observation is that, in the DCSIR case, the sum spectral efficiency per unit area is identical for ZF and ZF-SIC in a scaling law sense. This is because the signal power of the m-th data stream under ZF is $\mathbb{E}[H_{k,k}(m)] \simeq N_{\mathrm{r}} - N_{\mathrm{t}} + 1$ and under ZF-SIC is $\mathbb{E}[\tilde{H}_{k,k}(m)] \simeq N_{\mathrm{r}} - N_{\mathrm{t}} + m$ with $m \leq N_{\mathrm{t}}$. Consequently, in our setting, the array gain obtained by ZF-SIC detection, $m-1 = (N - N_{\mathrm{t}} + m) - (N_{\mathrm{r}} - N_{\mathrm{t}} + 1)(\leq c_1\lambda^{\beta_1})$, is negligible in the scaling law sense since $N_{\mathrm{r}}(= c_2\lambda^{\beta_2})$ is dominant. To obtain a gain from the SIC structure, the signal power gain by ZF-SIC should be at least the order of N_{r}, and this will actually be the case for LCISR (see Section 5.4).

This scaling law can be explained intuitively from the definition of the ergodic spectral efficiency. The ergodic spectral efficiency

$$\mathbb{E}^0\left[\sum_{m=1}^{N_{\mathrm{t}}}\log_2(1+\mathrm{SINR}(m))\right]$$

with independent N_{t} data streams, is approximated by $N_{\mathrm{t}}\log_2(1+\mathrm{SINR}(1))$. Since the signal power is $\chi^2_{2(N_{\mathrm{r}}-N_{\mathrm{t}}+1)}$ and the interference power scales as $N_{\mathrm{t}}\lambda^{\frac{\alpha}{2}}$,

the ergodic spectral efficiency scales as $N_{\mathrm{t}} \log_2 \left(1 + \frac{N_{\mathrm{r}} - N_{\mathrm{t}} + 1}{N_{\mathrm{t}} \lambda^{\frac{\alpha}{2}}}\right)$. As λ goes to infinity with the assumption $\beta_2 \geq \beta_1$ which leads $N_{\mathrm{r}} - N_{\mathrm{t}} + 1 \simeq N_{\mathrm{r}}$, (5.16) is obtained.

The next corollary, on per link spectral efficiency, follows immediately from the two theorems stated above.

Corollary 15. When the receive scheme is ZF or ZF-SIC, under DCSIR, the scaling law of the sum spectral efficiency per link is

$$\Theta(\lambda^{\beta_1} \log(\lambda)) \qquad \text{for} \quad \beta_2 - \beta_1 - \frac{\alpha}{2} > 0, \tag{5.17}$$

$$\Theta(\lambda^{\beta_1}) \qquad \text{for} \quad \beta_2 - \beta_1 - \frac{\alpha}{2} = 0, \tag{5.18}$$

$$\Theta(\lambda^{\beta_2 - \frac{\alpha}{2}}) \qquad \text{for} \quad \beta_2 - \beta_1 - \frac{\alpha}{2} < 0. \tag{5.19}$$

Here are important observations following from this corollary.

- Whenever $\beta_2 - \beta_1 - \frac{\alpha}{2} \geq 0$, the spectral efficiency per link is determined by N_{t} or β_1 alone. So, in this regime, *spatial multiplexing*, namely increasing the number of data streams, is beneficial; to the best of our knowledge, this result is new.

- Whenever $\beta_2 - \beta_1 - \frac{\alpha}{2} < 0$, the spectral efficiency per link scales with order of $\Theta(\lambda^{\beta_2 - \frac{\alpha}{2}})$. So the scaling law can be in super-linear region ($\beta_2 > \frac{\alpha}{2}$), linear region ($\beta_2 = \frac{\alpha}{2}$), or sub-linear region ($\beta_2 < \frac{\alpha}{2}$).

- For given β_2 and α, the optimal scaling law is acheived when $\beta_1 = \beta_2 - \frac{\alpha}{2}$, and the corresponding scaling law is $\Theta(\lambda^{\beta_2 - \frac{\alpha}{2}})$.

- For fixed N_{t} and N_{r}, (i.e. $\beta_1, \beta_2 = 0$), the scaling law is $\Theta(\lambda^{-\frac{\alpha}{2}})$.

***Remark* 24.** For fixed N_{t} and N_{r}, the signal-to-interference ratio (SIR) scale invariance, i.e., the fact that the SIR at the typical user does not depend on the infrastructure density, was observed in cellular network with the nearest base station association scenario and with power law attenuation [12]. So, one could expect that the ergodic spectral efficiency, which is a function of SIR, to be also constant in the present situation, but this is not compatible with our scaling result $\Theta(\lambda^{-\frac{\alpha}{2}})$. The main difference between the model in [12] and ours is that there is no interferer closer than the serving base station (i.e., there is a guard zone) in the cellular network model of [12] while the closest interferer in our model may be very close as λ increases.

Example 9. Assume that $p_{N_{\mathrm{t}}} = 1$. For fixed values of N_{t}, N_{r} and α, what is the optimal node density in our model? This part answers this question in a heuristic way by maximizing the lower bounds obtained above. For the ZF case, the density maximizing the lower bound of the sum spectral efficiency per unit area in (5.30) is[9]

$$\lambda^*_{\mathrm{ZF}} = \arg\max_{\lambda} \frac{2\lambda N_{\mathrm{t}}}{\alpha} \log_2 \left(1 + \left(\frac{2\Gamma(N_{\mathrm{t}})}{\Gamma(N_{\mathrm{t}}+\frac{2}{\alpha})\Gamma(1-\frac{2}{\alpha})} \right)^{\frac{\alpha}{2}} \eta \right),$$

where $\eta = \frac{N_{\mathrm{r}}-N_{\mathrm{t}}}{(\lambda\pi(R_d^2+1))^{\frac{\alpha}{2}}}$. For large x, since $\log_2(1+x) \simeq \log_2(x)$, the optimal link density in the high SIR regime is

$$\lambda^*_{\mathrm{ZF}} = \frac{\Gamma(N_{\mathrm{t}})}{2^{\ln 2 - 1}\Gamma(N_{\mathrm{t}}+\frac{2}{\alpha})\Gamma(1-\frac{2}{\alpha})} \frac{(N_{\mathrm{r}}-N_{\mathrm{t}})^{\frac{2}{\alpha}}}{\pi(R_d^2+1)}.$$

[9]Here, ϵ is ignored.

Hence, the optimal medium access probability under the spatial Aloha protocol [14] is

$$p^*_{\mathrm{ZF}} = \min(1, \frac{\lambda^*_{\mathrm{ZF}}}{\lambda}).$$

For the ZF-SIC case, by using the lower bound in (5.35) and the relation $\log_2(1+x) \simeq \log_2(x)$ for large x, the optimal λ given N_{t}, N_{r}, and λ in high SIR regime is

$$\begin{aligned}
\lambda^*_{\mathrm{SIC}} &= \arg\max_{\lambda} \frac{2\lambda}{\alpha} \sum_{m=1}^{N_{\mathrm{t}}} \log_2 \left(1 + \Big(\frac{2\Gamma(N_{\mathrm{t}})}{\Gamma(N_{\mathrm{t}} + \frac{2}{\alpha})\Gamma(1-\frac{2}{\alpha})} \Big)^{\frac{\alpha}{2}} \frac{N_{\mathrm{r}} - N_{\mathrm{t}} + m - 1}{(\lambda\pi(R_d^2+1))^{\frac{\alpha}{2}}} \right) \\
&\simeq \arg\max_{\lambda} \frac{2\lambda}{\alpha} \log_2 \left(\Big(\frac{2\Gamma(N_{\mathrm{t}})}{\Gamma(N_{\mathrm{t}} + \frac{2}{\alpha})\Gamma(1-\frac{2}{\alpha})\pi(R_d^2+1)} \Big)^{\frac{\alpha N_{\mathrm{t}}}{2}} \right. \\
&\left. \times \prod_{m=1}^{N_{\mathrm{t}}} (N_{\mathrm{r}} - N_{\mathrm{t}} + m - 1) \lambda^{-\frac{\alpha N_{\mathrm{t}}}{2}} \right) \\
&= \frac{\Gamma(N_{\mathrm{t}})}{2^{\ln 2 - 1}\Gamma(N_{\mathrm{t}} + \frac{2}{\alpha})\Gamma(1-\frac{2}{\alpha})\pi(R_d^2+1)} \left(\prod_{m=1}^{N_{\mathrm{t}}} (N_{\mathrm{r}} - N_{\mathrm{t}} + m - 1) \right)^{\frac{2}{N_{\mathrm{t}}\alpha}},
\end{aligned}$$

and the optimal medium access probability under the spatial Aloha protocol is

$$p^*_{\mathrm{SIC}} = \min(1, \frac{\lambda^*_{\mathrm{SIC}}}{\lambda}).$$

Example 10. Assume $p_{N_{\mathrm{t}}} = 1$. For fixed N_{r}, λ, and α, What is the optimal value for N_{t}? This can be obtained by using the formulas in Theorem 20 and 21. A simple way consists in maximizing the lower bounds as in Example 9. By using the Gamma function relation

$$\left(\frac{\Gamma(N_{\mathrm{t}})}{\Gamma(N_{\mathrm{t}} + \frac{2}{\alpha})\Gamma(1-\frac{2}{\alpha})} \right)^{\frac{\alpha}{2}} \geq \frac{1}{N_{\mathrm{t}}},$$

Equation (5.30), which is the lower bound of sum spectral efficiency per unit area when ZF-receiver is applied, becomes $f_{\mathrm{LB}}^{\mathrm{ZF}}(N_{\mathrm{t}})$ where

$$f_{\mathrm{LB}}^{\mathrm{ZF}}(x) = \frac{2\lambda x}{\alpha} \log_2 \left(1 + b\frac{N_{\mathrm{r}} - x}{x}\right), \tag{5.20}$$

when

$$b \triangleq \left(\frac{2}{\Gamma(1-\frac{2}{\alpha})}\right)^{\frac{\alpha}{2}} \frac{1}{(\lambda\pi R_d^2)^{\frac{\alpha}{2}}}.$$

One interesting case is $b = 1$, i.e., $\lambda = \frac{2}{\pi R_d^2 \Gamma(1-\frac{2}{\alpha})}$. Since $f_{\mathrm{LB}}^{\mathrm{ZF}}(x)$ is a concave function, the optimal N_{t} is $\lfloor \frac{N_{\mathrm{r}}}{e} \rfloor$ or $\lfloor \frac{N_{\mathrm{r}}}{e} \rfloor + 1$. Another intersting case is that $b \simeq 0$ or equivalently λ is very big. By using a relation $\log(1+x) \simeq x$ for a small x, $f_{\mathrm{LB}}^{\mathrm{ZF}}(x) \simeq \frac{2\lambda b}{\alpha}(N_{\mathrm{r}} - x)$. So, the optimal N_{t} is 1. This means, for a very dense network, transmitting one data stream is the best strategy for enhancing the reliability.

***Remark* 25.** The physical meaning of scaling law can be obtained as follows. The scaling law of ESE of the typical link with respect to the network density is

$$\Theta(\lambda^{\beta_1} \log_2(1 + \lambda^{\beta_2 - \beta_1 - \frac{\alpha}{2}})).$$

Since my target performance metric, ergodic spectral efficiency, is defined as $\mathbb{E}^0[\sum_{i=1}^{N_t} \log_2(1+SIR(o))]$, this is approximately $N_t \log_2(1+\frac{N_r - N_t + 1}{I})$ in the interference limited regime. The interference distribution of Poisson field under distance-based power law is α-stable[10]. In other words, the interference distribution with network density λ is $\lambda^{\frac{\alpha}{2}}$ times that with density 1. Furthermore,

[10]Here, α is not the path-loss exponent

since each interferer send N_t independent data streams from the same location, by plugging $N_t\lambda^{\frac{\alpha}{2}}$ into I, we obtain the above scaling law, since $N_r - N_t + 1$ is approximated by N_r when $\lambda \to \infty$.

***Remark* 26.** One of the results in [10] is that network throughput can be made to scale linearly with the number of receive antennas in the SIMO setting. However, in [10], the main different assumptions with are 1) using partial zero forcing receiver to obtain the optimal scaling law 2) when each receiver knows all channel state information. If I use a partial zero forcing receiver for achieving the optimal scaling law in SIMO setting (i.e., $\beta_1 = 0$), the scaling law of ESE per link will become

$$\Omega(\lambda^{\beta_1}\log_2(1+\lambda^{(\beta_2-\beta_1-1)\frac{\alpha}{2}})) = \Omega(\log_2(1+\lambda^{(\beta_2-1)\frac{\alpha}{2}})), \tag{5.21}$$

and the linear gain (constant per-link performance) can be achieved when $\beta_2 = 1$. This result can be connected with one of the results in [10].

***Remark* 27.** Also in [11], the authors claim that no multiplexing gain is obtained under the transmission capacity view. Both this contribution and [11] compute the post-processed SIR distribution of a certain data stream. So, the interference power when k data streams are sent will be k times larger compared to transmitting just 1 data stream. Under the TC view, due to the outage probability constraint which is

$$\mathbb{P}[\text{SIR} < \theta] < \epsilon,$$

transmitting multiple data streams will reduce the maximal density of transmitting nodes concurrently. In other words, the outage constraint under TC

can be thought as a reliability condition. For increasing the reliability of each stream, transmitting one stream is the optimal strategy. ESE does not consider this reliability. There is no term related to guaranteed SINR in ESE.

***Remark* 28.** Under the cellular network scenario with the nearest BS association [12], the coverage probability improves as α increases which is counter intuitive to the scaling law $\Theta(\lambda^{-\frac{\alpha}{2}})$ when N_t and N_r are fixed. However, under the cellular network scenario, there is no interferer closer than the serving base station (i.e., there is a guard zone). So, in interference-limited networks, SIR ratio will be improved for fixed as increases. However, in my ad-hoc network setting, there is no guard zone. So, when α is big, the closest interfer may be very close which explains why increasing α will be detrimental.

5.4 Local CSIR

LCSIR denotes the situation where $L_k > 0$, i.e., Y_k knows the L_k-nearest interferer CSIs in addition to the CSI of its own channel. Through this section, it is assumed that all transmitters are equipped with N_{t} antennas (i.e., $p_{N_{\mathrm{t}}} = 1$) and $L_k = L$ for all $Y_k \in \bar{\Phi}$ with $1 \leq L \leq \lfloor \frac{N_{\mathrm{r}}}{N_{\mathrm{t}}} \rfloor - 1$.

5.4.1 Sum Spectral Efficiency

In the LCSIR case, the sum spectral efficiencies per unit area are denoted by C_L^{ZF} under ZF and by C_L^{SIC} under ZF-SIC.

Theorem 24. In the LCSIR case, under ZF detection, the achievable sum

spectral efficiency per unit area with L dominant interferer CSI is

$$C_L^{\mathrm{ZF}} = \frac{\lambda N_{\mathrm{t}}}{\ln 2} \int_1^{R_d} \int_0^{\infty} \frac{1}{s e^{\frac{N_{\mathrm{t}} \sigma^2 s}{P}}} \left(1 - \frac{1}{(1+sx^{-\alpha})^{N_{\mathrm{r}}-(L+1)N_{\mathrm{t}}+1}}\right) \mathcal{L}_{\tilde{I}_k}(L;s) ds \frac{2x}{R_d^2 - 1} dx, \tag{5.22}$$

where

$$\mathcal{L}_{\tilde{I}_k}(L;s) = \int_0^{\infty} \exp\left(-\pi\lambda \int_{u=r^2}^{\infty} 1 - \left(\frac{1}{1+su^{-\frac{\alpha}{2}}}\right)^{N_{\mathrm{t}}} du \right) \frac{2(\lambda\pi r^2)^L}{r\Gamma(L)} e^{-\lambda\pi r^2} dr.$$

Proof. See Appendix 5.6.4. □

Theorem 25. In the LCSIR case, the achievable sum spectral efficiency per unit area with L dominant interferer channel information using ZF-SIC detection is

$$C_L^{\mathrm{SIC}} = \sum_{m=1}^{N_{\mathrm{t}}} \frac{\lambda}{\ln 2} \int_1^{R_d} \int_0^{\infty} \frac{1}{s e^{\frac{N_{\mathrm{t}} \sigma^2 s}{P}}} \times \left(1 - \frac{1}{(1+sx^{-\alpha})^{N_{\mathrm{r}}-N_{\mathrm{t}}+m}}\right) \mathcal{L}_{\tilde{I}_k}(L;s) ds \frac{2x}{R_d^2 - 1} dx,$$

where

$$\mathcal{L}_{\tilde{I}_k}(L;s) = \int_0^{\infty} \exp\left(-\pi\lambda \int_{u=r^2}^{\infty} 1 - \left(\frac{1}{1+su^{-\frac{\alpha}{2}}}\right)^{N_{\mathrm{t}}} du \right) \times \frac{2(\lambda\pi r^2)^L}{r\Gamma(L)} e^{-\lambda\pi r^2} dr.$$

Proof. See Appendix 5.6.4. □

Here as in the DCSIR case, the sum spectral efficiency increases with the network density, for both ZF and ZF-SIC. This can be checked in Fig. 5.3 where the sum capacity increases sub-linearly with the average number of links.

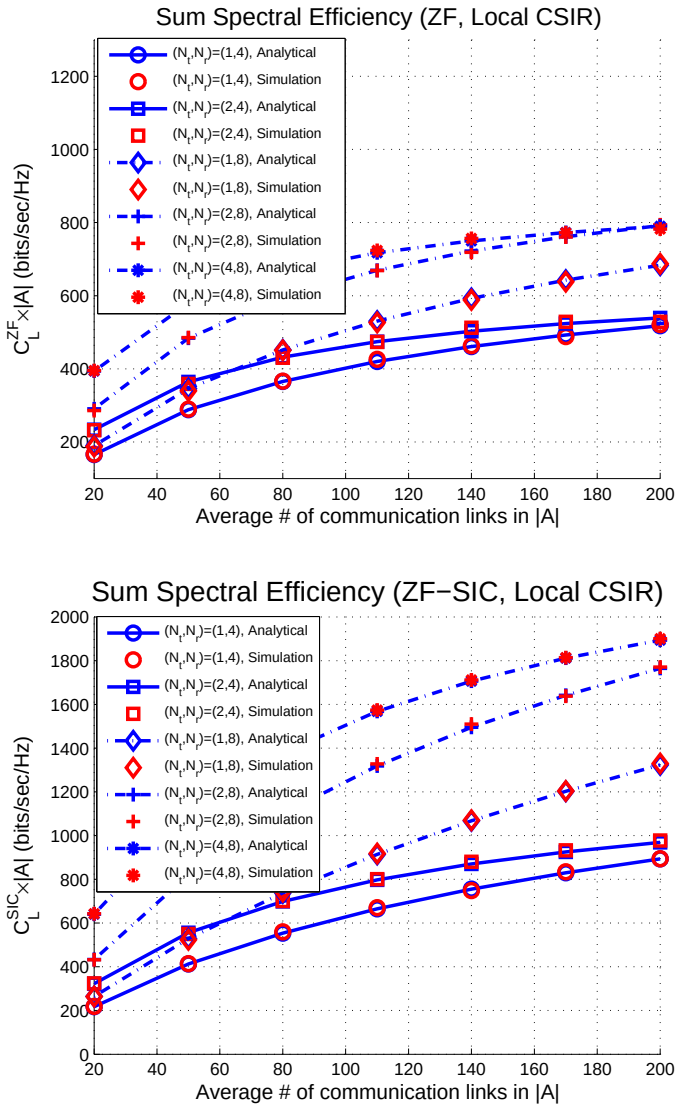

Figure 5.3: The sum spectral efficiency with LCSIR when $|\mathcal{A}| = \pi 500^2 (m^2)$, $\alpha = 4$, $R_d = 50(m)$, $P = -20(dBm)$, $\sigma^2 = -104(dBm)$ with $L = \lfloor \frac{N_r}{N_t} \rfloor - 1$.

***Remark* 29.** For the ZF case, the fading power of the desired signal is lower for LCSIR than for DCSIR because the remaining degrees of freedom at the receiver are used to suppress the inter-node interference from the L-dominant interferers. Therefore, leveraging all channel information is not always beneficial. This can be checked in the first figures of Fig. 5.2 and Fig. 5.3. For the ZF-SIC case, however, utilizing all information is always beneficial, since the fading power of the m-th data stream of the k-th link is $\chi^2_{2(N_\mathrm{r}-N_\mathrm{t}+m)}$, rather than $\chi^2_{2(N_\mathrm{r}-(L+1)N_\mathrm{t}+1)}$ in ZF. This observation can be checked on the second figures of Fig. 5.2 and Fig. 5.3.

5.4.2 Scaling Law

In this section, $L = \lfloor \frac{N_\mathrm{r}}{N_\mathrm{t}} \rfloor - 1$ which is the maximum possible number for nulling the interference from other nodes.

Theorem 26 (Local CSIR, Scaling Law, ZF)**.** Assume that $p_{N_\mathrm{t}} = 1$, and $N_\mathrm{t} = c_1 \lambda^{\beta_1}$, $N_\mathrm{r} = c_2 \lambda^{\beta_2}$ with with some constants $c_1, c_2 > 0$ and $\beta_1 \leq \beta_2$. Then, under ZF detection, the sum spectral efficiency per unit area scales as

$$C_L^{\mathrm{ZF}} = \Omega(\lambda^{\beta_1+1} \log_2(1 + \lambda^{(\beta_2-\beta_1-1)\frac{\alpha}{2}-\beta_2})), \tag{5.23}$$

when $L = \lfloor \frac{N_\mathrm{r}}{N_\mathrm{t}} \rfloor - 1$.

Proof. See Appendix 5.6.5. □

***Remark* 30.** When $\alpha = 4$, under ZF, the scaling law of spectral efficiency per link is $\Theta(\lambda^{\beta_1} \log_2(1 + \lambda^{\beta_2-\beta_1-1}))$ for DCSIR, whereas it is $\Omega(\lambda^{\beta_1} \log_2(1 +$

$\lambda^{\beta_2-2\beta_1-2}$)) for LCSIR In this case, it can be observed that nulling all interference from other nodes is not useful in the sense of scaling laws. This is because the receiver wastes the spatial degrees of freedom to cancel the nearest inter-node interference. This chapter concludes that, when ZF detection is employed, in the scaling law sense, treating the nearest inter-node interference as noise is a better strategy than canceling it.

Theorem 27 (Local CSIR, Scaling Law, ZF-SIC)**.** The assumptions for the number of antenna configurations are the same as in Theorem 26. When $L = \lfloor \frac{N_\mathrm{r}}{N_\mathrm{t}} \rfloor - 1$, the sum spectral efficiency per unit area with ZF-SIC detection scales as

$$C_L^{\mathrm{SIC}} = \Omega(\lambda^{\beta_1+1} \log_2(1 + \lambda^{(\beta_2-\beta_1-1)\frac{\alpha}{2}})). \tag{5.24}$$

Proof. See Appendix 5.6.5. □

The main difference between (5.23) and (5.24) is the recovered degrees of freedom of signal power by the successive cancellation architecture.

Corollary 16. Under ZF-SIC and LCSIR, the scaling law of the ergodic spectral efficiency per link is

$$\begin{aligned}
&\Omega(\lambda^{\beta_1} \log(\lambda)) && \text{for} \quad \beta_2 - \beta_1 - 1 > 0 \\
&\Omega(\lambda^{\beta_1}) && \text{for} \quad \beta_2 - \beta_1 - 1 = 0 \\
&\Omega(\lambda^{\beta_1+(\beta_2-\beta_1-1)\frac{\alpha}{2}}) && \text{for} \quad \beta_2 - \beta_1 - 1 < 0.
\end{aligned}$$

The conclusions are similar to those of Corollary 15. In particular, for given β_2 and α, the best β_1 in the scaling law sense is hence $\beta_1^* = \beta_2 - 1$, and the corresponding scaling law is $\Omega(\lambda^{\beta_2 - 1})$. Since $\alpha > 2$ is assumed, by comparing with the scaling law in Corollary 15, LCSIR can achieve higher performance than DCSIR case in the ergodic spectral efficiency per link in the scaling law sense. [11]

Example 11. When N_{t}, N_{r}, λ, and L are given, the density maximizing the lower bounds in (5.37) for ZF and (5.38) for ZF-SIC under LCSIR can be obtained as follows. As in Example 9, in the high SIR regime, the optimal densities for ZF and ZF-SIC are

$$\lambda^*_{\mathrm{ZF,L}} = \left(\frac{N_{\mathrm{r}} - (L+1)N_{\mathrm{t}}}{\frac{2(1-R_d^{2-\alpha})}{(\alpha-2)(R_d^2-1)}(2\pi)^{\frac{\alpha}{2}} N_{\mathrm{t}}} (L - \frac{\alpha}{2})^{\frac{\alpha}{2}-1} \right)^{\frac{2}{\alpha}} \frac{1}{2^{\ln 2}}$$

$$\lambda^*_{\mathrm{SIC,L}} = \left(\frac{(L - \frac{\alpha}{2})^{\frac{\alpha}{2}-1}}{\frac{2(1-R_d^{2-\alpha})}{(\alpha-2)(R_d^2-1)}(2\pi)^{\frac{\alpha}{2}} N_{\mathrm{t}}} \right)^{\frac{2}{\alpha}} \left(\prod_{m=1}^{N_{\mathrm{t}}} (N_{\mathrm{r}} - N_{\mathrm{t}} + m - 1) \right)^{\frac{2}{N_{\mathrm{t}}\alpha}} \frac{1}{2^{\ln 2}},$$

and the optimal medium access probabilities under the spatial Aloha are

$$p^*_{\mathrm{ZF,L}} = \min\left(1, \frac{\lambda^*_{\mathrm{ZF,L}}}{\lambda}\right)$$

$$p^*_{\mathrm{SIC,L}} = \min\left(1, \frac{\lambda^*_{\mathrm{SIC,L}}}{\lambda}\right).$$

[11] Even though LCSIR achieves higher scaling law over DCSIR, a large amount of CSI is required, which is the cost of the enhanced scaling law. As λ goes to infinity, the required amount of CSI also goes to infinity in asymptotic region.

5.5 Conclusions

This chapter considered a random wireless network with multiple transmit and receive antennas and examined the benefits of using MIMO techniques for obtaining multiplexing gains from the ergodic spectral efficiency point-of-view. Assuming two different types of CSI at receivers, this chapter gave exact analytical expressions and scaling laws for the ergodic spectral efficiency. The main finding is that the scaling of the ergodic spectral efficiency can be made a function of both the density of nodes and the number of transmit streams, provided that the number of antennas scales in a particular polynomial function with the density. Especially, when LCSIR with ZF-SIC detection is employed, the scaling law is enhanced compared to that of DCSIR case.

There are many interesting directions left as future work. One possible direction is to consider antenna correlation effects in both transmit and receive antennas, and to analyze how the correlation effects change the scaling laws. Assuming a MIMO random network with finite feedback, it would also be interesting to investigate the benefits of a closed-loop MIMO transmission technique over the open-loop transmission method examined here. Another direction is to assume a MIMO heterogeneous network and to investigate the optimum number of data streams as a function of the density of nodes.

5.6 Appendix

5.6.1 A Lemma for Capacity Analysis

The following lemma presented in [112] will be useful below.

Lemma 10. Let $x_1, \ldots, x_N, y_1, \ldots, y_M$ be arbitrary non-negative random variables. Then

$$\mathbb{E}\left[\ln\left(1+\frac{\sum_{n=1}^{N} x_n}{\sum_{m=1}^{M} y_m + 1}\right)\right] = \int_0^\infty \frac{\mathcal{M}_y(z) - \mathcal{M}_{x,y}(z)}{z} \exp(-z) dz,$$

where $\mathcal{M}_y(z) = \mathbb{E}\left[e^{-z\sum_{m=1}^{M} y_m}\right]$ and $\mathcal{M}_{x,y}(z) = \mathbb{E}\left[e^{-z(\sum_{n=1}^{N} x_n + \sum_{m=1}^{M} y_m)}\right]$.

Proof. See [112]. □

The following lemma, proved in [109, Appendix B], will also be used:

Lemma 11. Let $X > 0$ and $Y > 0$ be independent non-negative random variables such that $\mathbb{E}[X] < \infty$, $\mathbb{E}[Y] < \infty$, and $\mathbb{E}[\frac{1}{Y}] < \infty$. Then,

$$\begin{aligned}\log_2\left(1+\frac{\exp(\mathbb{E}[\ln(X)])}{\mathbb{E}[Y]}\right) &\leq \mathbb{E}_{X,Y}\left[\log_2\left(1+\frac{X}{Y}\right)\right] \\ &\leq \log_2\left(1+\mathbb{E}[X]\mathbb{E}\left[\frac{1}{Y}\right]\right).\end{aligned}$$

5.6.2 Proof of Theorem 20 and 21

Let X and Y be two independent non-negative random variables with $a \in \mathbb{R}^+$, Lemma 10 becomes

$$\mathbb{E}\left[\ln\left(1+\frac{X}{Y+a}\right)\right] = \int_0^\infty \frac{e^{-az}}{z}(1-\mathbb{E}[e^{-zX}])\mathbb{E}[e^{-zY}]dz. \tag{5.25}$$

Theorem 20 is proven first. Given $d_{0,0} = d$ for the typical link and $N_{\mathrm{t},0} = t$, applying (5.25), the ergodic spectral efficiency for the m-th data stream of the

typical link is

$$\mathbb{E}\left[\log_2\left(1+\frac{H_{0,0}(m)}{d_{0,0}^{\alpha}I_0(m)+\frac{d_{0,0}^{\alpha}N_{\mathrm{t},0}\sigma^2}{P}}\right)|d_{0,0}=d,N_{\mathrm{t},0}=t\right]$$
$$=\frac{1}{\ln 2}\int_0^{\infty}\frac{e^{-\frac{d^{\alpha}t\sigma^2}{P}z}}{z}(1-\mathbb{E}[e^{-zH_{0,0}(m)}])\mathbb{E}[e^{-zd^{\alpha}I_0(m)}]dz. \quad (5.26)$$

Let us define $I_0(m)=\bar{I}_{01}(m)+\bar{I}_{02}(m)+\ldots+\bar{I}_{0N_{\mathrm{r}}}(m)$, where $\bar{I}_{0k}(m)$ comes from nodes with k-transmit antennas. Then, the Laplace transform of the interference $I_0(m)$ is

$$\mathcal{L}_{I_0(m)}(s)=\mathbb{E}[e^{-sI_0(m)}]=\mathbb{E}[e^{-s\sum_{k=1}^{N_{\mathrm{r}}}\bar{I}_{0k}(m)}]$$
$$=\prod_{k=1}^{N_{\mathrm{r}}}\mathbb{E}[e^{-s\bar{I}_{0k}(m)}]=\prod_{k=1}^{N_{\mathrm{r}}}\mathcal{L}_{\bar{I}_{0k}(m)}(s).$$

The Laplace transform of $\bar{I}_{0i}(m)$ is

$$\mathcal{L}_{\bar{I}_{0k}(m)}(s)$$
$$\overset{(a)}{=}\exp\left(-\int_{\mathbb{R}^2}\mathbb{E}_p[1-e^{-s\frac{p}{(\sqrt{x^2+y^2})^{\alpha}}}]\lambda p_k dxdy\right)$$
$$\overset{(b)}{=}\exp\left(-\lambda p_k\int_0^{2\pi}\int_0^{\infty}\mathbb{E}_p[1-e^{-s\frac{p}{r^{\alpha}}}]rdrd\theta\right)$$
$$\overset{(c)}{=}\exp\left(-2\pi\lambda p_k\mathbb{E}_p[\int_0^{\infty}(1-e^{-s\frac{p}{r^{\alpha}}})rdr]\right)$$
$$\overset{(d)}{=}\exp\left(-\pi\lambda p_k\mathbb{E}_p[(sp)^{\frac{2}{\alpha}}\int_0^{\infty}(1-e^{-u})\frac{-2}{\alpha}\frac{1}{u^{1+\frac{2}{\alpha}}}du]\right)$$
$$\overset{(e)}{=}\exp\left(-\pi\lambda p_k\mathbb{E}_p[(sp)^{\frac{2}{\alpha}}\int_0^{\infty}e^{-u}u^{-\frac{2}{\alpha}}du]\right)$$
$$\overset{(f)}{=}\exp\left(-\pi\lambda p_k\Gamma(1-\frac{2}{\alpha})\mathbb{E}_p[(sp)^{\frac{2}{\alpha}}]\right)$$
$$\overset{(g)}{=}\exp\left(-\pi\lambda p_k s^{\frac{2}{\alpha}}\Gamma(1-\frac{2}{\alpha})\frac{\Gamma(k+\frac{2}{\alpha})}{\Gamma(k)}\right).$$

(a) comes from the thinning, the displacement theorem, the independent marking of PPP, and the probability generating functional (PGFL) of PPP [5]; p is the inter-node interference power when $\mathbf{v}_0(m)$ is applied. (b) is obtained by changing from Cartesian coordinates to polar coordinates; (c) is by Fubini's theorem. (d) follows from the change of variable $u = \frac{sp}{r^\alpha}$; (e) comes from the integration by part; (f) is by the definition of the Gamma function and (g) comes from the fact that p is a Chi-squared random variable with $2k$ degrees of freedom.

So, the Laplace transform of the interference $I_0(m)$ at zd^α is

$$\mathbb{E}[e^{-zd^\alpha I_0(m)}] = \prod_{k=1}^{N_\mathrm{r}} \exp\left(-\pi\lambda p_k d^2 z^{\frac{2}{\alpha}} \frac{\Gamma(k+\frac{2}{\alpha})}{\Gamma(k)} \Gamma(1-\frac{2}{\alpha})\right), \tag{5.27}$$

which comes from the independent thinning and the superposition of PPP. By

plugging (5.27) into (5.26),

$$\begin{aligned}
&\frac{1}{\ln 2}\int_0^\infty \frac{e^{-\frac{d^\alpha t\sigma^2}{P}z}}{z}(1-\mathbb{E}[e^{-zH_{0,0}(m)}]) \\
&\quad\times \exp\left(-\pi\lambda d^2 z^{\frac{2}{\alpha}}\sum_{k=1}^{N_\mathrm{r}} p_k \frac{\Gamma(k+\frac{2}{\alpha})}{\Gamma(k)}\Gamma(1-\frac{2}{\alpha})\right) dz \\
&\overset{(a)}{=}\frac{\alpha}{2\ln 2}\int_0^\infty \frac{e^{-\frac{d^\alpha t\sigma^2}{P}\left(\lambda\pi d^2\sum_{k=1}^{N_\mathrm{r}} p_k \frac{\Gamma(k+\frac{2}{\alpha})\Gamma(1-\frac{2}{\alpha})}{\Gamma(k)u}\right)^{-\frac{\alpha}{2}}-u}}{u} \\
&\quad\left(1-\mathbb{E}\left[e^{-\left(\lambda\pi d^2\sum_{k=1}^{N_\mathrm{r}} p_k \frac{\Gamma(k+\frac{2}{\alpha})\Gamma(1-\frac{2}{\alpha})}{\Gamma(k)u}\right)^{-\frac{\alpha}{2}}H_{0,0}(m)}\right]\right) du \\
&\overset{(b)}{=}\frac{\alpha}{2\ln 2}\int_0^\infty \frac{e^{-\frac{d^\alpha t\sigma^2}{P}\left(\lambda\pi d^2\sum_{k=1}^{N_\mathrm{r}} p_k \frac{\Gamma(k+\frac{2}{\alpha})\Gamma(1-\frac{2}{\alpha})}{\Gamma(k)u}\right)^{-\frac{\alpha}{2}}-u}}{u}\Bigg(1- \\
&\quad\left(\frac{1}{1+\left(\lambda\pi d^2\sum_{k=1}^{N_\mathrm{r}} p_k \frac{\Gamma(k+\frac{2}{\alpha})\Gamma(1-\frac{2}{\alpha})}{\Gamma(k)u}\right)^{-\frac{\alpha}{2}}}\right)^{N_\mathrm{r}-t+1}\Bigg) du, \qquad (5.28)
\end{aligned}$$

where (a) comes from a variable change, and (b) follows from deconditioning $H_{0,0}(m)$ which is a Chi-squared random variable with $2(N_\mathrm{r}-t+1)$ degrees of freedom. Since Y_k is uniformly distributed in the ring centered at X_k, (5.9) is obtained by considering all data streams and deconditioning with respect to the number of transmit antennas of the typical link.

For the ZF-SIC detection method, the main difference in the proof is that $\tilde{H}_{0,0}(m)$ is distributed as a Chi-squared with $2(N_\mathrm{r}-t+m)$ degrees of

freedom, and (5.28) is changed to

$$\frac{\alpha}{2\ln 2}\int_0^\infty \frac{e^{-\frac{d^\alpha t\sigma^2}{P}\left(\lambda\pi d^2\sum_{k=1}^{N_\mathrm{r}} p_k \frac{\Gamma(k+\frac{2}{\alpha})\Gamma(1-\frac{2}{\alpha})}{\Gamma(k)u}\right)^{-\frac{\alpha}{2}}-u}}{u}$$
$$\left(1-\left(\frac{1}{1+\left(\lambda\pi d^2\sum_{k=1}^{N_\mathrm{r}} p_k \frac{\Gamma(k+\frac{2}{\alpha})\Gamma(1-\frac{2}{\alpha})}{\Gamma(k)u}\right)^{-\frac{\alpha}{2}}}\right)^{N_\mathrm{r}-t+m}\right)du,$$

and (5.10) is obtained similarly.

5.6.3 Proof of Theorem 22 and 23

Proof. The lower and upper bounds of (5.9) will be derived first. By applying Lemma 11, the sum spectral efficiency over the network is lower bounded as follows:

$$\begin{aligned}
&\lambda\mathbb{E}^0\left[\sum_{m=1}^{N_\mathrm{t}}\log_2(1+\mathrm{SINR}_0^{\mathrm{ZF}}(m))\right]\\
&=\lambda\sum_{m=1}^{N_\mathrm{t}}\mathbb{E}_{H_{0,0}(m),d_{0,0},I_0(m)}\left[\log_2\left(1+\frac{H_{0,0}(m)d_{0,0}^{-\alpha}}{I_0(m)}\right)\right]\\
&\geq\lambda\sum_{m=1}^{N_\mathrm{t}}\mathbb{E}_{d_{0,0},I_0(m)}\left[\log_2\left(1+\frac{e^{\mathbb{E}[\ln(H_{0,0}(m))]}}{d_{0,0}^{\alpha}I_0(m)}\right)\right].
\end{aligned}$$

Since $H_{0,0}(m)$ is a Chi-square random variable with $2(N_\mathrm{r}-N_\mathrm{t}+1)$ degrees of freedom,

$$\mathbb{E}[\ln(H_{0,0}(m))]=\psi(N_\mathrm{r}-N_\mathrm{t}+1),$$

where

$$\psi(n)=-\gamma+\sum_{j=1}^{n-1}\frac{1}{j},$$

with $\gamma \simeq 0.577$, Euler's constant. By [113, Theorem 3.1],

$$e^{\psi(x)} > x - 1, \tag{5.29}$$

and

$$e^{\mathbb{E}[\ln(H_{0,0}(m))]} > N_{\mathrm{r}} - N_{\mathrm{t}} + \epsilon,$$

where ϵ is some positive number[12]. Thus, the lower bound of the sum spectral efficiency per unit area is

$$
\begin{aligned}
&\lambda \sum_{m=1}^{N_\mathrm{t}} \mathbb{E}_{d_{0,0},I_0(m)} \left[\log_2 \left(1 + \frac{N_\mathrm{r} - N_\mathrm{t} + \epsilon}{d_{0,0}^{\alpha} I_0(m)} \right) \right] \\
&\overset{(a)}{=} \frac{\lambda}{\ln 2} \sum_{m=1}^{N_\mathrm{t}} \int_0^\infty \frac{1}{z} (1 - e^{-z(N_\mathrm{r}-N_\mathrm{t}+\epsilon)}) \mathbb{E}_{d_{0,0},I_0(m)} [e^{-z d_{0,0}^{\alpha} I_0(m)}] dz \\
&\overset{(b)}{=} \frac{\lambda}{\ln 2} \sum_{m=1}^{N_\mathrm{t}} \int_0^\infty \frac{1}{z} (1 - e^{-z(N_\mathrm{r}-N_\mathrm{t}+\epsilon)}) \mathbb{E}_{d_{0,0}} \left[\exp \left(-\lambda \pi d_{0,0}^2 z^{\frac{2}{\alpha}} \frac{\Gamma(N_\mathrm{t} + \frac{2}{\alpha}) \Gamma(1 - \frac{2}{\alpha})}{\Gamma(N_\mathrm{t})} \right) \right] dz \\
&\overset{(c)}{\geq} \frac{\lambda}{\ln 2} \sum_{m=1}^{N_\mathrm{t}} \int_0^\infty \frac{1}{z} (1 - e^{-z(N_\mathrm{r}-N_\mathrm{t}+\epsilon)}) \exp \left(-\lambda \pi \mathbb{E}[d_{0,0}^2] z^{\frac{2}{\alpha}} \frac{\Gamma(N_\mathrm{t} + \frac{2}{\alpha}) \Gamma(1 - \frac{2}{\alpha})}{\Gamma(N_\mathrm{t})} \right) dz \\
&\overset{(d)}{=} \frac{\lambda \alpha}{2 \ln 2} \sum_{m=1}^{N_\mathrm{t}} \int_0^\infty \frac{1}{u} e^{-u} \left(1 - e^{-\left(\frac{2\Gamma(N_\mathrm{t})}{\Gamma(N_\mathrm{t}+\frac{2}{\alpha})\Gamma(1-\frac{2}{\alpha})} \right)^{\frac{\alpha}{2}} \frac{N_\mathrm{r}-N_\mathrm{t}+\epsilon}{(\lambda\pi(R_d^2+1))^{\frac{\alpha}{2}}} u^{\frac{\alpha}{2}}} \right) du \\
&\overset{(e)}{\geq} \frac{\lambda}{\ln 2} \sum_{m=1}^{N_\mathrm{t}} \int_0^\infty \frac{1}{u} e^{-u^{\frac{\alpha}{2}}} \left(1 - e^{-\left(\frac{2\Gamma(N_\mathrm{t})}{\Gamma(N_\mathrm{t}+\frac{2}{\alpha})\Gamma(1-\frac{2}{\alpha})} \right)^{\frac{\alpha}{2}} \frac{N_\mathrm{r}-N_\mathrm{t}+\epsilon}{(\lambda\pi(R_d^2+1))^{\frac{\alpha}{2}}} u^{\frac{\alpha}{2}}} \right) du \\
&\overset{(f)}{=} \frac{2\lambda N_\mathrm{t}}{\alpha} \log_2 \left(1 + \left(\frac{2\Gamma(N_\mathrm{t})}{\Gamma(N_\mathrm{t} + \frac{2}{\alpha})\Gamma(1 - \frac{2}{\alpha})} \right)^{\frac{\alpha}{2}} \frac{N_\mathrm{r} - N_\mathrm{t} + \epsilon}{(\lambda \pi (R_d^2 + 1))^{\frac{\alpha}{2}}} \right) \\
&\overset{(g)}{\geq} \frac{2\lambda N_\mathrm{t}}{\alpha} \log_2 \left(1 + \frac{1}{N_\mathrm{t}} \left(\frac{2}{\Gamma(1 - \frac{2}{\alpha})} \right)^{\frac{\alpha}{2}} \frac{N_\mathrm{r} - N_\mathrm{t} + \epsilon}{(\lambda \pi (R_d^2 + 1))^{\frac{\alpha}{2}}} \right),
\end{aligned}
\tag{5.30}
$$

where (a) follows from Lemma 10, (b) comes from the expression for the interference of the Laplace functional of PPP, (c) follows from Lemma 11, (d) comes from a variable change and the fact that $\mathbb{E}[d_{k,k}^2] = \frac{R_d^2+1}{2}$, (e) comes from the fact that $e^{-u} \geq \frac{2}{\alpha} e^{-u^{\frac{\alpha}{2}}}$ when $u \geq 0$ and $\alpha > 2$, (f) is obtained by

[12]With a numerical approach, the gap of $e^{\psi(x)}$ and $x - 1$ is lower bounded by 0.4. For obtaining lower bound of the sum spectral efficiency (and scaling law of it), ϵ is put to prevent the lower bound becoming 0.

$\int_0^\infty \frac{1}{u} e^{-u^{\frac{\alpha}{2}}}(1-e^{-b\times u^{\frac{\alpha}{2}}})du = \frac{2}{\alpha}\log(1+b)$, and (g) comes from

$$\frac{\Gamma(N_{\mathrm{t}})}{\Gamma(N_{\mathrm{t}}+\frac{2}{\alpha})} \geq N_{\mathrm{t}}^{-\frac{2}{\alpha}}.$$

Using the assumption that $N_{\mathrm{t}} = c_1\lambda^{\beta_1}$ and $N_{\mathrm{r}} = c_2\lambda^{\beta_2}$,

$$\lim_{\lambda\to\infty} C^{\mathrm{ZF}} = \Omega(\lambda^{\beta_1+1}\log_2(1+\lambda^{\beta_2-\beta_1-\frac{\alpha}{2}})), \tag{5.31}$$

as λ goes to infinity.

In the interference limited regime,

$$\begin{aligned}
&\lambda\mathbb{E}\left[\sum_{m=1}^{N_{\mathrm{t}}}\log_2(1+\mathrm{SINR}_0^{\mathrm{ZF}}(m))\right] \\
&= \lambda\sum_{m=1}^{N_{\mathrm{t}}}\mathbb{E}_{H_{0,0}(m),d_{0,0},I_0(m)}\left[\log_2\left(1+\frac{H_{0,0}(m)d_{0,0}^{-\alpha}}{I_0(m)}\right)\right] \\
&\overset{(a)}{\leq} \lambda N_{\mathrm{t}}\log_2\left(1+\mathbb{E}[d_{0,0}^{-\alpha}]\mathbb{E}[H_{0,0}(m)]\mathbb{E}\left[\frac{1}{I_0(m)}\right]\right) \\
&\overset{(b)}{=} \lambda N_{\mathrm{t}}\log_2\left(1+\frac{2(1-R_d^{2-\alpha})}{(\alpha-2)(R_d^2-1)}\frac{1}{R_d^{\alpha}}(N_{\mathrm{r}}-N_{\mathrm{t}}+1)\frac{\Gamma(1+\frac{2}{\alpha})\Gamma(N_{\mathrm{t}})^{\frac{\alpha}{2}}}{(\lambda\pi\Gamma(N_{\mathrm{t}}+\frac{2}{\alpha})\Gamma(1-\frac{2}{\alpha}))^{\frac{\alpha}{2}}}\right),
\end{aligned} \tag{5.32}$$

where (a) comes from Lemma 11, and (b) follows from $\mathbb{E}[d_{0,0}^{-\alpha}] = \frac{2(1-R_d^{2-\alpha})}{(\alpha-2)(R_d^2-1)}$, $\mathbb{E}[H_{0,0}(m)] = N_{\mathrm{r}}-N_{\mathrm{t}}+1$, and the relation of $\mathbb{E}\left[\frac{1}{X}\right] = \mathbb{E}\left[\int_0^\infty e^{-sX}ds\right]$ for any positive random variable X. The negative moment of $I_0(m)$ is

$$\begin{aligned}
\mathbb{E}\left[\frac{1}{I_0(m)}\right] &= \int_0^\infty \mathbb{E}[e^{-sI_0(m)}]ds \\
&= \int_0^\infty e^{-\lambda\pi\frac{\Gamma(N_{\mathrm{t}}+\frac{2}{\alpha})\Gamma(1-\frac{2}{\alpha})}{\Gamma(N_{\mathrm{t}})}s^{\frac{2}{\alpha}}}ds \\
&= \frac{\Gamma(1+\frac{2}{\alpha})\Gamma(N_{\mathrm{t}})^{\frac{\alpha}{2}}}{(\lambda\pi\Gamma(N_{\mathrm{t}}+\frac{2}{\alpha})\Gamma(1-\frac{2}{\alpha}))^{\frac{\alpha}{2}}}.
\end{aligned}$$

Therefore, the upper bound on the sum spectral efficiency per unit area is

$$C^{\mathrm{ZF}} = \lambda N_{\mathrm{t}} \log_2 \left(1 + \frac{2(1-R_d^{2-\alpha})}{(\alpha-2)(R_d^2-1)} (N_{\mathrm{r}} - N_{\mathrm{t}} + 1) \frac{\Gamma(1+\frac{2}{\alpha})\Gamma(N_{\mathrm{t}})^{\frac{\alpha}{2}}}{(\lambda\pi\Gamma(N_{\mathrm{t}}+\frac{2}{\alpha})\Gamma(1-\frac{2}{\alpha}))^{\frac{\alpha}{2}}} \right)$$
$$\leq \lambda N_{\mathrm{t}} \log_2 \left(1 + \frac{2(1-R_d^{2-\alpha})}{(\alpha-2)(R_d^2-1)} (N_{\mathrm{r}} - N_{\mathrm{t}} + 1) \frac{\Gamma(1+\frac{2}{\alpha})}{(\lambda\pi\Gamma(1-\frac{2}{\alpha}))^{\frac{\alpha}{2}}} \left((N_{\mathrm{t}}-1)^{-\frac{2}{\alpha}} \right)^{\frac{\alpha}{2}} \right),$$

where the last inequality comes from

$$\frac{\Gamma(x)}{\Gamma(x+\frac{2}{\alpha})} \leq (x-1)^{-\frac{2}{\alpha}}. \tag{5.33}$$

By letting λ tend to infinity,

$$\lim_{\lambda\to\infty} C^{\mathrm{ZF}} = \mathcal{O}(\lambda^{\beta_1+1} \log_2(1+\lambda^{\beta_2-\beta_1-\frac{\alpha}{2}})). \tag{5.34}$$

Equations (5.31) and (5.34) conclude the proof of Theorem 22.

The proof of Theorem 23 is analogous to that of Theorem 22. The main difference consists in changing $H_{0,0}(m) \sim \chi^2_{2(N_{\mathrm{r}}-N_{\mathrm{t}}+1)}$ to $\tilde{H}_{0,0}(m) \sim \chi^2_{2(N_{\mathrm{r}}-N_{\mathrm{t}}+m)}$. The lower bound of the sum spectral efficiency per unit area becomes

$$\lambda \mathbb{E}\left[\sum_{m=1}^{N_{\mathrm{t}}} \log_2 \left(1 + \mathrm{SINR}_0^{\mathrm{SIC}}(m) \right) \right]$$
$$> \frac{2\lambda}{\alpha} \sum_{m=1}^{N_{\mathrm{t}}} \log_2 \left(1 + \left(\frac{2\Gamma(N_{\mathrm{t}})}{\Gamma(N_{\mathrm{t}}+\frac{2}{\alpha})\Gamma(1-\frac{2}{\alpha})} \right)^{\frac{\alpha}{2}} \frac{N_{\mathrm{r}} - N_{\mathrm{t}} + m - 1 + \epsilon}{(\lambda\pi(R_d^2+1))^{\frac{\alpha}{2}}} \right)$$
$$> \frac{2\lambda N_{\mathrm{t}}}{\alpha} \log_2 \left(1 + \frac{1}{N_{\mathrm{t}}} \left(\frac{2}{\Gamma(1-\frac{2}{\alpha})} \right)^{\frac{\alpha}{2}} \frac{N_{\mathrm{r}} - N_{\mathrm{t}} + \epsilon}{(\lambda\pi(R_d^2+1))^{\frac{\alpha}{2}}} \right), \tag{5.35}$$

and the upper bound becomes

$$\lambda \mathbb{E}\left[\sum_{m=1}^{N_{\mathrm{t}}} \log_2\left(1+\mathrm{SINR}_0^{\mathrm{SIC}}(m)\right)\right]$$
$$\leq \lambda \sum_{m=1}^{N_{\mathrm{t}}} \log_2\left(1+\frac{2(1-R_d^{2-\alpha})}{(\alpha-2)(R_d^2-1)}(N_{\mathrm{r}}-N_{\mathrm{t}}+m)\frac{\Gamma(1+\frac{2}{\alpha})\Gamma(N_{\mathrm{t}})^{\frac{\alpha}{2}}}{(\lambda\pi\Gamma(N_{\mathrm{t}}+\frac{2}{\alpha})\Gamma(1-\frac{2}{\alpha}))^{\frac{\alpha}{2}}}\right)$$
$$< \lambda N_{\mathrm{t}} \log_2\left(1+\frac{2(1-R_d^{2-\alpha})}{(\alpha-2)(R_d^2-1)}\frac{\Gamma(1+\frac{2}{\alpha})}{(\pi\Gamma(1-\frac{2}{\alpha}))^{\frac{\alpha}{2}}}N_{\mathrm{r}}\left(\frac{\Gamma(N_{\mathrm{t}})}{\Gamma(N_{\mathrm{t}}+\frac{2}{\alpha})}\right)^{\frac{\alpha}{2}}\lambda^{-\frac{\alpha}{2}}\right)$$
$$\leq \lambda N_{\mathrm{t}} \log_2\left(1+\frac{2(1-R_d^{2-\alpha})}{(\alpha-2)(R_d^2-1)}\frac{\Gamma(1+\frac{2}{\alpha})}{(\pi\Gamma(1-\frac{2}{\alpha}))^{\frac{\alpha}{2}}}\frac{N_{\mathrm{r}}}{N_{\mathrm{t}}-1}\lambda^{-\frac{\alpha}{2}}\right),$$

where the last inequality comes from (5.33). With the foregoing assumptions, the scaling law of the sum spectral per unit area with respect to the density becomes $\Theta(\lambda^{\beta_1+1}\log_2(1+\lambda^{\beta_2-\beta_1-\frac{\alpha}{2}}))$. □

5.6.4 Proof of Theorem 24 and 25

Lemma 10 is used again. First, the ZF-receiver case is derived. Conditioned on $d_{k,k}=d$, the spectral efficiency of the m-th data stream of the typical link is

$$\mathbb{E}\left[\log_2\left(1+\frac{\tilde{H}_{0,0}(m)d_{0,0}^{-\alpha}}{\tilde{I}_0(m)+\frac{N_{\mathrm{t}}\sigma^2}{P}}\right)|d_{0,0}=d\right]$$
$$=\frac{1}{\ln 2}\int_0^\infty \frac{e^{-\frac{N_{\mathrm{t}}\sigma^2}{P}z}}{z}(1-\mathbb{E}[e^{-zH_{0,0}(m)}d^{-\alpha}])$$
$$\times \mathbb{E}[e^{-z\sum_{j=L+1}^{\infty}\tilde{H}_{0,0_j}(m)d_{0,0_j}^{-\alpha}}]dz, \tag{5.36}$$

by Lemma 10. Since $\tilde{H}_{0,0}(m)$ is Chi-square distributed with $2(N_{\mathrm{r}}-(L+1)N_{\mathrm{t}}+1)$ distributed,

$$\mathbb{E}\left[e^{-z\tilde{H}_{0,0}(m)d^{-\alpha}}\right]=\frac{1}{(1+zd^{-\alpha})^{N_{\mathrm{r}}-(L+1)N_{\mathrm{t}}+1}}.$$

The Laplace transform of $\tilde{I}_0(m)$ for the given L is

$$\mathcal{L}_{\tilde{I}_0(m)}(L;z) = \mathbb{E}\left[e^{-z\sum_{j=L+1}^{\infty}\tilde{H}_{0,0_j}(m)d_{0,0_j}^{-\alpha}}\right].$$

Under the condition that the L-th nearest interferer's distance is r, the Laplace transform is obtained as

$$\begin{aligned}
&\mathcal{L}_{\tilde{I}_0(m)|d_{0,0_L}=r}(L;z)\\
&= \mathbb{E}\left[e^{-z\sum_{j=L+1}^{\infty}\tilde{H}_{0,0_j}(m)d_{0,0_j}^{-\alpha}}|d_{0,0_L}=r\right]\\
&\overset{(a)}{=} \mathbb{E}\left[\prod_{d_{0,0_j}\in\Phi\setminus\mathcal{B}(0,r)}\frac{1}{(1+zd_{0,0_j}^{-\alpha})^{N_\mathrm{t}}}|d_{0,0_L}=r\right]\\
&\overset{(b)}{=} \exp\left(-\pi\lambda\int_{u=r^2}^{\infty}1-\frac{1}{(1+zu^{-\frac{\alpha}{2}})^{N_\mathrm{t}}}du\right),
\end{aligned}$$

where (a) comes from the fact that $\tilde{H}_{0,0_j}(m)\sim\chi^2_{2N_\mathrm{t}}$ and (b) follows from PGFL. The distribution of r is given in [114] and by unconditioning with respect to it,

$$\begin{aligned}
\mathcal{L}_{\tilde{I}_0(m)}(L;z) = \int_0^{\infty}&\exp(-\pi\lambda\int_{u=r^2}^{\infty}1-\frac{1}{(1+zu^{-\frac{\alpha}{2}})^{N_\mathrm{t}}}du)\\
&\times\frac{2(\lambda\pi r^2)^L}{r\Gamma(L)}e^{-\lambda\pi r^2}dr.
\end{aligned}$$

Thus, the sum spectral efficiency conditioned on $d_{k,k}=d$ can be written as

$$\begin{aligned}
&\mathbb{E}\left[\log_2\left(1+\frac{\tilde{H}_{0,0}(m)d^{-\alpha}}{\tilde{I}_0(m)+\frac{\sigma^2N_\mathrm{t}}{P}}\right)|\{d_{0,0}=d\}\right]\\
&=\frac{1}{\ln 2}\int_0^{\infty}\frac{e^{-\frac{sN_\mathrm{t}\sigma^2}{P}}}{s}\left[1-\frac{1}{(1+zd^{-\alpha})^{N_\mathrm{r}-(L+1)N_\mathrm{t}+1}}\right]\mathcal{L}_{\tilde{I}_0}(L;s)ds.
\end{aligned}$$

It is obtained that the announced result when using the fact that $d_{0,0}$ is uniformly distributed in a ring with radii $(1,R_d)$.

The result for ZF-SIC follows by the same arguments, using the fact that $\tilde{H}_{0,0}(m)$ is Chi-square random variable with $2(N_{\mathrm{r}} - N_{\mathrm{t}} + m)$ degrees of freedom.

5.6.5 Proof of Theorem 26 and 27

Proof. First, the proof of Theorem 26 is considered. The lower bound of (5.22) is

$$\begin{aligned}
&\lambda \mathbb{E}\left[\sum_{m=1}^{N_{\mathrm{t}}} \log_2(1+\mathrm{SINR}_{0,L}^{\mathrm{ZF}}(m))\right] \\
&= \lambda \sum_{m=1}^{N_{\mathrm{t}}} \mathbb{E}_{\tilde{H}_{0,0} d_{0,0}, \tilde{I}_0(m)}\left[\log_2\left(1+\frac{\tilde{H}_{0,0}(m) d_{0,0}^{-\alpha}}{\tilde{I}_0(m)}\right)\right] \\
&\overset{(a)}{\geq} \lambda \sum_{m=1}^{N_{\mathrm{t}}} \log_2\left(1+\frac{e^{\mathbb{E}[\ln(\tilde{H}_{0,0}(m))]}}{\mathbb{E}[d_{0,0}^{-\alpha}]\mathbb{E}[\tilde{I}_0(m)]}\right) \\
&\overset{(b)}{>} \lambda \sum_{m=1}^{N_{\mathrm{t}}} \log_2\left(1+\frac{N_{\mathrm{r}} - (L+1)N_{\mathrm{t}} + \epsilon}{\frac{2(1-R_d^{2-\alpha})}{(\alpha-2)(R_d^2-1)}\mathbb{E}[\tilde{I}_k(m)]}\right),
\end{aligned}$$

where (a) comes from Lemma 11, and (b) comes from the inequality (5.29), $\mathbb{E}[d_{0,0}^{-\alpha}] = \frac{2(1-R_d^{2-\alpha})}{(\alpha-2)(R_d^2-1)}$. The expectation of $\tilde{I}_0$ conditioned on $d_{0,0_L} = r$ is

$$\mathbb{E}[\tilde{I}_0(m) | d_{0,0_L} = r] = \frac{2\pi\lambda N_{\mathrm{t}}}{2-\alpha} r^{2-\alpha}.$$

By unconditioning with respect to $d_{0,0_L}$ whose distribution is given in [114],

$$\begin{aligned}
\mathbb{E}[\tilde{I}_0(m)] &= \frac{2\pi\lambda N_{\mathrm{t}}}{2-\alpha} \int_0^{\infty} r^{2-\alpha} \frac{2(\lambda\pi r^2)^L}{r\Gamma(L)} e^{-\lambda\pi r^2} dr \\
&= (2\pi\lambda)^{\frac{\alpha}{2}} N_{\mathrm{t}} \frac{\Gamma(1-\frac{\alpha}{2}+L)}{\Gamma(L)}.
\end{aligned}$$

By leveraging

$$\frac{\Gamma(L)}{\Gamma(1-\frac{\alpha}{2}+L)} \geq (L-\frac{\alpha}{2})^{\frac{\alpha}{2}-1},$$

the lower bound becomes

$$\begin{aligned}
&\lambda \mathbb{E}\left[\sum_{m=1}^{N_{\mathrm{t}}} \log_2(1+\mathrm{SINR}_{0,L}^{\mathrm{ZF}}(m))\right] \\
&> \lambda N_{\mathrm{t}} \log_2\left(1+\frac{N_{\mathrm{r}}-(L+1)N_{\mathrm{t}}+\epsilon}{\frac{2(1-R_d^{2-\alpha})}{(\alpha-2)(R_d^2-1)}} \frac{\Gamma(L)}{(2\pi\lambda)^{\frac{\alpha}{2}} N_{\mathrm{t}} \Gamma(1-\frac{\alpha}{2}+L)}\right) \\
&\geq \lambda N_{\mathrm{t}} \log_2\left(1+\frac{N_{\mathrm{r}}-(L+1)N_{\mathrm{t}}+\epsilon}{\frac{2(1-R_d^{2-\alpha})}{(\alpha-2)(R_d^2-1)}(2\pi\lambda)^{\frac{\alpha}{2}} N_{\mathrm{t}}}(L-\frac{\alpha}{2})^{\frac{\alpha}{2}-1}\right). \qquad (5.37)
\end{aligned}$$

By plugging $N_{\mathrm{t}} = c_1\lambda^{\beta_1}$, $N_{\mathrm{r}} = c_2\lambda^{\beta_2}$ into (5.37),

$$\lim_{\lambda\to\infty} C_L^{\mathrm{ZF}} = \Omega(\lambda^{\beta_1+1}\log_2(1+\lambda^{(\beta_2-\beta_1-1)\frac{\alpha}{2}-\beta_2})),$$

since $L = \lfloor \frac{N_{\mathrm{r}}}{N_{\mathrm{t}}} \rfloor - 1$.

The proof of Theorem 27 is almost identical to the proof of Theorem 26. The main difference is in the distribution of $\tilde{H}_{0,0}(m)$. The lower bound becomes

$$\begin{aligned}
&\lambda \mathbb{E}\left[\sum_{m=1}^{N_{\mathrm{t}}} \log_2(1+\mathrm{SINR}_{0,L}^{\mathrm{SIC}}(m))\right] \\
&> \lambda \sum_{m=1}^{N_{\mathrm{t}}} \log_2\left(1+\frac{N_{\mathrm{r}}-N_{\mathrm{t}}+m-1+\epsilon}{\frac{2(1-R_d^{2-\alpha})}{(\alpha-2)(R_d^2-1)}(2\pi\lambda)^{\frac{\alpha}{2}} N_{\mathrm{t}}}(L-\frac{\alpha}{2})^{\frac{\alpha}{2}-1}\right). \qquad (5.38)
\end{aligned}$$

With the foregoing assumptions,

$$\lim_{\lambda\to\infty} C_L^{\mathrm{SIC}} = \Omega(\lambda^{\beta_1+1}\log_2(1+\lambda^{(\beta_2-\beta_1-1)\frac{\alpha}{2}})).$$

□

Chapter 6

Conclusion

This dissertation mainly aims at using stochastic geometry to model and analyze emerging wireless networks. The first contribution of this dissertation is the development of new mathematical models for studying wireless networks scenarios which have not been discussed sufficiently. Chapter 2 proposed the *Poisson building* for 3-D in-building networks using Poisson line processes. Chapter 3 introduced the concept of *shadowing cell* where base stations in the same *shadowing cell* have the same shadowing random variable. The second contribution of this dissertation is the analysis of correlated shadowing in stochastic geometry models. The new mathematical models in Chapters 2, 3 allow one to study the impact of spatially correlated shadowing fields. Especially, Chapter 3 showed that widely used performance metrics are evaluated in a pessimistic way under the independent shadowing assumption. Chapter 4 investigated multihop communications in mmWave networks and compared some connectivity results between the correlated and independent shadowing models. Finally, Chapter 5 showed that spatial multiplexing is beneficial under MIMO ad-hoc networks with a newly defined metric, *Ergodic spectral efficiency*.

In the rest of this chapter, I summarize the main contributions and discuss the prospective future works.

6.1 Summary

In Chapter 2, I proposed a new 3-D spatial model for in-building wireless networks which capture spatial shadowing correlation created by the static physical walls. Most previous models studied outdoor networks on the scale of a city and the shadowing correlation is typically ignored and path loss is simply modeled through independent log-normal shadowing coefficients [2, 3] or a distance dependent function combined with independent fading/shadowing random variables [4, 13]. These models ignore shadowing effects generated by spatial geometry.

This new 3-D model for in-building wireless networks is the *Poisson building* model, which explicitly handles the shadowing correlation. This model is compatible with the empirically supported lognormal shadowing model in that the marginal shadowing component converges to lognormal distribution as the link distance grows. The tractability of the Poisson building model is provided by explicitly deriving the interference distribution and its spatial correlation. Under this model, analytical characterizations of the coverage probability of in-building cellular networks. The analysis of these variants further reveals fundamental differences between 3-D and 2-D correlated shadowing analysis.

In Chapter 3, I proposed a new network model, *Shadowing cell* to

analyze the correlated shadowing field in general outdoor wireless networks. The Poisson building model can capture the correlated shadowing field, but it is limited to in-building wireless networks and blockage-based path loss function. As already explained, most of the previous research papers used the independent shadowing approximation to analyze the shadowing effects. In contrast, in order to represent the spatial correlation property, some shadowing values are assigned based on the obstacle topology. Especially, base stations in the same *Shadowing cell* have the same shadowing random variable.

The main contribution is the comparison of the interference distribution between the correlated and independent shadowing models in the stochastic ordering sense. Chapter 3 computed the Laplace transforms of the interference observed by the typical user which is located at the origin under these two models, and then provides the ordering relation of the three metrics for the typical user, i.e., 1) coverage probability, 2) Shannon throughput, and 3) local delay. These three metrics were shown completely monotone functions of the interference. From well known results on the relation between the Laplace transform ordering and completely monotone functions, the ordering relations were obtained between the two shadowing assumptions. One interesting observation in this Chapter was that the evaluation of the considered metrics under the independent approximation was systematically pessimistic compared to the correlated shadowing model.

In Chapter 4, I proposed a new stochastic geometric approach to analyze mmWave multihop networks in the presence of blockages. The multi-

hop connectivity under the mmWave networks has not been widely discussed in previous papers. I considered two blockage models: *independent blockage model* and *correlated blockage model*. The *independent blockage* model was considered in order to get exact analytical expressions of connectivity results. In this model, the blockage process is independent over links even though two links are close to each other. Then, I considered the *correlated blockage* model which is closer to real environments. I provided exact expressions of connectivity results under the *independent blockage* setting and compare some of these results between two blockage models since it is hard to obtain exact expressions under the correlated blockage model. To the best of my knowledge, this comparison has not been discussed in the mmWave multihop setting.

Further, I provided new percolation results under the correlated blockage model. Under the independent blockage model, there always exists a user critical density for the existence of an infinite size connected user cluster. However, under the correlated blockage model, the critical user density does not exist under certain blockage conditions. This comparison provides new insight of percolation theory under the more realistic network scenarios.

In Chapter 5, I analyzed MIMO ad-hoc networks modeled by a Poisson bipolar network. In previous works, under this setting, the transmission capacity which quantifies the maximum allowable spatial density of successful transmissions per unit area subject to a given outage probability constraint was characterized. However, a common shortcoming of the transmission capacity metric is that it cannot capture the effects of rate adaptation techniques,

which are the key features used in many modern wireless systems to track and exploit channel variations. The main novelty of this contribution compared to this line of thought is the analysis of the *ergodic spectral efficiency* (rather than transport capacity), which quantifies the achievable Shannon transmission rate per unit area when adapting the rate to the different local conditions.

For a MIMO setting, I derived the exact expressions of *ergodic spectral efficiency* under a Poisson bipolar setting. One key message in this chapter was that *spatial multiplexing* transmission techniques [110] can improve the scaling laws of the sum spectral efficiency which cannot be obtained under the transmission capacity view.

6.2 Future Directions

Based on the stochastic geometry frameworks in this dissertation, various performance metrics of wireless networks can be analyzed with fundamental approaches. As wireless networks evolve with more features, this mathematical tool can still serve as an important analytical tool. These advanced features lead more challenging stochastic geometry analysis such as new network scenarios and new physical phenomena. Motivated by these, I propose some prospective research directions that extends contributions in this dissertation.

6.2.1 Effects of the Shadowing Correlation: Quantifying, Multihop Networks, mmWave Networks

One core result of this dissertation is the analysis of the effect of correlated shadowing using stochastic geometry. I proposed new models (Poisson building and Shadowing cell) and presented some network connectivity results in mmWave multihop networks for understanding the impact of the shadowing correlation. Especially, the main result of Chapter 3 is that when ignoring the spatial correlations of shadowing, widely used metrics such as coverage probability, Shannon throughput, local delay are systematically evaluated in a pessimistic way. This was proved by using stochastic ordering and completely monotone functions. This result is new and provides a better qualitative understanding of the effect of shadowing correlation. However, Chapter 3 does not quantify how much different these metrics are under the independent and the correlated shadowing. From this point, one interesting possible direction would be to quantify the impact of correlated shadowing on the important metrics.

Another possible research direction is to understand the effect of shadowing correlation in multihop networks. All results in Chapter 3 are focused on the typical user's performance under single-hop networks. By investigating this effect under multihop scenarios, it should be possible to analyze the impact of correlated shadowing on other important results such as connectivity (partly discussed in Chapter 4), delay and so on. Since multihop communication is a promising technique to extend coverage in emerging 5G networks,

understanding the impact of the correlated shadowing on this type of communications is particularly important.

In Chapter 3, the path-loss model is exactly that used in [4] and connected to the blockage-based path loss model in [16, 115, 116]. The results in this contribution can be directly applied for lower frequencies networks. In the path loss model used in this chapter, the channel path loss exponent is fixed. In the analysis of mmWave networks using stochastic geometry, different path-loss exponents are used for LOS and NLOS signals. So, the results cannot be directly applied to general mmWave networks. However, if we admit independence between NLOS and LOS signals as in previous papers, by assuming interference to be the sum of two independent interference process (LOS and NLOS signals), it is possible to extend our results to general mmWave networks. In this case, since $\mathcal{L}_I(s) = \mathcal{L}_{I_{LOS}}(s) \times \mathcal{L}_{I_{NLOS}}(s)$, the ordering relations of some performance metrics between the correlated and independent shadowing models will be the same. The analysis of the correlation between LOS and NLOS signals can be another interesting research direction in connection with mmWave networks.

6.2.2 mmWave Multihop Communications: More Metrics, MAC Protocols, NLOS signals, and Interference

As already mentioned, multihop communication is a very promising technique in emerging 5G networks in terms of coverage extension. Chapter 4 is motivated by this and mainly presented the connectivity results by leveraging

stochastic geometry tools.

In classical studies on multihop networks, the following metrics are typically considered.

1. Per-hop transmission success probability [14]: The probability that the SINR at the receiver is above a particular threshold;

2. Normalized average forward progress [117]: The average distance traveled by the packet towards its final destination;

3. End-to-end delay [14]: the time taken for a packet to be transmitted across a network from source to destination.

One particularly interesting research direction would consist in analyzing the above metrics under multihop communications in mmWave networks. Combined with the connectivity results in Chapter 4, the analysis of these performance metrics will provide a way to progress on network management and cell planning. Further, it would be quite useful to use this framework to design new MAC protocols which aim at reducing or preventing collisions by limiting interference in these networks.

In Chapter 4, I only analyzed the LOS connectivity of mmWave networks. However, it is known that high data rate can be supported by NLOS links through reflected paths [74]. So, analyzing the connectivity of NLOS signals which support the 5G immersive experiences [75] will be another interesting future direction. Further, the connectivity results in Chapter 4 are

analyzed under the noise-limited networks. However, interference is not negligible with certain network parameters. It should be stressed that when considering interference, the connection rules become more complicated functions of network topology.

6.2.3 Network Analysis under Clustered Poisson Networks

In classical stochastic geometrical models, the underlying node distribution is often assumed to be the homogeneous Poisson point process, which is equivalent to assuming complete spatial randomness for node locations. This assumption neglects the dependencies among node locations in practical systems [118]. I analyze the correlated shadowing effect under the Matérn cluster process in Chapter 3. Similarly, it is possible to analyze MIMO ad-hoc networks modeled by clustered networks such as Poisson cluster process as in Chapter 5.

The Matérn cluster process, an example of Poisson cluster processes, consists of mother homogeneous PPP of intensity λ_m and daughter points, which are marks of each mother point with parameter λ_d. The daughter points are uniformly distributed in a circle centered at their mother point and with radius R_d. Two scenarios are applicable for this Matérn cluster process: 1) body area network and 2) vehicular ad-hoc networks. It is possible to assume that the daughter points (potential transmitters) transmit to their mother points (potential receivers), see Figure 6.1. So, each person (or each monitor) can be thought as a mother point and its body networks can be thought of as

daughter points. Another appropriate scenario is that of vehicular networks. The roadside units (RSU) are distributed as a homogeneous PPP (mother process) and cars in communication range from a certain RSU can be modeled as a finite-size PPP (daughter process). This network model is highly correlated with the model in Chapter 5. The main differences are 1) the number of the potential data streams for each receiver is not fixed and 2) the sources of data streams are spatially separated.

The expected results in this research direction are: 1) comparing the ergodic spectral efficiency under PPP and PCP networks to understand the clustered networks 2) examining the benefits of using MIMO techniques in PCP networks and 3) connecting the results to the previous results such as Laplace ordering of point processes [49, 119].

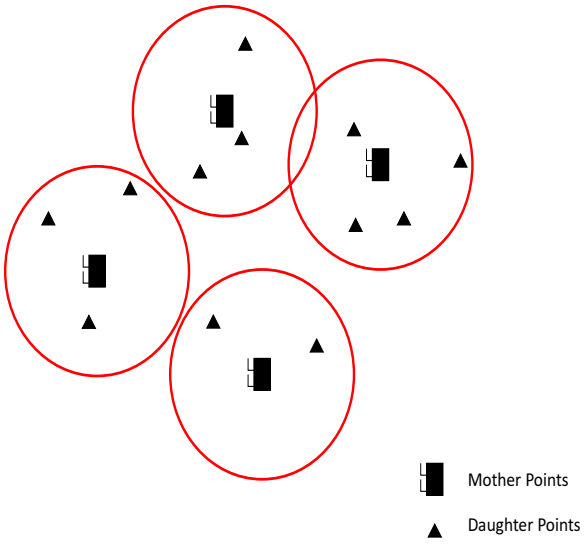

Figure 6.1: Matérn cluster process

Bibliography

[1] H. ElSawy, E. Hossain, and M. Haenggi, "Stochastic geometry for modeling, analysis, and design of multi-tier and cognitive cellular wireless networks: A survey," *IEEE Communications Surveys & Tutorials*, vol. 15, no. 3, pp. 996–1019, 2013.

[2] J. Ilow and D. Hatzinakos, "Analytic alpha-stable noise modeling in a Poisson field of interferers or scatterers," *IEEE Transactions on Signal Processing*, vol. 46, no. 6, pp. 1601–1611, 1998.

[3] B. Blaszczyszyn, M. K. Karray, and H. P. Keeler, "Wireless networks appear Poissonian due to strong shadowing," *IEEE Transactions on Wireless Communications*, vol. 14, no. 8, pp. 4379–4390, 2015.

[4] T. Bai, R. Vaze, and R. W. Heath, "Analysis of blockage effects on urban cellular networks," *IEEE Transactions on Wireless Communications*, vol. 13, no. 9, pp. 5070–5083, 2014.

[5] F. Baccelli and B. Blaszczyszyn, *Stochastic Geometry and Wireless Networks: Volume 1: THEORY*. Now Publishers Inc, 2009, vol. 1.

[6] R. S. Blum, "MIMO capacity with interference," *IEEE Journal on Selected Areas in Communications*, vol. 21, no. 5, pp. 793–801, 2003.

[7] B. Chen and M. J. Gans, "MIMO communications in ad hoc networks," *IEEE Transactions on Signal Processing*, vol. 54, no. 7, pp. 2773–2783, 2006.

[8] X. Yu, R. M. De Moraes, H. Sadjadpour, and J. Garcia-Luna-Aceves, "Capacity of MIMO mobile wireless ad hoc networks," in *International Conference on Wireless Networks, Communications and Mobile Computing, 2005*, vol. 2. IEEE, 2005, pp. 1053–1058.

[9] S. P. Weber, X. Yang, J. G. Andrews, and G. De Veciana, "Transmission capacity of wireless ad hoc networks with outage constraints," *IEEE Transactions on Information Theory*, vol. 51, no. 12, pp. 4091–4102, 2005.

[10] N. Jindal, J. G. Andrews, and S. Weber, "Multi-antenna communication in ad hoc networks: Achieving mimo gains with simo transmission," *Communications, IEEE Transactions on*, vol. 59, no. 2, pp. 529–540, 2011.

[11] R. Vaze and R. W. Heath, "Transmission capacity of ad-hoc networks with multiple antennas using transmit stream adaptation and interference cancellation," *IEEE Transactions on Information Theory*, vol. 58, no. 2, pp. 780–792, 2012.

[12] J. G. Andrews, F. Baccelli, and R. K. Ganti, "A tractable approach to coverage and rate in cellular networks," *IEEE Transactions on Communications*, vol. 59, no. 11, pp. 3122–3134, 2011.

[13] T. Bai and R. W. Heath, "Coverage and rate analysis for millimeter-wave cellular networks," *IEEE Transactions on Wireless Communications*, vol. 14, no. 2, pp. 1100–1114, 2015.

[14] F. Baccelli and B. Blaszczyszyn, *Stochastic Geometry and Wireless Networks: Volume 2: APPLICATIONS*. Now Publishers Inc, 2009, vol. 2.

[15] J. Lee, X. Zhang, and F. Baccelli, "Shadowing and coverage in Poisson buildings," in *IEEE INFOCOM 2016-The 35th Annual IEEE International Conference on Computer Communications*. IEEE, 2016, pp. 1–9.

[16] ——, "A 3-d spatial model for in-building wireless networks with correlated shadowing," *IEEE Transactions on Wireless Communications*, vol. 15, no. 11, pp. 7778–7793, 2016.

[17] P. Gupta and P. R. Kumar, "Internets in the sky: The capacity of three dimensional wireless networks," *Communications in Information and Systems*, vol. 1, no. 1, pp. 33–50, Jan. 2001.

[18] A. K. Gupta, X. Zhang, and J. G. Andrews, "SINR and throughput scaling in ultradense urban cellular networks," *IEEE Wireless Communications Letters*, Aug. 2015.

[19] A. Goldsmith, *Wireless Communications*. New York, NY, USA: Cambridge University Press, 2005.

[20] X. Zhang and J. G. Andrews, "Downlink cellular network analysis with multi-slope path loss models," *IEEE Transactions on Communications*, vol. 63, no. 5, pp. 1881–1894, 2015.

[21] J. W. McKown and R. L. Hamilton, "Ray tracing as a design tool for radio networks," *IEEE Network*, vol. 5, no. 6, pp. 27–30, 1991.

[22] R. Valenzuela, "A ray tracing approach to predicting indoor wireless transmission," in *Vehicular Technology Conference*, May 1993, pp. 214–218.

[23] D. J. Daley and D. Vere-Jones, *An Introduction to the Theory of Point Processes*, 2nd ed. Springer, 2007.

[24] F. Baccelli and X. Zhang, "A correlated shadowing model for urban wireless networks," in *IEEE INFOCOM'15*, Apr. 2015.

[25] S. Marano and M. Franceschetti, "Ray propagation in a random lattice: a maximum entropy, anomalous diffusion process," *IEEE Transactions on Antennas and Propagation*, vol. 53, no. 6, pp. 1888–1896, 2005.

[26] R. K. Ganti and M. Haenggi, "Spatial and temporal correlation of the interference in ALOHA ad hoc networks," *IEEE Communications Letters*, vol. 13, no. 9, pp. 631–633, 2009.

[27] W. Feller, *An introduction to probability theory and its applications*. John Wiley & Sons, 2008, vol. 2.

[28] X. Zhang, F. Baccelli, and R. Heath, "An indoor correlated shadowing model," in *IEEE Global Telecommunications Conference*, Dec. 2015.

[29] H. S. Dhillon, R. K. Ganti, F. Baccelli, and J. G. Andrews, "Modeling and analysis of K-tier downlink heterogeneous cellular networks," *IEEE Journal on Selected Areas in Communications*, vol. 30, no. 3, pp. 550–560, 2012.

[30] M. Haenggi, *Stochastic geometry for wireless networks*. Cambridge University Press, 2012.

[31] J. Lee and F. Baccelli, "On the effect of shadowing correlation on wireless network performance," *arXiv preprint arXiv:1712.00900*, 2017.

[32] T. S. Rappaport *et al.*, *Wireless communications: principles and practice*. Prentice Hall PTR New Jersey, 1996, vol. 2.

[33] A. Goldsmith, *Wireless communications*. Cambridge university press, 2005.

[34] A. J. Coulson, A. G. Williamson, and R. G. Vaughan, "A statistical basis for lognormal shadowing effects in multipath fading channels," *IEEE Transactions on Communications*, vol. 46, no. 4, pp. 494–502, 1998.

[35] M. Gudmundson, "Correlation model for shadow fading in mobile radio systems," *Electronics letters*, vol. 27, no. 23, pp. 2145–2146, 1991.

[36] M. Shaked, J. G. Shanthikumar, and Y. Tong, "Stochastic orders and their applications," *SIAM Review*, vol. 37, no. 3, pp. 477–478, 1995.

[37] F. Graziosi and F. Santucci, "A general correlation model for shadow fading in mobile radio systems," *IEEE Communications Letters*, vol. 6, no. 3, pp. 102–104, 2002.

[38] P. Agrawal and N. Patwari, "Correlated link shadow fading in multi-hop wireless networks," *IEEE Transactions on Wireless Communications*, vol. 8, no. 8, pp. 4024–4036, 2009.

[39] E-UTRA, "Evolved universal terrestrial radio access (E-UTRA); Further advancements for E-UTRA physical layer aspects," 3GPP TR 36.814, Tech. Rep., 2010.

[40] V. Erceg *et al.*, "TGn channel models," *IEEE 802.11-03/940r4*, 2004.

[41] S. Weber, J. G. Andrews, and N. Jindal, "An overview of the transmission capacity of wireless networks," *IEEE Transactions on Communications*, vol. 58, no. 12, pp. 3593–3604, 2010.

[42] F. Baccelli, B. Blaszczyszyn, and P. Muhlethaler, "An ALOHA protocol for multihop mobile wireless networks," *IEEE Transactions on Information Theory*, vol. 52, no. 2, pp. 421–436, 2006.

[43] X. Zhang and M. Haenggi, "Random power control in Poisson networks," *IEEE Transactions on Communications*, vol. 60, no. 9, pp. 2602–2611, 2012.

[44] ——, "Delay-optimal power control policies," *IEEE Transactions on Wireless Communications*, vol. 11, no. 10, pp. 3518–3527, 2012.

[45] H. S. Dhillon, T. D. Novlan, and J. G. Andrews, "Coverage probability of uplink cellular networks," in *2012 IEEE Global Communications Conference (GLOBECOM)*. IEEE, 2012, pp. 2179–2184.

[46] F. Baccelli and X. Zhang, "A correlated shadowing model for urban wireless networks," in *2015 IEEE Conference on Computer Communications (INFOCOM)*. IEEE, 2015, pp. 801–809.

[47] X. Zhang, F. Baccelli, and R. W. Heath, "An indoor correlated shadowing model," in *Global Communications Conference (GLOBECOM), 2015 IEEE*. IEEE, 2015, pp. 1–7.

[48] S. N. Chiu, D. Stoyan, W. S. Kendall, and J. Mecke, *Stochastic geometry and its applications*. John Wiley & Sons, 2013.

[49] B. Błaszczyszyn, D. Yogeshwaran *et al.*, "Directionally convex ordering of random measures, shot noise fields, and some applications to wireless communications," *Advances in Applied Probability*, vol. 41, no. 3, pp. 623–646, 2009.

[50] R. Burton and E. Waymire, "Scaling limits for associated random measures," *The Annals of Probability*, pp. 1267–1278, 1985.

[51] R. Pemantle, "Towards a theory of negative dependence," *Journal of Mathematical Physics*, vol. 41, no. 3, pp. 1371–1390, 2000.

[52] B. Błaszczyszyn, D. Yogeshwaran *et al.*, "On comparison of clustering properties of point processes," *Advances in Applied Probability*, vol. 46, no. 1, pp. 1–20, 2014.

[53] A. Alzaid, J. S. Kim, and F. Proschan, "Laplace ordering and its applications," *Journal of Applied Probability*, vol. 28, no. 1, pp. 116–130, 1991.

[54] R. K. Ganti and M. Haenggi, "Interference and outage in clustered wireless ad hoc networks," *IEEE Transactions on Information Theory*, vol. 55, no. 9, pp. 4067–4086, 2009.

[55] J. Lee and F. Baccelli, "On the comparison of correlated and independent shadowing," in *INFOCOM*, 2018, long version of the submission. Available at https://arxiv.org/abs/1712.00900.

[56] D. J. Daley and D. Vere-Jones, *An introduction to the theory of point processes*. Springer Science & Business Media, 2007.

[57] T. S. Rappaport, R. W. Heath Jr, R. C. Daniels, and J. N. Murdock, *Millimeter wave wireless communications*. Pearson Education, 2014.

[58] J. G. Andrews, S. Buzzi, W. Choi, S. V. Hanly, A. Lozano, A. C. Soong, and J. C. Zhang, "What will 5g be?" *IEEE Journal on selected areas in communications*, vol. 32, no. 6, pp. 1065–1082, 2014.

[59] S. Rangan, T. S. Rappaport, and E. Erkip, "Millimeter-wave cellular wireless networks: Potentials and challenges," *Proceedings of the IEEE*, vol. 102, no. 3, pp. 366–385, 2014.

[60] S. Singh, F. Ziliotto, U. Madhow, E. Belding, and M. Rodwell, "Blockage and directivity in 60 ghz wireless personal area networks: From cross-layer model to multihop mac design," *IEEE Journal on Selected Areas in Communications*, vol. 27, no. 8, 2009.

[61] H.-S. Jo, Y. J. Sang, P. Xia, and J. G. Andrews, "Heterogeneous cellular networks with flexible cell association: A comprehensive downlink SINR analysis," *IEEE Transactions on Wireless Communications*, vol. 11, no. 10, pp. 3484–3495, 2012.

[62] T. Bai, A. Alkhateeb, and R. W. Heath, "Coverage and capacity of millimeter-wave cellular networks," *IEEE Communications Magazine*, vol. 52, no. 9, pp. 70–77, 2014.

[63] S. Singh, M. N. Kulkarni, A. Ghosh, and J. G. Andrews, "Tractable model for rate in self-backhauled millimeter wave cellular networks," *IEEE Journal on Selected Areas in Communications*, vol. 33, no. 10, pp. 2196–2211, 2015.

[64] A. Thornburg, T. Bai, and R. W. Heath Jr, "Performance analysis of outdoor mmwave ad hoc networks." *IEEE Trans. Signal Processing*, vol. 64, no. 15, pp. 4065–4079, 2016.

[65] T.-C. Hou and V. Li, "Transmission range control in multihop packet radio networks," *IEEE Transactions on Communications*, vol. 34, no. 1, pp. 38–44, 1986.

[66] E. S. Sousa and J. A. Silvester, "Optimum transmission ranges in a direct-sequence spread-spectrum multihop packet radio network," *IEEE journal on selected areas in communications*, vol. 8, no. 5, pp. 762–771, 1990.

[67] K. Stamatiou and M. Haenggi, "Delay characterization of multihop transmission in a poisson field of interference," *IEEE/ACM Transactions on Networking*, vol. 22, no. 6, pp. 1794–1807, 2014.

[68] F. Baccelli, B. Blaszczyszyn, and P. Mühlethaler, "A spatial reuse aloha mac protocol for multihop wireless mobile networks," Ph.D. dissertation, INRIA, 2003.

[69] F. Baccelli, B. Blaszczyszyn, and P. Muhlethaler, "On the performance of time-space opportunistic routing in multihop mobile ad hoc networks," in *Modeling and Optimization in Mobile, Ad Hoc, and Wireless Networks and Workshops, 2008. WiOPT 2008. 6th International Symposium on*. IEEE, 2008, pp. 307–316.

[70] X. Lin and J. G. Andrews, "Connectivity of millimeter wave networks with multi-hop relaying," *IEEE Wireless Communications Letters*, vol. 4, no. 2, pp. 209–212, 2015.

[71] R. Meester, M. D. Penrose, and A. Sarkar, "The random connection model in high dimensions," *Statistics & probability letters*, vol. 35, no. 2, pp. 145–153, 1997.

[72] M. D. Penrose, "On a continuum percolation model," *Advances in applied probability*, vol. 23, no. 3, pp. 536–556, 1991.

[73] X. J. Li, B.-C. Seet, and P. H. J. Chong, "Multihop cellular networks: Technology and economics," *Computer Networks*, vol. 52, no. 9, pp. 1825–1837, 2008.

[74] Y. Inoue, Y. Kishiyama, Y. Okumura, J. Kepler, and M. Cudak, "Experimental evaluation of downlink transmission and beam tracking performance for 5g mmw radio access in indoor shielded environment," in *Personal, Indoor, and Mobile Radio Communications (PIMRC), 2015 IEEE 26th Annual International Symposium on*. IEEE, 2015, pp. 862–866.

[75] Y. Qi, M. Hunukumbure, M. Nekovee, J. Lorca, and V. Sgardoni, "Quantifying data rate and bandwidth requirements for immersive 5g experience," in *Communications Workshops (ICC), 2016 IEEE International Conference on*. IEEE, 2016, pp. 455–461.

[76] M. R. Akdeniz, Y. Liu, M. K. Samimi, S. Sun, S. Rangan, T. S. Rappaport, and E. Erkip, "Millimeter wave channel modeling and cellular capacity evaluation," *IEEE journal on selected areas in communications*, vol. 32, no. 6, pp. 1164–1179, 2014.

[77] M. N. Kulkarni, S. Singh, and J. G. Andrews, "Coverage and rate trends in dense urban mmwave cellular networks," in *Global Communications Conference (GLOBECOM), 2014 IEEE*. IEEE, 2014, pp. 3809–3814.

[78] S. G. Larew, T. A. Thomas, M. Cudak, and A. Ghosh, "Air interface design and ray tracing study for 5g millimeter wave communications," in *Globecom Workshops (GC Wkshps), 2013 IEEE*. IEEE, 2013, pp. 117–122.

[79] D. Stauffer and A. Aharony, *Introduction to percolation theory*. CRC press, 1994.

[80] F. Baccelli and P. Brémaud, *Elements of queueing theory: Palm Martingale calculus and stochastic recurrences*. Springer Science & Business Media, 2013, vol. 26.

[81] M. Ismail, W. Zhuang, E. Serpedin, and K. Qaraqe, "A survey on green mobile networking: From the perspectives of network operators and mobile users," *IEEE Communications Surveys & Tutorials*, vol. 17, no. 3, pp. 1535–1556, 2015.

[82] W. Elam, A. Kerstein, and J. Rehr, "Critical properties of the void percolation problem for spheres," *Physical review letters*, vol. 52, no. 17, p. 1516, 1984.

[83] J. Kertész, "Percolation of holes between overlapping spheres: Monte carlo calculation of the critical volume fraction," *Journal de Physique*

Lettres, vol. 42, no. 17, pp. 393–395, 1981.

[84] J. Lee, N. Lee, and F. Baccelli, "Scaling laws for ergodic spectral efficiency in mimo poisson networks," *IEEE Transactions on Information Theory*, 2017.

[85] P. Gupta and P. R. Kumar, "The capacity of wireless networks," *IEEE Transactions on Information Theory*, vol. 46, no. 2, pp. 388–404, 2000.

[86] S. Toumpis and A. J. Goldsmith, "Capacity regions for wireless ad hoc networks," *IEEE Transactions on Wireless Communications*, vol. 2, no. 4, pp. 736–748, 2003.

[87] H. Hartenstein and K. P. Laberteaux, "A tutorial survey on vehicular ad hoc networks," *IEEE Communications Magazine*, vol. 46, no. 6, pp. 164–171, 2008.

[88] K. Doppler, M. Rinne, C. Wijting, C. B. Ribeiro, and K. Hugl, "Device-to-device communication as an underlay to LTE-advanced networks," *IEEE Communications Magazine*, vol. 47, no. 12, pp. 42–49, 2009.

[89] G. Fodor, E. Dahlman, G. Mildh, S. Parkvall, N. Reider, G. Miklós, and Z. Turányi, "Design aspects of network assisted device-to-device communications," *IEEE Communications Magazine*, vol. 50, no. 3, pp. 170–177, 2012.

[90] A. Özgür, O. Lévêque, and D. N. Tse, "Hierarchical cooperation achieves optimal capacity scaling in ad hoc networks," *IEEE Transactions on Information Theory*, vol. 53, no. 10, pp. 3549–3572, 2007.

[91] A. M. Tulino and S. Verdú, *Random matrix theory and wireless communications*. Now Publishers Inc, 2004, vol. 1.

[92] M. Franceschetti, O. Dousse, N. David, and P. Thiran, "Closing the gap in the capacity of wireless networks via percolation theory," *IEEE Transactions on Information Theory*, vol. 53, no. 3, pp. 1009–1018, 2007.

[93] O. Lévêque and E. Telatar, "Information theoretic upper bounds on the capacity of large extended ad-hoc wireless networks," in *Proceedings of the 2004 IEEE International Symposium on Information Theory*, no. LTHI-CONF-2006-010, 2004.

[94] M. Grossglauser and D. Tse, "Mobility increases the capacity of ad-hoc wireless networks," in *INFOCOM 2001. Twentieth Annual Joint Conference of the IEEE Computer and Communications Societies. Proceedings. IEEE*, vol. 3. IEEE, 2001, pp. 1360–1369.

[95] R. Negi and A. Rajeswaran, "Capacity of power constrained ad-hoc networks," in *INFOCOM 2004. Twenty-third AnnualJoint Conference of the IEEE Computer and Communications Societies*, vol. 1. IEEE, 2004.

[96] M. Franceschetti, M. D. Migliore, and P. Minero, "The capacity of wireless networks: Information-theoretic and physical limits," *IEEE Trans-*

actions on Information Theory, vol. 55, no. 8, pp. 3413–3424, 2009.

[97] D. Stoyan, W. S. Kendall, and J. Mecke, *Stochastic Geometry and its Applications*, 2nd ed. Chichester: Wiley, 1995.

[98] J. G. Andrews, S. Weber, and M. Haenggi, "Ad hoc networks: to spread or not to spread?[ad hoc and sensor networks]," *IEEE Communications Magazine*, vol. 45, no. 12, pp. 84–91, 2007.

[99] S. P. Weber, J. G. Andrews, X. Yang, and G. De Veciana, "Transmission capacity of wireless ad hoc networks with successive interference cancellation," *IEEE Transactions on Information Theory*, vol. 53, no. 8, pp. 2799–2814, 2007.

[100] J. Blomer and N. Jindal, "Transmission capacity of wireless ad hoc networks: Successive interference cancellation vs. joint detection," in *IEEE International Conference on Communications, 2009. ICC'09.* IEEE, 2009, pp. 1–5.

[101] X. Zhang and M. Haenggi, "The performance of successive interference cancellation in random wireless networks," *IEEE Transactions on Information Theory*, vol. 60, no. 10, pp. 6368–6388, 2014.

[102] A. M. Hunter, J. G. Andrews, and S. Weber, "Transmission capacity of ad hoc networks with spatial diversity," *Wireless Communications, IEEE Transactions on*, vol. 7, no. 12, pp. 5058–5071, 2008.

[103] S. Akoum, M. Kountouris, M. Debbah, and R. W. Heath, "Spatial interference mitigation for multiple input multiple output ad hoc networks: Miso gains," in *Signals, Systems and Computers (ASILOMAR), 2011 Conference Record of the Forty Fifth Asilomar Conference on.* IEEE, 2011, pp. 708–712.

[104] R. H. Louie, M. R. McKay, and I. B. Collings, "Open-loop spatial multiplexing and diversity communications in ad hoc networks," *IEEE Transactions on Information Theory*, vol. 57, no. 1, pp. 317–344, 2011.

[105] K. Huang, J. G. Andrews, D. Guo, R. W. Heath, and R. A. Berry, "Spatial interference cancellation for multiantenna mobile ad hoc networks," *Information Theory, IEEE Transactions on*, vol. 58, no. 3, pp. 1660–1676, 2012.

[106] M. Kountouris and J. G. Andrews, "Transmission capacity scaling of SDMA in wireless ad hoc networks," in *IEEE Information Theory Workshop, 2009. ITW 2009.* IEEE, 2009, pp. 534–538.

[107] N. Lee, D. Morales-Jimenez, A. Lozano, and R. W. Heath, "Spectral efficiency of dynamic coordinated beamforming: A stochastic geometry approach," *IEEE Transactions on Wireless Communications*, vol. 14, no. 1, pp. 230–241, 2015.

[108] A. Lozano and N. Jindal, "Are yesterday-s information-theoretic fading models and performance metrics adequate for the analysis of today's

wireless systems?" *IEEE Communications Magazine*, vol. 50, no. 11, pp. 210–217, 2012.

[109] N. Lee, F. Baccelli, and R. W. Heath, "Spectral efficiency scaling laws in dense random wireless networks with multiple receive antennas," *IEEE Transactions on Information Theory*, vol. 62, no. 3, pp. 1344–1359, 2016.

[110] D. Tse and P. Viswanath, *Fundamentals of wireless communication*. Cambridge university press, 2005.

[111] X. Wu, S. Tavildar, S. Shakkottai, T. Richardson, J. Li, R. Laroia, and A. Jovicic, "Flashlinq: A synchronous distributed scheduler for peer-to-peer ad hoc networks," *IEEE/ACM Transactions on Networking (TON)*, vol. 21, no. 4, pp. 1215–1228, 2013.

[112] K. A. Hamdi, "A useful lemma for capacity analysis of fading interference channels," *Communications, IEEE Transactions on*, vol. 58, no. 2, pp. 411–416, 2010.

[113] A. Laforgia and P. Natalini, "On some inequalities for the gamma function," *Advances in Dynamical Systems and Applications*, vol. 8, no. 2, pp. 261–267, 2013.

[114] M. Haenggi, "On distances in uniformly random networks," *IEEE Transactions on Information Theory*, vol. 51, no. 10, pp. 3584–3586, 2005.

[115] F. Baccelli and X. Zhang, "A correlated shadowing model for urban wireless networks," in *IEEE INFOCOM*, vol. 15.

[116] X. Zhang, F. Baccelli, and R. W. Heath Jr, "An indoor correlated shadowing model."

[117] M. J. Farooq, H. ElSawy, and M.-S. Alouini, "A stochastic geometry model for multi-hop highway vehicular communication," *IEEE Transactions on Wireless Communications*, vol. 15, no. 3, pp. 2276–2291, 2016.

[118] Y. Li, F. Baccelli, H. S. Dhillon, and J. G. Andrews, "Statistical modeling and probabilistic analysis of cellular networks with determinantal point processes," *IEEE Transactions on Communications*, vol. 63, no. 9, pp. 3405–3422, 2015.

[119] J. Lee and C. Tepedelenlioğlu, "Stochastic ordering of interference in large-scale wireless networks," *IEEE Transactions on Signal Processing*, vol. 62, no. 3, pp. 729–740, 2014.

Vita

Junse Lee received the B.S. and M.S. degrees in Electrical and Electronic Engineering from KAIST, Daejeon, Korea, in 2009 and 2011, respectively. He joined the Wireless Networking and Communications Group (WNCG) in Fall 2014, and has been pursuing toward his Ph.D. degree in the Department of Electrical and Computer Engineering, The University of Texas at Austin, Austin, TX, USA. From 2011 to 2014, he worked at Samsung Electronics Telecommunication Network, where he dealt with LTE eNB system design. His research interest is developing and analyzing future wireless communication systems using tools of multi-antenna theory, information theory, and stochastic geometry.

Permanent address: junselee@utexas.edu

This dissertation was typeset with LaTeX[†] by the author.

[†]LaTeX is a document preparation system developed by Leslie Lamport as a special version of Donald Knuth's TeX Program.